TITANIUM DIOXIDE NANOSTRUCTURES FOR PHOTOCATALYTIC AND PHOTOVOLTAIC APPLICATIONS

A DISSERTATION SUBMITTED TO
THE DEPARTMENT OF PHYSICS
AND THE INSTITUTE OF ENGINEERING AND SCIENCE
OF BILKENT UNIVERSITY
IN PARTIAL FULFILLMENT OF THE REQUIREMENTS
FOR THE DEGREE OF
DOCTOR OF PHILOSOPHY

By
Deniz Çakır
August, 2008

I certify that I have read this thesis and that in my opinion it is fully adequate, in scope and in quality, as a dissertation for the degree of doctor of philosophy.

Assoc. Prof. Dr. Oğuz Gülseren(Supervisor)

I certify that I have read this thesis and that in my opinion it is fully adequate, in scope and in quality, as a dissertation for the degree of doctor of philosophy.

Prof. Dr. Şinasi Ellialtıoğlu

I certify that I have read this thesis and that in my opinion it is fully adequate, in scope and in quality, as a dissertation for the degree of doctor of philosophy.

Prof. Dr. Ahmet Oral

I certify that I have read this thesis and that in my opinion it is fully adequate, in scope and in quality, as a dissertation for the degree of doctor of philosophy.

Assist. Prof. Dr. Ceyhun Bulutay

I certify that I have read this thesis and that in my opinion it is fully adequate, in scope and in quality, as a dissertation for the degree of doctor of philosophy.

Prof. Dr. Engin U. Akkaya

Approved for the Institute of Engineering and Science:

Prof. Dr. Mehmet B. Baray
Director of the Institute

ABSTRACT

TITANIUM DIOXIDE NANOSTRUCTURES FOR PHOTOCATALYTIC AND PHOTOVOLTAIC APPLICATIONS

Deniz Çakır
PhD. in Physics
Supervisor: Assoc. Prof. Dr. Oğuz Gülseren
August, 2008

In this thesis, TiO_2 nanostructures and their photocatalytic and photovoltaic applications have been investigated by using the first-principles calculations based on density functional theory. We have concentrated on three different systems, namely TiO_2 clusters, nanowires and surfaces. TiO_2 is widely used in various applications, since it is chemically stable in different conditions, firm under illumination, non toxic, and relatively easy and cheap to produce. Most of the technological applications such as photovoltaic and photocatalytic of TiO_2 are mainly related to its optical properties.

First of all, structural, electronic, and magnetic properties of small $(TiO_2)_n$ (n=1–10) clusters have been studied. Various initial geometries for each n have been searched to find out the ground state geometries. In general, it has been found that the ground state structures (for n=1–9) have at least one dangling or pendant O atom. Only the lowest lying structure of n=10 cluster does not have any pendant O atom. In the ground state structures, Ti atoms are at least 4–fold coordinated for $n \geq 4$. Clusters prefer to form three–dimensional and compact structures. All clusters have singlet ground state. The formation energy and HOMO–LUMO gap have also been calculated as a function of the number of TiO_2 unit to study the stability and electronic properties. The formation energy increases with increasing size of the cluster. This means that clusters become stronger as their size grows. The interaction of the ground state structure of each $(TiO_2)_n$ cluster with H_2O has been investigated. The binding energy E_b of H_2O molecule decreases and oscillates as the cluster size increases. The interaction of the ground state structure of n=3, 4, 10 clusters with more than one H_2O molecule has also been studied. We have calculated E_b per adsorbed molecule and we have shown that it decreases with increasing number of adsorbed H_2O

molecule (N). When $N \geq 2$ for n=3 and $N \geq$3 for n=4 clusters, H_2O molecules bind more strongly to n=10 cluster. The adsorption of transition metal (TM) atoms such as V, Co, and Pt on n=10 cluster has been studied as well. All these elements interact with the cluster forming strong chemisorption bonds, and the permanent magnetic moment is induced upon the adsorption of Co or V atoms.

Second of all, structural, electronic and magnetic properties of very thin TiO_x (x=1,2) nanowires have been presented. All stoichiometric TiO_2 nanowires exhibit semiconducting behavior and have non–magnetic ground state. There is a correlation between binding energy (E_b) and the energy band gap (E_g) of these TiO_2 nanowires. In general, E_b increases with E_g. In non-stoichiometric TiO nanowires, we have both metallic and semiconducting nanowires. In addition to non–magnetic TiO nanowires, we have also ferromagnetic nanowires. Three–dimensional (3D) structures are more energetic than planar ones for both stoichiometries. The stability of TiO_x nanowires is enhanced by the increase of the size and coordination number of Ti and O atoms which tend to possess at least four and two nearest neighbors, respectively. We have also studied the structural and electronic properties of rutile (110) nanowires obtained by cutting bulk rutile along the [110] direction with a certain cross section. The bulk nanowires are more energetic than the thin nanowires after a certain diameter. Like thin TiO_2 nanowires, all bulk wires are semiconducting and E_g oscillates with the cross section of these (110) nanowires.

Third of all, we have studied the interaction of perylenediimide (PDI)–based dye compounds (BrPDI, BrGly, and BrAsp) with both the unreconstructed (UR) and reconstructed (RC) anatase TiO_2 (001) surfaces. All dye molecules form strong chemical bonds with the surface in the most favorable adsorption structures. The lowest binding energy is 2.60 eV which has been obtained in the adsorption of BrPDI dye on the UR surface. In UR–BrGly, RC–BrGly and RC–BrAsp cases, we have observed that HOMO and LUMO levels of the adsorbed molecules appear within the band gap and conduction band regions, respectively. Moreover, we have obtained a gap narrowing upon adsorption of BrPDI on the RC surface. Because of the reduction in the effective band gap of the surface–dye system and possibly achieved the visible light activity, these results are valuable for photovoltaic and photocatalytic applications. We have also considered the effects of the hydration of surface on the binding of BrPDI. It has been found that the binding energy drops significantly for the completely hydrated surfaces.

Fourth of all, we have considered the interaction of BrPDI, BrGly, and BrAsp dye molecules with defect free rutile TiO_2 (110) surfaces. All dye molecules form moderate chemical bonds with surface in the most stable adsorption structures. The average binding energy of dye molecules is about 1 eV. Regardless of the type of dye molecules, HOMO and LUMO levels of the adsorbed dye appear within the gap and the conduction band region of defect free surface, respectively. The effect of the slab thickness on the interaction strength between the dye and the surface has also been examined. Unlike the four layers slab, BrGly and BrAsp molecules are dissociatively adsorbed on the three layers slab. The interaction between BrPDI and partially reduced rutile (110) as well as platinized surface has been also considered in order to figure out the effects of O vacancy and preadsorbed small Pt_n (n=1, 3 and 5) clusters on the binding, electronic, and structural properties of the dye–surface system. It has been found that BrPDI dye prefers to bind to the O vacancy site for the partially reduced surface case.

Transition metal deposition on metal oxides plays a crucial role in various industrial areas such as catalysts and photovoltaic cells. Finally, an extensive study of the adsorption of small Pt_n (n=1–8) and bimetallic Pt_2Au_m (m=1–5) clusters on partially reduced rutile TiO_2 (110) has been presented. The effect of surface O vacancies on the adsorption and growth of Pt and bimetallic Pt–Au clusters over the defective site of the 4×2 rutile surface has been studied. Structures, energetics and electronic properties of adsorbed Pt_n and Pt_2Au_m clusters have been analyzed. The surface O vacancy site has been found to be the most active site for a single Pt monomer. Other Pt clusters, namely dimer, trimer and so on, tend to grow around this monomer. As a result, O vacancy site behaves as a nucleation center for the clustering of Pt atoms. Small Pt clusters interact strongly with the partially reduced surface. E_b per adsorbed Pt atom is 3.38 eV for Pt_1 case and E_b increases as the cluster size grows due to the formation of strong Pt–Pt bonds. Pt clusters prefer to form planar structures for n = 1–6 cases. The calculated partial density of states of Pt_n–TiO_2 surface has revealed that the surface becomes metallic when $n \geq 3$. In the case of bimetallic Pt-Au clusters, Au_m clusters have been grown on the Pt_2–TiO_2 surface. Previously adsorbed Pt dimer at the vacancy site of the reduced surface acts as a clustering center for Au atoms. This Pt_2 cluster also inhibits sintering of the Au clusters on the surface. The interaction between the adsorbed Au atoms and titania surface as well as previously adsorbed Pt dimer is weak compared to Pt–TiO_2 surface interactions. Since charge state of the clusters adsorbed on the oxide surfaces is

crucial for catalysis applications of these clusters, total charge on each atom of the metal clusters has also been calculated. Charge transfer among the cluster atoms and underlying oxide surface is more pronounced for Pt_n clusters. Furthermore, the absolute value of total charge on the clusters is greater for Pt_n than that of bimetallic Pt–Au case.

Keywords: First principles, *ab–initio*, density functional theory, titanium dioxide, clusters, nanowires, surfaces, photocatalysis, photovoltaic, dye molecules, light harvesting molecules, dye–sensitized solar cells.

ÖZET

TİTANYUM DİOKSİT TABANLI NANOYAPILARIN FOTOKATALİTİK VE FOTOVOLTAİK UYGULAMALARI

Deniz Çakır
Fizik, Doktora
Tez Yöneticisi: Doç. Dr. Oğuz Gülseren
Ağustos, 2008

Bu çalışmada, titanyum-dioksit tabanlı nanotel, nanoparçacık ve yüzeyler ile bu nano yapıların fotokatalitik ve fotovoltaik uygulamaları yoğunluk fonksiyoneli teorisine dayanan temel prensipler yöntemi kullanılarak incelenmiştir. İlk olarak çok küçük $(TiO_2)_n$ (n=1–10) nano parçacıklarının yapısal, elektronik ve manyetik özellikleri incelendi. n=1–9 topakları için, en düşük enerjili yapılarda en az bir tane yanlızca tek bir Ti atomu ile bağ yapmış O atomu bulunmaktadır. Ti atomunun koordinasyunun veya bir başka deyişle bağ yaptığı atom sayısının artması parçacıkların dayanıklılıklarını artırmaktadır. Nanoparçacıklar en düşük enerjili durumlarında üç boyutlu yapıları tercih etmektedir ve manyetik özellik göstermemektedirler. Bu parçacıkların elektronik özelliklerini ve dayanılıklarını incelemek için, HOMO–LUMO enerji seviyeleri arasindaki fark ve oluşum enerjilerini hesapladık. Parçacık büyüdükçe oluşum enerjiside büyümekte ve daha küçük parçacıklara oranla daha dayanıklı yapılar oluşturmaktadırlar. Deney ortamlarında her zaman H_2O molekülleri bulunduğu için TiO_2 parçacıklarının bu moleküllerle olan etkileşmesi son derece önemlidir. Bu sebeple H_2O molekülü ile en düşük enerjili parçacıklar arasındaki etkileşim incelendi. Parçacıklarin boyutları küçüldükçe H_2O molekülünün bu parçacıklara bağlanma enerjisi (E_b) artmaktadır. Ayrıca n=3, 4, 7, 10 nano parçacıkların birden fazla su molekülü ile olan etkileşimide incelendi. Yapışan su molekülü sayısı artıkça, bu moleküllerin n=10 nano parçacığına diğer daha küçük nano parçacıklara oranla daha kuvvetli bağlandıgı bulundu. Son olarakta n=10 parçacığının geçiş elemetleriyle olan etkileşimi incelendi. Geçiş elementlerinden vanadyum, kobalt ve platinyum çalışıldı. Bu elementler nano parçacıklara çok kuvvetli kimyasal bağlarla bağlanmaktadır. Vanadyum ve kobalt ile n=10 parçacıgının etkileşimleri kalıcı manyetizasyona neden olmaktadır.

İkinci olarak, çok ince TiO_x $(x = 1, 2)$ ve rutile (110) nanotellerinin yapısal, elektronik ve manyetik özellileri incelendi. TiO_2 nanotellerinin tamamı yarı iletken özellik göstermektedir. TiO_2 nanotellerinde manyetizma gözlenmemiştir. Bu stokiyometrik nanotellerin yasak enerji aralıkları ve bağlanma enerjileri arasında çok kuvvetli bir ilişki vardır. Genel olarak bağlanma enerjisi yasak enerji aralığı ile birlikte artmaktadır. Rutile (110) nanotelleride ince TiO_2 nanotelleri ile aynı stokiyometriye sahiptir. Rutile nanotelleri belli bir kesit alanından itibaren ince TiO_2 tellerine göre daha kararlı olmaya başlarlar. Stokiyometrik olmayan ince TiO nanotelleri, stokiyometrik nanotellere göre daha çeşitli özellik göstermektedirler. Hem metallik hemde yarı iletken TiO nanoteller mevcuttur. Ayrıca, bazı TiO telleri manyetik özellikte göstermektedirler. TiO ve TiO_2 tellerinin dayanıklılığı bu telleri oluşturan Ti ve O atomlarının kordinasyonuyla doğrudan ilişkilidir. Atomların kordinasyonun artması tellerin bağlanma enerjisini buna bağlı olarakta dayanıklık artırmaktadır.

Üçüncü olarak, perylenediimid (PDI) tabanlı boya moleküllerinin anatase (001) yüzeyi ile olan etkileşimi incelendi. Boya molekülü olarak BrPDI, BrGly ve BrAsp seçildi. Bu çalışmada hem düz (UR) hemde yeniden yapılanmaya (RC) uğramış (001) yüzeyi kullanıldı. Boya molekülleri iki yüzeyle de güçlü kimyasal bağlar oluşturmaktadır. Örneğin elde edilen en küçük bağlanma enerjisi UR–BrPDI sisteminde 2.60 eV olarak hesaplanmıştır. UR–BrGly, RC–BrGly ve RC–BrAsp sistemlerinde, boya molekülünün HOMO seviyesi yüzeyin yasak enerji aralığının içinde çıkmaktadır. Ayrıca aynı molekülün LUMO seviyeside yüzeyin iletkenlik bandının içindedir. BrPDI molekülü kullanıldığında ise yüzey–boya sisteminin efektif yasak enerji aralığı yüzeyin yasak enerji aralığına göre daha düşüktür. BrAsp ve BrGly moleküllerinin yüzeye tutunması sonucunda yüzey görünür ışığı soğurabilme özelliği kazanmaktadır. Bu da fotovoltaik ve fotokatalitik uygulamaları için çok önemlidir. BrPDI molekülünün önceden su molekülleriyle kaplanmış anatase (001) yüzeyi ile olan etkileşimide çalışıldı ve bu boya molekülünün su bulunmayan temiz yüzeylerle daha kuvvetli etkileştiği bulundu.

Daha sonra, perilen (perylene) tabanlı BrPDI, BrGly ve BrAsp boya moleküllerinin kusursuz rutile (110) yüzeyi ile olan etkileşmeside araştırıldı. Boya moleküllerinin rutile (110) yüzeyi ile olan etkileşmesi anatase (001) yüzeyi ile olan etkileşmesine oranla daha zayıftır. Bu moleküllerin rutile yüzeye bağlanma enerjisi 1 eV civarındadır. Molekülün ne olduğuna bağlı olmaksızın, yapışmış

olan boyanın HOMO seviyesi yasak enerji aralığının içindedir. Ayrıca LUMO seviyeside yüzeyin iletkenlik bandında yeralmaktadır. Yüzey–boya sistemlerinde yüzeyin doğru bir şekilde simülasyonunu yapmak için kullandığımız tabaka kalınlığı önemlidir. 4 katmandan oluşan tabaka rutile (110) yüzeyini ifade etmek için yeterlidir. Ayrıca BrPDI molekülünün kusurlu ve küçük Pt_n (n=1, 3 and 5) nanoparçacıklarının bağlanmış olduğu rutile (110) yüzeyleriyle olan etkileşimide incelendi. Buna göre, boya molekülü yüzeyin kusurlu bölgesine bağlanmayı tercih etmektedir.

Bu tezde son olarak Pt_n (n=1–8) ve Pt_2Au_m (m=1–5) nanoparçacıklarının kusurlu rutile (110) yüzeyi ile olan etkileşimi incelendi. Bu nanoparçacıkların yapısal ve elektronik özellikleri kapsamlı bir şekilde araştırıldı. Pt atomunun yüzeyde bulunduğu en kararlı yer yüzeyin kusurlu bölgesidir. Daha büyük Pt_n nano parçacıklar bu kusurlu bölgeye bağlanmış Pt atomu etrafında büyümektedir. Başka bir deyişle kusurlu bölge Pt nano parçacıklarının büyüme merkezidir. Pt nano parçacıkları ile yüzey arasındaki etkileşim çok kuvvetlidir. Öyleki tek bir Pt atomunun kusurlu bölgeye bağlanma enerjisi 3.38 eV dir. Pt nanoparçacıkları n =1–6 için en düşük enerjili durumda iki boyutlu yapıları tercih etmektedir. Bu nanoparçacıkların yüzeye yapışmasının yüzeyin elektronik özelliklerine ne gibi etkileri olduğuda araştırıldı. Buna göre $n \geq 3$ için Pt_n–yüzey sistemi metallik özellik kazanmaktadır. Son olarak Pt–Au iki metalli nanoparçacıklarının kusurlu rutile (110) yüzeyi ile olan etkileşimi incelendi. Au nanoparçacıkları daha önceden yüzeyin kusurlu bölgesine bağlanmış olan Pt_2 molekülü etrafında büyümektedir. Au atomu Pt atomuna göre yüzeyle, diğer Au ve Pt atomlarıyla daha az etkileşmektedir. Pt_n ve Pt_2Au_m nanoparçacıkları ve bunları meydana getiren atomlar üzerindeki toplam elektriksel yük TiO_2 yüzeylere tutunmuş bu nanoparçacıkların katalizör uygulamalarında çok önemli bir yere sahiptir. Bu nedenle, Pt_n ve iki metallli Pt_2Au_m parçacıkları ve her bir atom üzerindeki toplam yük hesaplandı. Buna göre Pt_n parçacıklarını oluşturan Pt atomları ve yüzey arasında Pt_2–Au_m parçacıklarına oranla daha fazla yük transferi olmaktadır.

Anahtar sözcükler: temel prensipler, *ab–initio*, yoğunluk fonksiyoneli teorisi, titanyum dioksit, nanoparçacıklar, nanoteller, yüzeyler, fotokatalitik, fotovoltaik, boya molekülleri, güneş pilleri.

Anneme, Babama ve Ceyda'ya.

Acknowledgement

I would like to express my gratitude to my supervisor Assoc. Prof. Dr. Oğuz Gülseren for his instructive comments in the supervision of my thesis.

I would like to thank Prof. Dr. Şinasi Ellialtıoğlu, Dr. E. Mete, and Prof. Dr Deniz Üner for valuable and nice discussions.

I appreciate Dr. Ceyhun Bulutay for his morale support and interest.

I would like to thank Dr. Cem Sevik, Dr. Engin Durgun, Rasim Volga Ovalı, Barış Öztop, Onur Umucalılar, Sevil Özer, Sefaettin Tongay, Dr. Sefa Dağ, Dr. Haldun Sevinçli, Sevilay Sevinçli, Hasan Şahin and Dr. Kerim Savran for their help and invaluable friendship. I will always remember the good and hard times that we shared together.

I would like to thank my friends Turgut Tut, Emre Taşkın, A. Levent Subaşı, Dr. Aşkın Kocabaş, Dr. Mehrdad Atabak, Dr. Sinem Binicioğlu, Dündar Yılmaz, Seymur Cahangirov, Can Ataca, Mehmet Topsakal, Ümit Keleş and Cem Murat Turgut.

I would like to thank my family for their great support.

And finally, I am grateful to Ceyda for her great morale support and help at every time.

Part of the calculations has been carried out at UNAM National Nanotechnology Center Project computational facilities, ULAKBIM Computer Center and UYBHM at Istanbul Technical University .

Contents

List of Figures

List of Tables

Chapter 1

INTRODUCTION

Nanoscience is a multi disciplinary field comprising the applied physics, biology, chemistry, material science, chemical engineering, mechanical engineering, biotechnology, and electrical engineering and so on. There is an exponential growth on nanoscience and nanotechnology research activities. One nanometer (nm) is one billionth, or 10^{-9} of a meter. For comparison, in a gold dimer, interatomic distance is about 0.25 nm and DNA double-helix has a diameter around 2 nm. As the size of the system decreases, several physical phenomena become noticeably pronounced. These include statistical mechanical and quantum mechanical effects, for instance quantum size effect where the electronic properties of solids are altered with great reductions in particle size. This effect does not come into play by going from macro to micro dimensions. However, it becomes dominant when the nanometer size range is reached. Surface to volume ratio increases dramatically as the size of a material decreases. Additionally, mechanical, electrical, optical, structural and chemical properties of a material change when its size reduces from macro to micro, mainly because of quantum size effects. Materials in nanoscale can suddenly exhibit very different properties compared to what they exhibit on a macroscale. For instance, inert materials become catalysts (platinum and gold); insulators become conductors (silicon). Gold is a chemically inert material in macroscale. However, it can serve as a potential chemical catalyst at nanoscale. Nanoparticles and clusters are extensively used

in chemical catalysis, due to the extremely large surface to volume ratio. The potential applications of these low dimensional structures in catalysis reactions range from fuel cell to catalytic converters and photocatalytic devices. Catalysis is also important for the production of chemicals.

Titanium dioxide (TiO_2) is the potential material for both macro and microscale applications and has been a focus of attention because of its low cost, stability under illumination and its environmentally friendly applications [1, 2, 3]. It has various application areas including production of hydrogen from water and solar energy, used in solar cells (as an active semiconductor metal oxide in Grätzel solar cell) [4, 5, 6, 7], cleaning of water and air from organic pollutants, self-cleaning coatings, pigments, sunscreens, toothpaste, photocatalysis [8, 9, 10, 11] and sensors [12]. In nature, TiO_2 exists mainly in three types of crystal structures. These are rutile, anatase and brookite. Rutile is the thermodynamically most stable phase under ambient conditions. TiO_2 is a large band gap semiconductor (3 eV for rutile and 3.2 eV for anatase) and absorbs only ultraviolet (down to $\sim$ 400 nm) portion of the solar spectrum. This property reduces the efficiency of solar energy conversion. There are extensive efforts to achieve the visible light activity of TiO_2 through doping or substitution with impurities, for instance, C, N, F, P, or S of oxygen atom in the titania lattice [13, 14, 15, 16, 17, 18, 19].

In 1972, photocatalytic splitting of water on TiO_2 under ultraviolet light has been observed by Fujishima and Honda [8]. After then, enormous efforts have been devoted to the research on TiO_2 based materials, which has led to important applications such as photovoltaics and photocatalysis. Catalysis under light irradiation, called photocatalysis, is attracting a great deal of attention from the point view of fundamental science and applications for practical uses. The photocatalytic application principles of a semiconductor is straightforward. First, a photon with energy larger than band gap (E_g) TiO_2 is absorbed. Electrons are excited from valance band to conduction band, creating electron-hole pairs. These charges migrate to the surface and react with the chemicals adsorbed by the surface of TiO_2 to decompose these chemicals. Intermediate species such as OH, O^{2-}, H_2O_2 or O_2 are usually involved in these photodecomposition process. Photocatalytic activity of a semiconductor depends on several factors: (1) light absorbtion

spectrum and coefficient, (2) reduction and oxidation rate on the surface by the electrons and holes, (3) recombination rate of electron-hole pair. Surface area has effects on speed and efficiency of photocatalysis phenomena. The larger specific surface area, the higher the photocatalytic activity is. Surfaces which have defects behave as recombination centers. Crystallinity reduces the number of bulk defects and these cause higher catalytic activity. Therefore, to achieve faster and more efficient photocatalytic reaction, a balance must be obtained among several factors which influence the photocatalysis processes. Photocatalytic ability of TiO_2 is also used to kill bacteria and tumor cells in cancer treatment.

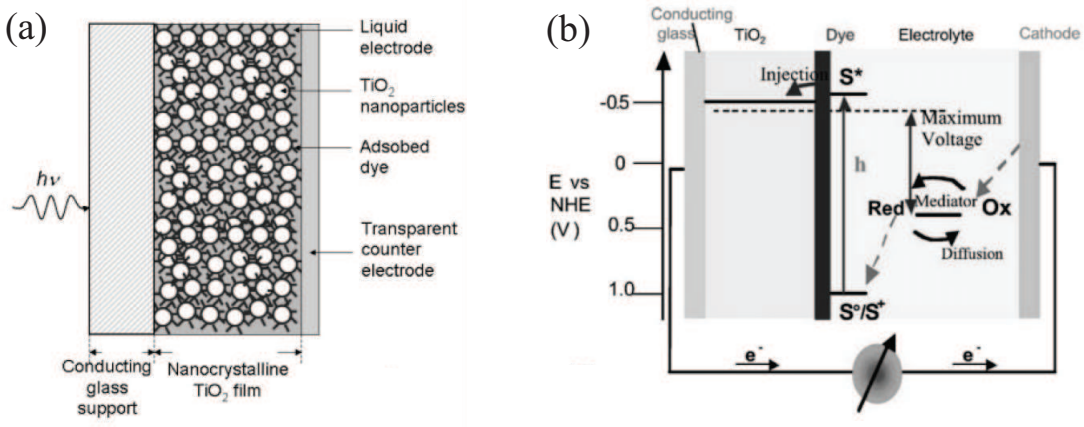

Figure 1.1: (a) Structure and (b) principle of operation and energy level scheme of the dye-sensitized nanocrystalline solar cell. Photoexcitation of the sensitizer (S) is followed by electron injection into the conduction band of an oxide semiconductor film. The dye molecule is regenerated by the redox system, which itself is regenerated at the counterelectrode by electrons passed through the load. Potentials are referred to the normal hydrogen electrode (NHE). The open circuit voltage of the solar cell corresponds to the difference between the redox potential of the mediator and the Fermi level of the nanocrystalline film indicated with a dashed line. The energy levels drawn for the sensitizer and the redox mediator match the redox potentials of the doubly deprotonated N3 sensitizer ground state and the iodide/triiodide couple. Reprinted from Grätzel, M. J. Photochem. Photobiol. A: Chem. **164**, 3 (2004).

Photovoltaic is another important application area of TiO_2. Research on renewable energy sources help to overcome possible energy crisis in future. Solar energy is an unlimited and clean energy. Solar cells are photovoltaic devices in which light are converted to electricity. Although, silicon based solar cells are capable of stable and efficient solar energy conversion, their production is expensive. Therefore, a great deal of effort has been conducted to developing cheap and efficient solar cells. Dye-sensitized solar cells (DSSC) [4] has been a focus of attention because of their potential low cost and relatively high power conversion efficiency. TiO_2 is widely used in DSSC as an active semiconductor metal oxide because it is chemically stable in different conditions, stable under illumination, non toxic and relatively easy and cheap to produce. A schematic presentation of the structure and operating principles of the DSSC is given in Figure 1.1.

The optical response of TiO_2 to sunlight from the UV to the visible region can be extended substantially by adsorbing dye molecules on the semiconductor surface. This is the basic idea behind dye-sensitized solar cells. The dyes are the light-harvesting organic or inorganic molecules, which capture the energy of the sunlight, and the absorption of photons leads to excitation of an electron from a low-energy state into a high-energy state of the dye. The excited electron can then rapidly be injected into the semiconductor. This charge injection must be fast enough to prevent the reduction of oxidized dyes. Then, the following charge transfer, to the back-electrode, takes place in the semiconductor, and in this way the absorption is separated from the charge transport. This concept, letting the process of light absorption be separated from the charge transport, differentiates this type of solar cells from the conventional silicon based solar cell. The major advantage of DSSC is the fact that the conduction mechanism is based on majority carrier transport. This means that bulk or surface recombination of carriers in the TiO_2 cannot occur. It has been shown that dye-sensitized solar cells are able to attain efficiencies close to 11 % [7].

The dyes are the key components of the DSSC. Ruthenium-based dye complexes are used in solar cell devices because of their high efficiency in sensitizing TiO_2 nanocrystalline particles. These rare earth metal dyes exhibit excellent light harvesting, fast charge injection kinetics, and long-term molecular stability under

various environmental conditions. Figure 1.2(a) shows the commercially available $[Ru(Bpy)_3]^{2+}$ (RuBpy) dye complex. HOMO level of these dyes is populated by Ru t_{2g} symmetry orbitals: d_{xy}, d_{xz}, and d_{yz}. Carboxylic or phosphoric acid groups can be added to RuBpy to design new functional dyes. It is known that dyes are anchored to semiconductor surface through their carboxyl groups. As the number of the carboxyl groups increase in the dye sensitizers, the electron-transfer efficiencies increase due to their better anchoring to the surface. The stability of the DSSC over time and temperature ranges under various conditions is the most important issue. Interaction between the metal oxide surface and dyes must be strong enough.

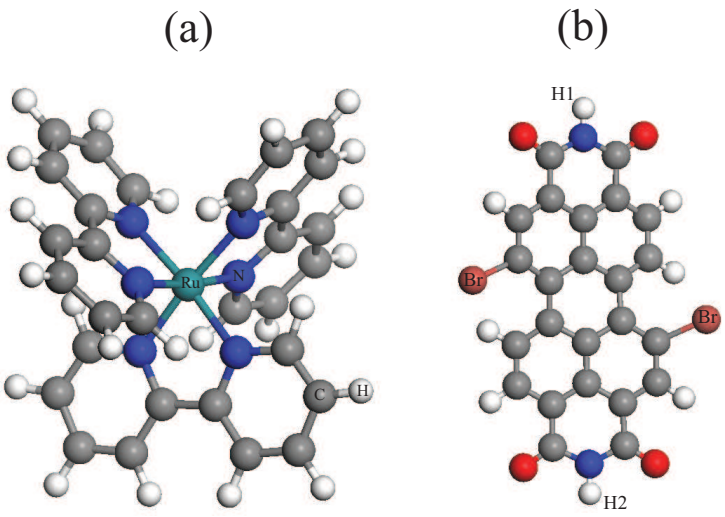

Figure 1.2: Molecular structure of the dye molecules (a) RuBpy and (b) BrPDI. H1 and H2 atoms can be replaced by various chemical groups such as carboxyl group (CH_2COOH) for possible functionalization of these dyes.

Perylenediimide (PDI)–based dye compounds are also potential candidates for DSSC. Figure 1.2(b) presents the structure of BrPDI. These dyes are stable at their ground states and sensitive to visible light. Like RuBpy, several different PDI molecules are obtained by adding carboxyl groups to the dye. BrGly and BrAsp dyes are synthesized by replacing the two H atoms of dye with two glycine and aspartine groups, respectively.

In this context, first-principles studies of TiO_2 based 0D, 1D, and 2D structures are important. The main purpose of this study is to clarify and model the structural, electronic, magnetic properties of these materials. Functionalization of these material are discussed for possibility of real device applications.

The organization of the thesis is as follows : After Introduction part, the theory and methodology used in calculations is briefly discussed in Chapter 2 by leaving details to related references. Structural, electronic and magnetic properties of TiO_2 clusters and nanowires are given in Chapter 3 and Chapter 4, respectively. In the following three chapters, we discuss the TiO_2 anatase (001) and rutile (110) surfaces and their interactions with perylene based dye molecules (BrPDI, BrGly, and BrAsp) and metal atoms (Pt and Au) for the DSSC and photocatalytic applications. Anatase–dye and rutile–dye systems are presented in Chapter 5 and Chapter 6, respectively. Interaction of Pt and bimetallic PtAu clusters with partially reduced rutile TiO_2 (110) surface is analyzed in Chapter 7. In Chapter 8 as a Conclusion part, the obtained results are briefly summarized.

Chapter 2

THEORETICAL BACKGROUND

In this chapter, we will present the theoretical approaches and approximations which are used in standard Density Functional Theory (DFT) based methods. The details of the theory can be obtained from the several reviews and books [20, 21, 22].

2.1 The problem of structure of matter

The microscopic description of the physical and chemical properties of matter is a very complex problem. In general, we deal with a collection of interacting atoms, which may also be affected by some external field. This ensemble of particles may be in the gas phase (molecules and clusters), or in a condensed phase (solids, surfaces, wires). However, in all cases we can certainly describe the system by a number of nuclei and electrons interacting through electrostatic forces. The Hamiltonian of such a system can be written in the following general form:

$$H = \sum_{I=1}^{N} \frac{\vec{P_I}^2}{2M_I} + \sum_{i=1}^{N_e} \frac{\vec{p_i}^2}{2m} + \sum_{i>j} \frac{e^2}{|\vec{r_i} - \vec{r_j}|} + \sum_{I>J} \frac{Z_I Z_J e^2}{\mid \vec{R_I} - \vec{R_J} \mid} - \sum_{i,I} \frac{Z_I e^2}{|\vec{R_I} - \vec{r_i}|}, \quad (2.1)$$

where $R = R_N$, $N = 1...N$, is a set of N nuclear coordinates, and $r = r_{N_e}$, $i = 1...N_e$, is a set of N_e electronic coordinates. Z_I and M_I are the N nuclear charges and masses, respectively. Electrons are fermions, so that the total electronic wave function must be antisymmetric with respect to exchange of two electrons. Nuclei can be fermions, bosons or distinguishable particles, according to the particular problem under examination. All the ingredients are perfectly known and, in principle, all the properties can be derived by solving the many-body Schrödinger equation:

$$\widehat{H}\Phi(x, \vec{R}) = E\Phi(x, \vec{R}), \quad (2.2)$$

where $x \equiv (\vec{r}, s)$ full set of electronic positions and spin variables. In practice, this problem is almost impossible to treat in a full quantum mechanical framework. Only in a few cases a complete analytic solution is available, and numerical solutions are also limited to a very small number of particles. There are several features that contribute to this difficulty. First, this is a multicomponent many–body system, where each component (each nuclear species and the electrons) obeys a particular statistics. Second, the complete wave function cannot be easily factorized because of coulombic correlations. In other words, the full Schrödinger equation cannot be easily decoupled into a set of independent equations so that, in general, we have to deal with $(3N + 3N_e)$ coupled degrees of freedom. The dynamics is an even more difficult problem, and very few and limited numerical techniques have been proposed to solve it. The usual choice is to find out some proper approximations. The large majority of the calculations presented in the literature starts with: (1) the adiabatic separation of nuclear and electronic degrees of freedom (adiabatic approximation), and (2) the classical treatment of the nuclei.

2.2 Adiabatic approximation (Born–Oppenheimer)

Since the electrons are so much lighter and faster than the nuclei, the electrons can follow instantaneously the motion of the nuclei which stay always in the same stationary state of the electronic Hamiltonian. This is called the Born–Oppenheimer approximation [23]. This stationary state will vary in time because of the coulombic coupling of the two sets of degrees of freedom but, if the electrons were, e.g. in the ground state, they will remain there forever. This means that as the nuclei follow their dynamics, the electrons instantaneously adjust their wave function according to the nuclear wave function. Under the above conditions, the full wavefunction factorizes in the following way:

$$\Phi(x, \vec{R}) = \Psi(x, \vec{R})\chi(\vec{R}), \tag{2.3}$$

where $\Psi(x, \vec{R})$ is the electronic wave function, $\chi(\vec{R})$ is the nuclear wave function. $\Psi(x, \vec{R})$ is more localized than $\chi(\vec{R})$. That is $\nabla_I \chi(\vec{R}) \gg \nabla_I \Psi(x, \vec{R})$, and moreover $\Psi(x, \vec{R})$ is normalized for every R. So this separation of variables leads to

$$[T_e + V_{ee}(\vec{r}) + V_{eN}(\vec{r}, \vec{R})]\Psi_n(x, \vec{R}) = \varepsilon_n(\vec{R})\Psi_n(x, \vec{R}), \tag{2.4}$$

and

$$[T_N + V_{NN}(\vec{R}) + \varepsilon(\vec{R})]\chi(\vec{R}) = E_n(\vec{R})\chi(\vec{R}). \tag{2.5}$$

Electronic eigenvalue $\varepsilon_n(\vec{R})$ depends parametrically on the ionic positions $\vec{R}$. In Adiabatic approximation, ions move on the potential–energy surface of the electronic ground state only.

$$[T_e + V_{ee}(\vec{r}) + V_{eN}(\vec{r}, \vec{R})]\Psi_0(x, \vec{R}) = \varepsilon_0(\vec{R})\Psi(x, \vec{R}), \tag{2.6}$$

and

$$[T_N + V_{NN}(\vec{R}) + \varepsilon(\vec{R})]\chi(\vec{R}) = i\hbar\frac{\partial}{\partial t}\chi(\vec{R}, t). \tag{2.7}$$

2.3 Classical nuclei approximation

Solving Eq. 2.6 or 2.7 is a difficult task for two reasons: First, it is a many-body equation in the $3N$ nuclear coordinates, the interaction potential being given in an implicit form. Second, the determination of the potential energy surface $\varepsilon_n(\vec{R})$ for every possible nuclear configuration R involves solving M^{3N} times the electronic equation, where M is, e.g., a typical number of grid points. The largest size achieved up to date using non–stochastic methods is six nuclear degrees of freedom. In a large variety of cases of interest, however, the solution of the quantum nuclear equation is not necessary. This is based on two observations: (1) The thermal wavelength for a particle of mass M is $T = \frac{e^2}{Mk_BT}$ so that regions of space separated by more than $\lambda_T \simeq 0.1$ Å do not exhibit quantum phase coherence. The least favorable case is that of hydrogen, and even so, at room temperature $\lambda_T \simeq 0.1$ Å , while interatomic distances are normally of the order of 1 Å. (2) Potential energy surfaces in typical bonding environment are normally stiff enough to localize the nuclear wave functions to a large extent. For instance, a proton in a hydroxyl group has a width of about 0.25 Å. This does not mean that quantum nuclear effects can be neglected altogether. In fact, there is a variety of questions in condensed matter and molecular physics which require a quantum mechanical treatment of the nuclei. Well–known examples are the solid phases of hydrogen, hydrogen–bonded systems like water and ice, fluxional molecules, and even active sites of enzymes. There is, however, an enormous number of systems where the nuclear wave packets are sufficiently localized to be replaced by Dirac's δ–functions. The connection between quantum and classical mechanics is achieved through Ehrenfest's theorem for the mean values of the position and momentum operators. The quantum-mechanical analog of Newton's equations is:

$$\frac{\langle \partial^2 \vec{P}_I \rangle}{\partial t^2} = -\langle \nabla_I E_0(\vec{R}) \rangle, \tag{2.8}$$

and

$$E_0(\vec{R}) = \varepsilon_0(\vec{R}) + V_{NN}(\vec{R}). \tag{2.9}$$

Force $-\nabla_I E_0(\vec{R})$ contains contributions from direct ion–ion interaction and from the gradient of the electronic total energy.

2.4 Hartree and Hartree–Fock approximation

Solving the Schrödinger equation of a system of N_e interacted electrons in the external coulombic field created by a collection of atomic nuclei is a very difficult scheme. The exact solution is known only in the case of uniform electron gas, for atoms with a small number of electrons, and for a few small molecules. These exact solutions are always numerical. At the analytical level, approximations must be used. The first approximation may be considered the one proposed by Hartree [24]. It consists of postulating that the many–electron wave function can be written as a simple product of one–electron wave functions. Each of these then satisfies a one-particle Schrödinger equation in an effective potential that takes into account the interaction with the other electrons in a mean field way:

$$\Psi(x, \vec{R}) = \prod_i \phi_i(\vec{r_i}), \tag{2.10}$$

and

$$\left(-\frac{\hbar^2}{2m}\nabla^2 - \frac{Ze^2}{r} + \int \frac{\sum_{j\neq i} |\phi_j(\vec{r'})|^2}{|\vec{r} - \vec{r'}|} d^3r' \right) \phi_i(\vec{r}) = \varepsilon_i \phi_i(\vec{r}), \tag{2.11}$$

where third term in left hand side is the Hartree potential. Sum of the second and the third term is the effective potential. Notice that charge density $n_j = |\phi_j|^2$ does not include the charge associated with particle i, so that the Hartree approximation is (correctly) self-interaction free. In this approximation, the energy of the many-body system is not just the sum of the eigenvalues of Eq. 2.11 because the formulation in terms of an effective potential makes the electron–electron interaction counted twice. The correct expression for the energy is:

$$E^H = \sum_i^{N_e} \varepsilon_i - \frac{1}{2} \int\int \frac{n(\vec{r})n(\vec{r'})}{|\vec{r} - \vec{r'}|} d^3r d^3r' = \frac{\langle \Psi | H | \Psi \rangle}{\langle \Psi | \Psi \rangle}. \tag{2.12}$$

The set of N_e coupled partial differential equations can be solved by minimizing the energy with respect to a set of variational parameters in a trial wave function $\delta \frac{\langle \widetilde{\Psi} | H | \widetilde{\Psi} \rangle}{\langle \widetilde{\Psi} | \widetilde{\Psi} \rangle} = 0$ or, alternatively, by recalculating the electronic densities using the solutions of Eq. 2.11, then calculating the potential, and solving again the

Schrödinger equation.This procedure can be repeated several times, until self-consistency in the initial and final wave function or potential is achieved. This procedure is called self-consistent Hartree approximation. The Hartree approximation treats the electrons as distinguishable particles. The wave function of a many electron system must be antisymmetric under exchange of two electron because the electrons are fermions. The antisymmetry of the wave function produces a spatial separation between electrons that have the the same spin and thus reduces the Coulomb energy of the electronic system. Slater determinant is the way to make antisymmetrized many electron wave function by using Pauli exclusion principle (Fermi statistics for electrons) [25]:

$$\Psi_{i_1 \ldots i_{N_e}}(q_1 \ldots q_{N_e}) = \frac{1}{\sqrt{N_e}} \begin{pmatrix} \phi_{i_1}(q_1) & \ldots & \phi_{i_{N_e}}(q_{N_e}) \\ \vdots & & \vdots \\ \phi_{i_1}(q_1) & \ldots & \phi_{i_{N_e}}(q_{N_e}) \end{pmatrix} \tag{2.13}$$

$$= \frac{1}{\sqrt{N_e}} \sum_P (-1)^P P \phi_{i_1}(q_1) \ldots \phi_{i_{N_e}}(q_{N_e}). \tag{2.14}$$

This wave function allows particle exchange due to the antisymmetry of wave function. The energy of the system is reduced by this exchange of particles (electrons). The approximation is called Hartree–Fock (HF) and has been for a long time the way of choice of chemists for calculating the electronic structure of molecules [26]. In fact, it provides a very reasonable picture for atomic systems and, although many–body correlations (arising from the fact that, due to the two–body Coulomb interactions, the total wave function cannot necessarily be separated as a sum of products of single–particle wave functions) are completely absent, it also provides a reasonably good description of interatomic bonding. Hartree–Fock equations look the same as Hartree equations, except for the fact that the exchange integrals introduce additional coupling terms in the differential

equations:

$$\Big(-\frac{\hbar^2}{2m}\nabla^2 - \frac{Ze^2}{r} + e^2 \sum_{i\neq j} \int \frac{|\phi_j(\vec{r'})|^2}{|\vec{r}-\vec{r'}|} d^3r' \Big)\phi_i(\vec{r}) \\ - e^2 \sum_{j\neq i} \int \frac{\phi_j^\star(\vec{r'})\phi_i(\vec{r})}{|\vec{r}-\vec{r'}|} d^3r' \phi_j(\vec{r}) = \varepsilon_i \phi_i(\vec{r}). \tag{2.15}$$

Notice that also in HF the self–interaction cancels exactly.

2.5 Thomas-Fermi theory

Thomas and Fermi proposed [27, 28], at about the same time as Hartree (1927-1928), that the full electronic density was the fundamental variable of the many-body problem, and derived a differential equation for the density without using to one-electron orbitals. The Thomas-Fermi approximation was actually too incomplete because it did not include exchange and correlation effects, and was also unable to sustain bound states because of the approximation used for the kinetic energy of the electrons. However, it set up the basis for the later development of Density Functional Theory (DFT), which has been the way of choice in electronic structure calculations in condensed matter physics during the past twenty years.

Thomas and Fermi (1927) gave a way for constructing the total energy in terms of only the electronic density. They used the expression for the kinetic, exchange and correlation energies of the homogeneous electron gas to construct the same quantities for the inhomogeneous system in the following way $E_i = \int \varepsilon_i[n(\vec{r})]dr$ where $\varepsilon_i \sim \varepsilon_i[n(\vec{r})]$ is the energy density (corresponding to the piece i), calculated locally for the value of the density at that point in space. This was the first time that the local density approximation, or LDA, was used. For the homogeneous electron gas the density is related to the Fermi energy (ε_F) by

$$n = \frac{1}{3\pi^2}\left(\frac{2m}{\hbar^2}\right)^{3/2} \varepsilon_F^{3/2}. \tag{2.16}$$

The kinetic energy density of the homogeneous gas is $T = \frac{3n\varepsilon_F}{5}$, so that the kinetic energy density is:

$$T[n] = \frac{3}{5}\frac{\hbar^2}{2m}(3\pi^2)^{3/2}n^{3/2}. \tag{2.17}$$

The kinetic energy is written,

$$T^{TF} = C_K \int n^{5/3}(\vec{r})dr, \tag{2.18}$$

with $C_K = 3(3\pi^2)^{2/3}/10$. The inhomogeneous system is thought of as locally homogenous. Neglecting exchange and correlation in total energy expression we obtain Thomas - Fermi theory:

$$E_{TF}[n] = C_K \int n^{5/3}(\vec{r})d^3r + \int v(\vec{r})n(\vec{r})d^3r + \frac{1}{2}\int\int \frac{n(\vec{r})n(\vec{r'})}{|\vec{r}-\vec{r'}|}d^3rd^3r'. \tag{2.19}$$

It can be seen that E_{TF} depends only on the electronic density, it is a functional of the density. By using variational principle, one can obtain the density $n(r)$ which minimizes E_{TF} subjected to the constraint that the total integrated charge be equal to the number of electrons. This can be put in terms of functional derivatives:

$$\frac{\delta}{\delta n(\vec{r})}\left(E_{TF} - \mu\int n(\vec{r})dr\right) = 0, \tag{2.20}$$

with

$$\mu = \frac{5}{3}C_K n^{2/3}(\vec{r}) + v(\vec{r}) + \int \frac{n(\vec{r'})}{|\vec{r}-\vec{r'}|}d^3r, \tag{2.21}$$

where μ is the chemical potential.

Hartree equation described the ground states better than Thomas–Fermi theory. The differences between them lay in the different treatments of the kinetic energy T.

2.6 Density Functional Theory

The initial work on DFT was reported in two publications: first by Hohenberg-Kohn in 1964 [29], and the next by Kohn–Sham in 1965 [30]. The Coulomb energy of the electronic system can be reduced below its Hartree–Fock value if electrons that have the opposite spins are also spatially separated. In this case the Coulomb energy of the electronic system is reduced at the cost of increasing the kinetic energy of the electrons. The differences between the many body energy of an electronic system and the energy of the system calculated in the HF approximation is called the correlation energy. Hohenberg and Kohn proved that the total energy, including exchange and this correlation energy, of an electron gas, even under the influence of an external static potential, for our case the potential due to ions, is a unique functional of the electron density. Further, the minimum value of the total energy functional is the ground-state energy of the system, and the density that yields this minimum value is the exact ground state energy. In addition to this, Kohn and Sham showed how to replace the many–electron problem by an exactly equivalent set of self-consistent one electron equations. Self-consistent here means that the solutions determine the equations themselves.

The important distinction between Hartree–Fock approximation and the Hohenberg–Kohn theory is the initial approach to the problem. Hartree–Fock method initially approximates a set of single–electron wave functions, anti- symmetrized by the Slater determinant approach and minimizes the total energy in terms of these functions. However, in the density functional theory, the total energy is introduced as a functional of the charge density, which is introduced ad–hoc to the system. The charge density later is definable as the sum of single–electron densities, whence the derivation of total energy with respect to the charge density yields the Kohn–Sham equations.

2.6.1 Hohenberg–Kohn Theory

In 1964, P. Hohenberg and W. Kohn formulated and proved a theorem on the ground of Thomas-Fermi theory. The theorem is divided into two parts:

1. The ground–state energy of a many body system is a unique functional of the particle density, $E_0 = E[n(\vec{r})]$. There is no $v(r) \neq v'(\vec{r})$(external potential) that corresponding to the same electronic density for the ground state.

2. The functional $E[n(\vec{r})]$ has its minimum relative to variations $\delta n(r)$ of the particle density at equilibrium density $n_0(\vec{r})$.

$$E = E[n_0(\vec{r})] = \min\ E[n(\vec{r})]. \tag{2.22}$$

2.6.2 The Hohenberg–Kohn variational principle

The most important property of an electronic ground state is its energy. By wave function methods E could be calculated by direct approximate solution of the Schrödinger equation or the Rayleigh–Ritz minimal principle,

$$E = \min(\widetilde{\Psi}, H\widetilde{\Psi})_{\widetilde{\Psi}}, \tag{2.23}$$

where $\widetilde{\Psi}$ is a normalized trial wave function for the given number of electrons N_e.

The formulation of minimal principle in terms of trial densities $n(r)$, rather than trial wave function $\widetilde{\Psi}$ was first presented in Hohenberg–Kohn (1964) [29].

Every trial function $\widetilde{\Psi}$ corresponding to a trial density $n(r)$ obtained by integrating $\widetilde{\Psi}\widetilde{\Psi^\star}$ over all variables. One may carry out the minimization in two stages. First fix trial density and denote $\widetilde{n}$. We define the constrained energy minimum, with n fixed, as

$$E_v[\widetilde{n}(\vec{r})] \equiv \min\,(\widetilde{\Psi^i_{\widetilde{n}}}, H\widetilde{\Psi^i_{\widetilde{n}}})_i = \int v(\vec{r})\widetilde{n}(\vec{r})dr + F[n(\vec{r})], \tag{2.24}$$

where

$$F[\widetilde{n}(\vec{r})] = \min\,[\widetilde{\Psi^i_{\widetilde{n}}}, (T+U)\widetilde{\Psi^i_{\widetilde{n}}}]_i. \tag{2.25}$$

$F[n(\vec{r})]$ requires no explicit knowledge of $v(r)$. It is a universal functional of the density $\widetilde{n}(r)$.

2.6.3 The self-consistent Kohn–Sham equations

$$E_{v(\vec{r})}(\widetilde{n}(\vec{r})) \equiv \int v(\vec{r})\widetilde{n}(\vec{r})dr + T[\widetilde{n}(\vec{r})]. \tag{2.26}$$

The Euler–Lagrange equations, embodying the fact the expression $n(\vec{r}) = \sum_i^{N_e} |\varphi_i(\vec{r})|^2$ is stationary with respect to variations of $\widetilde{n}(\vec{r})$ which leave the total number of electrons unchanged, is

$$\delta E_{v(\vec{r})}[\widetilde{n}(\vec{r})] = \int \delta\widetilde{n}(\vec{r}) \left(v(\vec{r}) + \frac{\delta}{\delta\widetilde{n}(\vec{r})} T[\widetilde{n}(\vec{r})]|_{\widetilde{n}\equiv n} - \varepsilon \right) dr, \tag{2.27}$$

where $\widetilde{n}(\vec{r})$ is the exact ground–state density for $v(r)$. Here ε is a Lagrange multiplier to assure particle conservation. Now in this soluble, noninteracting case, the ground state energy and density can be obtained by calculating the eigenfunctions φ_i and eigenvalues ε_i of noninteracting single-particle equations

$$\left(-\frac{\hbar^2}{2m}\nabla^2 + v(\vec{r}) - \varepsilon_i \right) \varphi_i = 0, \tag{2.28}$$

yielding

$$E = \sum_{i=1}^{N_e} \varepsilon_i, \tag{2.29}$$

and

$$n(\vec{r}) = \sum_{i}^{N_e} |\varphi_i(\vec{r})|^2. \tag{2.30}$$

Here i labels both orbital quantum numbers and spin.

The Kohn–Sham total energy functional for a set of doubly occupied electronic

state φ_i can be written

$$E[n(\vec{r})] = \int v(\vec{r})n(\vec{r})d^3r + F[n(\vec{r})], \tag{2.31}$$

where functional $F[\widetilde{n}(\vec{r})]$ is written in the form of

$$F[\widetilde{n}(\vec{r})] = T[\widetilde{n}(\vec{r})] + \frac{1}{2}\int\int \frac{\widetilde{n}(\vec{r})\widetilde{n}(\vec{r'})}{|\vec{r}-\vec{r'}|}d^3rd^3r' + E_{XC}[\widetilde{n}(\vec{r})]. \tag{2.32}$$

Here, $T[\widetilde{n}(\vec{r})]$ is the kinetic energy functional for noninteracting electrons and is in form of

$$T[n(r)] = 2\sum_i \int \varphi_i \left[-\frac{\hbar^2}{2m}\nabla^2\right]\varphi_i \, d^3r. \tag{2.33}$$

The last term is the exchange–correlation energy functional. The corresponding Euler–Lagrange equation, for a given total number of electrons, has the form

$$\delta E_{v(\vec{r})}[\widetilde{n}(\vec{r})] = \int \delta\widetilde{n}(\vec{r}) \left(v_{eff}(\vec{r}) + \frac{\delta}{\delta\widetilde{n}(\vec{r})}T[\widetilde{n}(\vec{r})]|_{\widetilde{n}(\vec{r})=n(\vec{r})} - \varepsilon\right) d^3r = 0, \tag{2.34}$$

with

$$v_{eff}(\vec{r}) = v(\vec{r}) + \int \frac{n(\vec{r'})}{|\vec{r}-\vec{r'}|}d^3r' + v_{XC}(\vec{r}), \tag{2.35}$$

and

$$v_{XC} \equiv \frac{\delta}{\delta\widetilde{n}(\vec{r})}E_{XC}[\widetilde{n}(\vec{r})]|_{\widetilde{n}(\vec{r})=n(\vec{r})}. \tag{2.36}$$

The form of Eq. 2.31 is identical to Eq. 2.26 for noninteracting particles moving in an effective external potential v_{eff} instead of $v(\vec{r})$ and the minimizing density $n(\vec{r})$ is given by solving the single particle equation

$$\left(-\frac{\hbar^2}{2m}\nabla^2 + v_{eff} - \varepsilon_i\right)\varphi_i = 0. \tag{2.37}$$

These self-consistent equations are called the Kohn–Sham (KS) equations and the ground state energy is given by

$$E = \sum_i \varepsilon_i + E_{XC}[n(\vec{r})] - \int v_{XC}n(\vec{r})d^3r - \frac{1}{2}\int \frac{n(\vec{r})n(\vec{r'}))}{|\vec{r}-\vec{r'}|}d^3rd^3r'. \tag{2.38}$$

If E_{XC} and v_{XC} is neglected, the Kohn–Sham equations reduce to self consistent Hartree equations. With the exact E_{XC} and v_{XC} all many body effects are in principle included. The Kohn–Sham equations must be solved self consistently so that the occupied electronic states generate a charge density that produces the electronic potential that was used to construct the equations.

2.7 Functionals for Exchange and Correlation

In DFT, E_{XC} is a very complicated term and explicit form of this functional is not known. Therefore, we must introduce some approximations and assumptions for this term to use DFT as a reliable tool for computational physics, biology and chemistry. The quality of the density functional approach thus depends on the accuracy of the chosen approximation to E_{XC}. In the exchange-correlation functionals approximations, the main idea is how the electron density is treated in the total energy calculations.

2.7.1 Local Spin Density Approximation (LSDA)

Kohn–Sham pointed out that solids can often be considered as close to the limit of the homogeneous electron gas. In that limit, the effects of exchange and correlation are local in character. In local density approximation (LDA) [31] or more generally local spin density approximation (LSDA), the exchange-correlation is simply an integral over all space with the exchange-correlation energy density at each point assumed to be the same as in a homogeneous electron gas with that density,

$$E_{xc}^{LSDA}[n^{\uparrow}, n^{\downarrow}] = \int d^3 r n(r) \varepsilon_{xc}^{hom}(n^{\uparrow}(\mathbf{r}), n^{\downarrow}(\mathbf{r})). \tag{2.39}$$

The LSDA is the most general local approximation and is given explicitly for exchange and by approximate expressions for correlation. For unpolarized systems LDA is simply found by setting $n^{\uparrow}(\mathbf{r}) = n^{\downarrow}(\mathbf{r}) = n(\mathbf{r})/2$.

Once one has made the local ansatz of the L(S)DA, then all the rest follows. Since the functional E_{xc} is universal, it follows that it is exactly the same as for the homogeneous gas. The only information needed is the exchange-correlation energy of the homogeneous gas as a function of density. The rationale for the local approximation is that for the densities typical of those found in solids where the range of effects of exchange and correlation is rather short. It is expected to be best for solids close to a homogeneous gas and worst for very inhomogeneous cases like atoms where the density must go continuously to zero outside the atom. Nevertheless, even in very inhomogeneous cases, the LSDA works remarkably well. The general features of the LDA is written as:

1. It favors more homogeneous systems.

2. It gives over–binding molecules and solids.

3. Chemical trends are usually correct.

4. For good systems (covalent, ionic, and metallic bonds): geometries are good, bond lengths, bond angles and phonon frequencies are within a few percent, while dielectric properties are overestimated by about a 10%.

5. In finite systems the XC potential does not decay as $-e^2/r$ in the vacuum region, thus affecting the dissociation limit and ionization energies. This is a consequence of the fact that both the LDA and LSDA fail at canceling the self interaction included in the Hartree term of the energy. This is one of the most severe limitations of these approximations.

The LDA is very successful approximation for many systems of interest, especially those where the electronic density is quite uniform such as bulk metals, but also for less uniform systems as semiconductors and ionic crystals. There are, however, a number of known features that the LDA fails to reproduce:

1. In atomic systems, where the density has large variations, and also the self–interaction is important.

2. In weak molecular bonds, e.g. hydrogen–bonds, because in the bonding

region the density is very small and the bonding is dominated by inhomogeneities.

3. In van der Waals –closed shell– systems, because in this case the binding is due to dynamical charge-charge correlations between two separated fragments, and this is an inherently non-local interaction.

4. In metallic surfaces, because the XC potential decays exponentially while it should follow a power law (image potential).

5. The energy band gap in semiconductors turns out to be very small. The reason is that when one electron is removed from the ground state, the exchange hole becomes screened, and this is absent in the LDA. On the other hand, also Hartree–Fock has the same limitation, but the band gap turns out to be too large.

2.7.2 Generalized Gradient Approximation (GGA)

The success of LSDA has led to the development of various generalized gradient approximations (GGA) [32] with marked improvement over LSDA over many cases. Widely used GGA's can now provide the accuracy required for density functional theory to be used in various type of analysis. The first step beyond local approximation is a functional of the magnitude of the gradient of the density (∇n) as well as the value n at each point. The low-order expansion of the exchange and correlation energies does not lead to consistent improvement over LSDA. The basic problem is that gradients in real materials are so large that the expansion breaks down. The term GGA denotes a variety of ways proposed for functions that modify the behavior at large gradients in such a way as to preserve desired properties. It is convenient to define the functional as a generalized form of Eq. 2.39

$$E_{xc}^{GGA}[n^{\uparrow}, n^{\downarrow}] = \int d^3r n(r)\varepsilon_{xc}^{hom}(n)F_{xc}(n^{\uparrow}(\mathbf{r}), n^{\downarrow}(\mathbf{r}), \nabla n^{\uparrow}(\mathbf{r}), \nabla n^{\downarrow}(\mathbf{r})), \qquad (2.40)$$

where F_{xc} is dimensionless and ε_x^{hom} is the exchange energy of the unpolarized gas. Numerous forms for F_{xc} have been proposed and they can be illustrated by three widely used forms of Becke(B88) [33], Perdew and Wang (PW91) [32], and Perdew, Burke, and Enzerhof (PBE) [34]. Typically, there are more rapidly varying density regions in atoms than in condensed matter, which leads to greater lowering of the exchange energy in atoms than in molecules and solids. The general trends of GGA's concerning improvements over the LDA are the following:

1. They improve binding energies and also atomic energies.

2. They improve bond lengths and angles.

3. They improve energetics, geometries and dynamical properties of water, ice and water clusters. BLYP and PBE show the best agreement with experiment. In general, they improve the description of hydrogen–bonded systems, although this is not very clear for the case of F–H bond.

4. Semiconductors are marginally better described within the LDA then in GGA, except for the binding energies.

5. For $4d$–$5d$ transition metals the improvement of the GGA over the LDA is not clear, and will depend on how well the LDA does in the particular case.

6. Lattice constants of noble metals (Ag, Au, Pt) are overestimated. The LDA values are very close the experiment, and thus any modification can only worsen them.

7. There is some improvement for the gap problem (and consequently for the dielectric constant), but it is not substantial because this feature is related to the description of the screening of the exchange hole when one electron is removed, and this feature is usually not fully taken into account by GGA.

2.8 Pseudopotentials

A plane–wave–basis formalism is one of the simplest and most natural formalism to implement for crystals. However, expanding the core wave functions or the core oscillatory region of the valence wave functions into plane waves is extremely inefficient and we need infinite number of them in principle. Therefore, in practice, plane–wave basis sets are always used in conjunction with the pseudopotential approximation. The physical reasoning behind the pseudopotential approximation is simple: since the core electron wave functions of an atom remain essentially unchanged when placed into different chemical environments and since that the core wave functions' only major contribution to chemical bonding is to enforce the valence wave functions orthogonality to the core states, the true atomic potential can be replaced by a pseudopotential that effectively reproduces the effects of the core electrons. With only this physical constraint, an infinite number of pseudopotentials can be generated. The combination of pseudopotentials and plane waves has become one of the most popular methods for electronic structure calculations.

It is well known that the most physical properties of solids are dependent on the valence electrons to a much greater than core electrons. The pseudopotential approximation exploits this by removing the core electrons, which are highly localized, and by replacing them and the strong ionic potential by a weaker pseudopotential that acts on a set of pseudo functions rather than the true valence wave functions. The valence wave function oscillate rapidly in the region occupied by the core electrons due to the strong ionic potential in this region. These oscillations maintain the orthogonality between the core wave functions and the valence wave functions due to exclusion principle. Since the kinetic energy of a state is proportional to second derivative of the wave function, the kinetic energy of the free electron state is increased in the vicinity of the core region. Most pseudopotentials are then constructed such that they satisfy four general conditions. The first is that the valence pseudowavefunctions generated from the pseudopotential should contain no nodes. This stems from the fact that we would like to construct smooth pseudo– wave–functions. Second, the normalized atomic radial

pseudo–wave–function (PP) with angular momentum l is equal to the normalized radial all–electron wave function (AE) beyond a chosen cutoff radius r_{cl}.

$$R_l^{cl}(r) = R_l^{AE}(r) \; for \; r_{cl} > r. \tag{2.41}$$

Third, the charge enclosed within r_{cl} for the two wave functions must be equal.

$$\int_0^{r_{cl}} |R_l^{PP}(r)|^2 r^2 dr = \int_0^{r_{cl}} |R_l^{AE}(r)|^2 r^2 dr. \tag{2.42}$$

Last, almost redundantly, the valence all–electron and pseudopotential eigenvalues must be equal,

$$\varepsilon_l^{PP} = \varepsilon_l^{AE}. \tag{2.43}$$

If a pseudopotential meets the conditions outlined above, it is commonly referred to as a norm–conserving pseudopotential. Pseudopotential is angular momentum dependent so each angular momentum component of the wave function see a different potential. So its scattering properties for the pseudo wave function are identical to scattering properties of the ion and the core electrons for the valence wave functions. An ionic potential, valence wave function and corresponding pseudopotential and pseudo wave function are illustrated in Figure 2.1.

2.8.1 Ultrasoft Pseudopotential

One goal of pseudopotentials is to create pseudofunctions that are as smooth as possible and accurate. One approach known as ultrasoft pseudopotentials reaches the goal of accurate calculations by a transformation that re-expresses the problem in terms of a smooth function and an auxiliary function around each ion core that represents the rapidly varying part of the density. The transformation proposed by Vanderbilt [35] rewrites the non-local potential in a form involving a smooth function $\widetilde{\phi}$=$r\widetilde{\Psi}$ that is not norm conserving, i.e. removing the condition

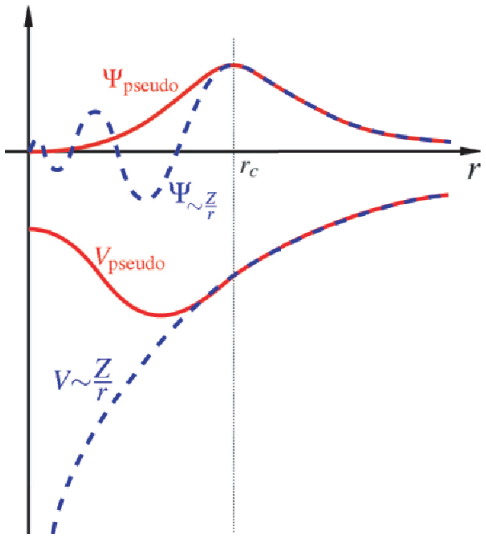

Figure 2.1: Comparison of a wavefunction in the Coulomb potential of the nucleus (dashed) to the one in the pseudopotential (solid). The real (dashed) and the pseudo wavefunction and potential (solid) match above a certain cutoff radius r_c.

of Eq. 2.42. For each reference atomic states smooth functions $\widetilde{\Psi}$ are solutions of generalized eigenvalue problem.

2.8.2 Projector Augmented Waves

The projector augmented wave (PAW) [36] method is a general approach to a solution of the electronic structure problem that reformulates the orthogonalized plane wave method (OPW), adapting it to modern techniques for calculation of total energy, forces, and stress. Like the ultrasoft pseudopotential method, it introduces projectors and auxiliary localized functions. The PAW approach also defines a functional for the total energy and it uses advances in algorithms for efficient solution of the generalized eigenvalue problem. However, the difference is that the PAW approach keeps the full all-electron wavefunction in a similar way to the general OPW expression so it recovers the wavefunction within the core region of atoms. Since the full wavefunction varies rapidly near the nucleus, all integrals are evaluated as a combination of integrals of smooth functions extending throughout space plus localized contributions evaluated by radial integration.

2.9 Periodic Supercells: the Bloch Theorem

By using the above presented formalisms observable of many-body systems can be transformed into single particle equivalents. However, there still remains two difficulties: A wave function must be calculated for each of the electrons in the system and the basis set required to expand each wave function is infinite since they extend over the entire solid. For periodic systems both problems can be handled by Bloch's theorem [37].

2.9.1 The Bloch's Theorem

According to the Bloch theorem, each electronic wave function of a periodic solid can be written in the following form :

$$\Psi_i(\mathbf{r}) = u_i(\mathbf{r})e^{i\mathbf{k}.\mathbf{r}}, \tag{2.44}$$

where u_i has the period of crystal lattice with $u_i(\mathbf{r}) = u_i(\mathbf{r} + \mathbf{T}_n)$ and $\mathbf{T}_n$ is the translation operator and eigenfunction of this operator vary from one unit cell to other in a periodic crystal with a phase factor given as: $T_n\Psi(\mathbf{r}) = \Psi(\mathbf{r} + \mathbf{T}_n) = e^{i\mathbf{k}\mathbf{T}_n}\Psi(\mathbf{r})$. u_i can be expanded using a basis set consisting of reciprocal lattice vectors of the crystal.

$$u_i(\mathbf{r}) = \sum_G a_{k,G}e^{i\mathbf{G}.\mathbf{r}}, \tag{2.45}$$

where $\mathbf{G}$ is the reciprocal lattice vector and defined as $\mathbf{G}.\boldsymbol{l} = 2\pi m$ for all l where l is a lattice of the crystal and m is the integer.

2.9.2 k–point Sampling

Electronic states are only allowed at a set of k–points determined by boundary conditions. The density of allowed k–points are proportional to the volume of the

cell. The occupied states at each k–point contribute to the electronic potential in the bulk solid, so that in principle, a finite number of calculations are needed to compute this potential. However, the electronic wave functions at k–points that are very close to each other, will be almost identical. Hence, a single k–point will be sufficient to represent the wave functions over a particular region of k–space. There are several methods which calculate the electronic states at special k–points in the Brillouin zone [38]. Using these methods one can obtain an accurate approximation for the electronic potential and total energy at a small number of k–points. The magnitude of any error can be reduced by using a denser set k–points.

2.9.3 Plane–wave Basis Sets

According to Bloch's theorem, the electronic wave functions at each k-point can be extended in terms of a discrete plane–wave basis set. Infinite number of plane waves are needed to perform such expansion. However, the coefficients for the plane waves with small kinetic energy $(\hbar^2/2m)|\mathbf{k}+\mathbf{G}|^2$ are more important than those with large kinetic energy. The truncation of the plane–wave basis set at a finite cutoff energy will lead to an error in computed energy. However, by increasing the cutoff energy the magnitude of the error can be systematically reduced.

2.9.4 Plane–wave Representation of Kohn–Sham Equations

When plane waves are used as a basis set, the Kohn–Sham (KS) [30] equations assume a particularly simple form. In this form, the kinetic energy is diagonal and potentials are described in terms of their Fourier transforms. Solution proceeds by diagonalization of the Hamiltonian matrix. The size of the matrix is determined by the choice of cutoff energy, i.e. the number of plane waves ($\mathbf{G}$ vectors), and will be very large for systems that contain both valence and core electrons.

This is a severe problem, but it can be overcome by considering pseudopotential approximation.

2.9.5 Non–periodic Systems

The Bloch theorem cannot be applied to a non–periodic systems, such as a system with a single defect or cluster. A continuous plane-wave basis set would be required to solve such systems. Calculations using plane-wave basis sets can only be performed on these systems if a periodic supercell is used. Periodic boundary conditions are applied to supercell so that the supercell is reproduced through out the space. As seen schematically in Figure 2.2 even molecules can be studied by constructing a large enough supercell which prevents interactions between molecules.

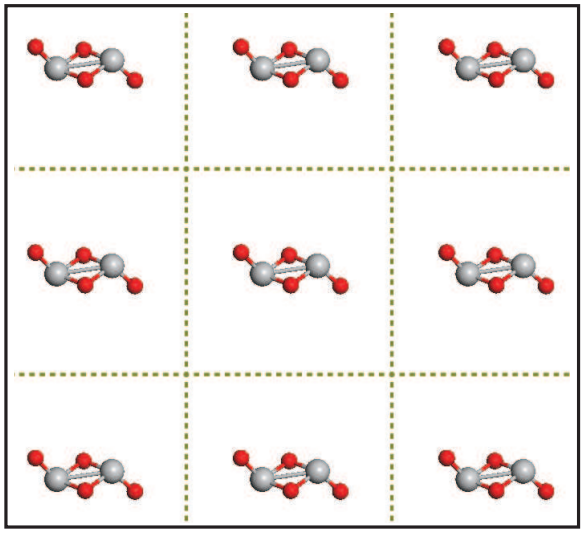

Figure 2.2: Schematic illustration of a supercell geometry of a molecule.

2.10 Numerical Calculations

We have used Vienna *Ab-initio* Simulation Package (VASP) in our numerical calculations[39]. VASP is a package for performing *ab initio* quantum mechanical molecular dynamics (MD) using either ultrasoft Vanderbilt pseudopotentials, or the Projector Augmented Wave Method, and a plane wave basis set. All calculations are performed within the Density Functional Theory formalism. The approach implemented in VASP is based on a finite–temperature local–density approximation and an exact evaluation of the instantaneous electronic ground state at each MD–step using efficient matrix diagonalization schemes and an efficient Pulay mixing. Forces and the full stress tensor can be calculated with VASP and used to relax atoms into their instantaneous ground-state.

We have performed calculation for several systems which require system specific parameters. Therefore, parameters used in calculations have been given in the beginning of the each chapter.

Chapter 3

SMALL TiO_2 CLUSTERS

Most of the applications of TiO_2 are mainly related to its optical properties such as photovoltaic and photocatalysis. As the size and dimensionality of TiO_2 materials decrease, we can enhance, for instance, the catalysis activity [40] of these materials. Therefore, low dimensional structures of TiO_2 nanoparticles and clusters are crucial to obtain efficient device applications. There are numerous experimental [41, 42, 43, 44, 45, 46, 47, 48, 49, 50] and theoretical studies on small neutral, negatively and positively charged TiO_2 clusters [51, 52, 53, 54, 55, 56, 57, 58, 59, 60, 61, 62, 63, 64] and nanoparticles [65, 66, 67]. Walsh *et al.* [53] have studied the structure, electron affinities and stability of TiO_n and $TiO_n{}^-$ clusters for $n = 1$–3 by using a density functional (DFT) based method. Stoichiometric and non-stoichiometric (O rich) small neutral and charge clusters have been investigated by Albaret [54, 55, 56]. Relative stability for the various isomers in terms of competition between ionic and covalent effects, derived from charge distribution, in Ti–O bond, electron affinities and optical excitation gaps have been calculated. Jeong *et al.* [57] have studied the energetics, equilibrium geometry, and harmonic vibrational frequencies of isolated Ti_mO_n clusters for m=1–6 and n=1–12 by using DFT based method. Hamad *et al.* [58] have searched a large number of cluster geometries making use of interatomic potential to find the global minima of small $(TiO_2)_n$ clusters and the most energetic structures have been reoptimized by using DFT/B3LYP

to obtain more accurate results. Structural, electronic, vibrational properties and stabilities of $(TiO_2)_n$ (n=1–8) clusters have been studied by employing DFT based methods [59]. Qu *et al.* [60, 61] have investigated the electronic structure and stability of both neutral and singly charged $(TiO_2)_n$ (n=1–9 and 10–16) clusters by using density functional B3LYP/LANL2DZ method. $(TiO_2)_n$ anatase like clusters with having n values between 16 and 32 have been constructed by introducing rigid criteria of stoichiometry, high coordination and balanced charge distribution by using B3LYP method [62]. Bardard *et al.* [64] have studied the electronic and structural properties of anatase TiO_2 nanoparticles through self consistent tight binding method and DFT.

Existence of H_2O molecules can influence the reactions in experiments and processes. There are several theoretical studies on interaction of water with nanoparticles which have different size and structure [68, 69, 70, 71]. Erdin *et al.* [70] have studied the interaction of water with rutile and anatase nanoparticles using tight binding molecular dynamics (MD). Nanoparticles expand in water due to interaction and water molecules dissociate on the nanoparticle surface. Koparde *et al.* [71] have also used MD to study the interaction of water with anatase and rutile particles ranging from 2.5 to 4 nm at room temperature and hydrothermal conditions.

In order to use TiO_2 clusters as a nanoscale material, it is mandatory to know their structural, electronic and magnetic properties. Because of their importance for fundamental science and practical applications, we have presented a systematic investigation of structural and electronic properties of $(TiO_2)_n$ clusters (n=1–10) within the density functional theory. Interaction of these clusters with molecular and atomic species like H_2O, Co, V, and Pt have also been studied. We have clarified how TiO_2 base materials behave in low dimensions.

3.1 Method

We have performed first-principles plane wave calculations [21, 39] within density functional theory (DFT) [30] using projected augmented-wave (PAW) potentials [36]. $3p^6 3d^3 4s^1$ for Ti and $2s^2 2p^4$ electronic configuration for O atom have been used in pseudopotentials. The exchange correlation potential has been approximated by Generalized Gradient Approximation (GGA) by using PW91 [32] formulation. All structures have been treated in a tetragonal supercell (with lattice parameters a_{sc}, b_{sc} and c_{sc}) using periodic boundary conditions. To prevent interaction between adjacent isolated clusters, a large spacing between the clusters (at least 10 Å) has been taken. In the self-consistent potential and total energy calculations, only Γ point has been used for $\boldsymbol{k}$-point. A plane-wave basis set with kinetic energy cutoff (E_{cut}) 500 eV has been used. All atomic positions have been optimized by using conjugate gradient method where total energy and atomic forces are minimized. The convergence criterion for energy and forces have been chosen as 10^{-5} eV between two ionic steps, and the maximum force allowed on each atoms is 0.03 eV/Å.

3.2 Results and Discussions

As a first step, we have studied TiO and TiO_2 clusters. TiO molecule prefers the magnetic ground state with magnetic moment of $\mu = 2\mu_B$ and Ti–O bond length is 1.63 Å in good agreement with experiment [72]. Bent TiO_2 molecule is about 2 eV energetically more stable than the linear one and both structures prefer the singlet state. Ti–O bond length and O–Ti–O bond angle are 1.66 Å and 109°, respectively. Experimentally, estimated value of O–Ti–O angle is 110±5 [41]. In linear Ti_2O_2 molecule, Ti–O–O–Ti structure is unstable. Molecule breaks from O–O bond and two separated weakly interacting Ti–O molecules upon relaxation of linear Ti–O–O–Ti molecule is obtained. We can propose formation mechanism for bent TiO_2 in terms of a single Ti atom and O_2 molecule.

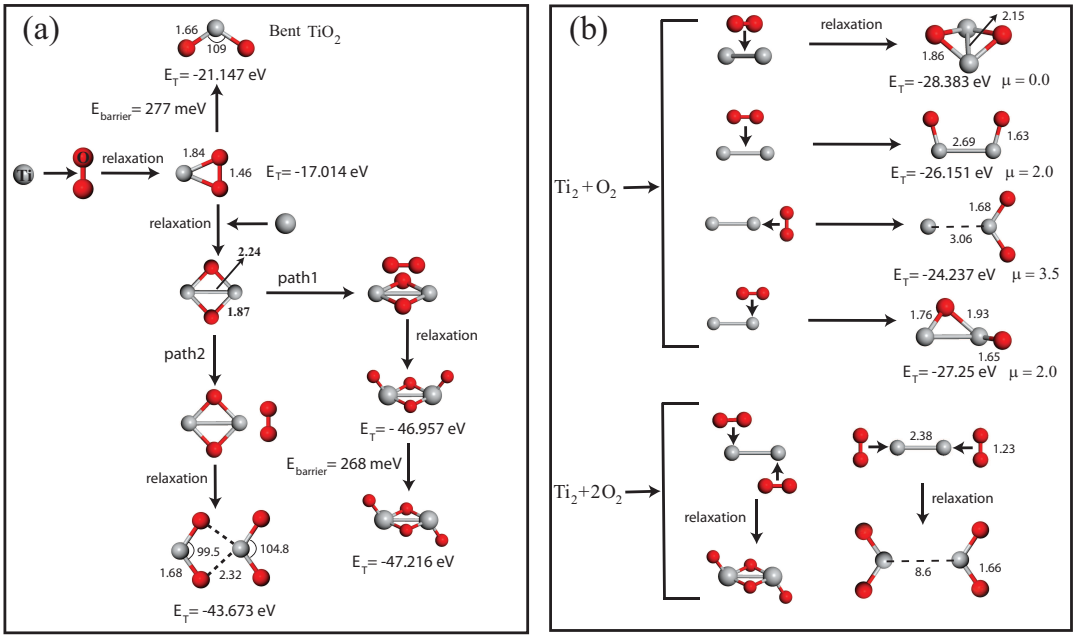

Figure 3.1: Growth mechanism of some small TiO and TiO_2 molecules: (a) in terms of Ti atom and O_2 molecule and (b) Ti and O dimers. Bond lengths and magnetic moments are given in Å and μ_B, respectively.

As a result of the interaction between Ti atom and O_2 molecule, we have initially obtained a metastable structure in which O–Ti–O bond angle, Ti–O and O–O interatomic distances are 46.9°, 1.84 and 1.46 Å, respectively. Energy barrier between this metastable and bent structures is 277 meV. Figure 3.1 represents the formation path of some small TiO and TiO_2 clusters. When an extra Ti atom is sent to this metastable TiO_2 molecule, O–O bond is broken completely and resulting Ti_2O_2 molecule has singlet ground state. In addition to construction of small stoichiometric (TiO_2) and non-stoichiometric (TiO) clusters in terms of Ti atom and O_2 molecule, formation of these clusters have been also considered in terms of Ti and O dimers as shown in Figure 3.1 (b). In general, magnetic clusters have been obtained upon the interaction between single Ti_2 and O_2 dimers. All these non-stoichiometric magnetic clusters have at least one 1–fold coordinated O atom. However, the ground state structure of product of Ti_2 + O_2 reaction is paramagnetic and has no dangling O atom. In contrast to Ti + O_2 interaction, O_2 molecule dissociates during the interaction with Ti_2 molecule. There is no energy barrier for this dissociation. As a result of breaking of O–O bond (which

occur in all possible interaction structure between Ti and O dimers) and Ti–Ti bond (which is observed only in one interaction case), it can be argued that Ti–O bond is more stronger than both O–O and Ti–Ti bonds. In the case of $Ti_2 + 2O_2$ interaction, bent TiO_2 and ground state structure of Ti_2O_4 cluster can be directly obtained upon the reaction among one Ti and two O dimers without supplying any additional energy to overcome any barrier. It is easy to find global minimum structures of stoichiometric small Ti_nO_{2n} clusters for $n < 4$ clusters (where n is the number of Ti atoms in cluster) and our findings are consistent with previous experimental and theoretical works.

In construction of cluster geometries, we have considered some criteria in order to obtain stable clusters: we have avoided O–O bonds, undercoordinated Ti atoms (each Ti atom bind to at least four O atoms) in large clusters ($n > 4$) and more than two pendant O atoms. In this last criterion, O atom binds only to a single Ti atom and bond length occurs around 1.64 Å, which is at least 0.2 Å shorter than Ti–O bond length for a more coordinated O atom. To find the lowest structure, we have searched a large number of cluster geometries for each n (=1–10). For the bonding analysis, Ti–O and Ti–Ti bonds exist if Ti–O and Ti–Ti interatomic distances are smaller than 2.13 and 2.94 Å, respectively. For the bulk anatase and rutile phases of TiO_2, Ti–O bond lengths range from 1.95 to 2.01 Å. Coordination number is the important analysis tool for the investigation of the stability of the small titania clusters. It is defined as the total number of nearest neighbors of one Ti or O atom.

3.2.1 Clusters n=1–5

Energetics and stability of the lowest lying structures for each n have been compared with their isomers. Figure 3.2 shows the optimized structure of the five lowest lying isomers for n=1–5 $(TiO_2)_n$ clusters. For $(TiO_2)_2$ clusters, 2a is 0.26 eV more energetic than its cis isomer (2b). In 2c cluster, one pendant O atom exists and one of the Ti atoms binds to three O atoms. Due to cage structure and

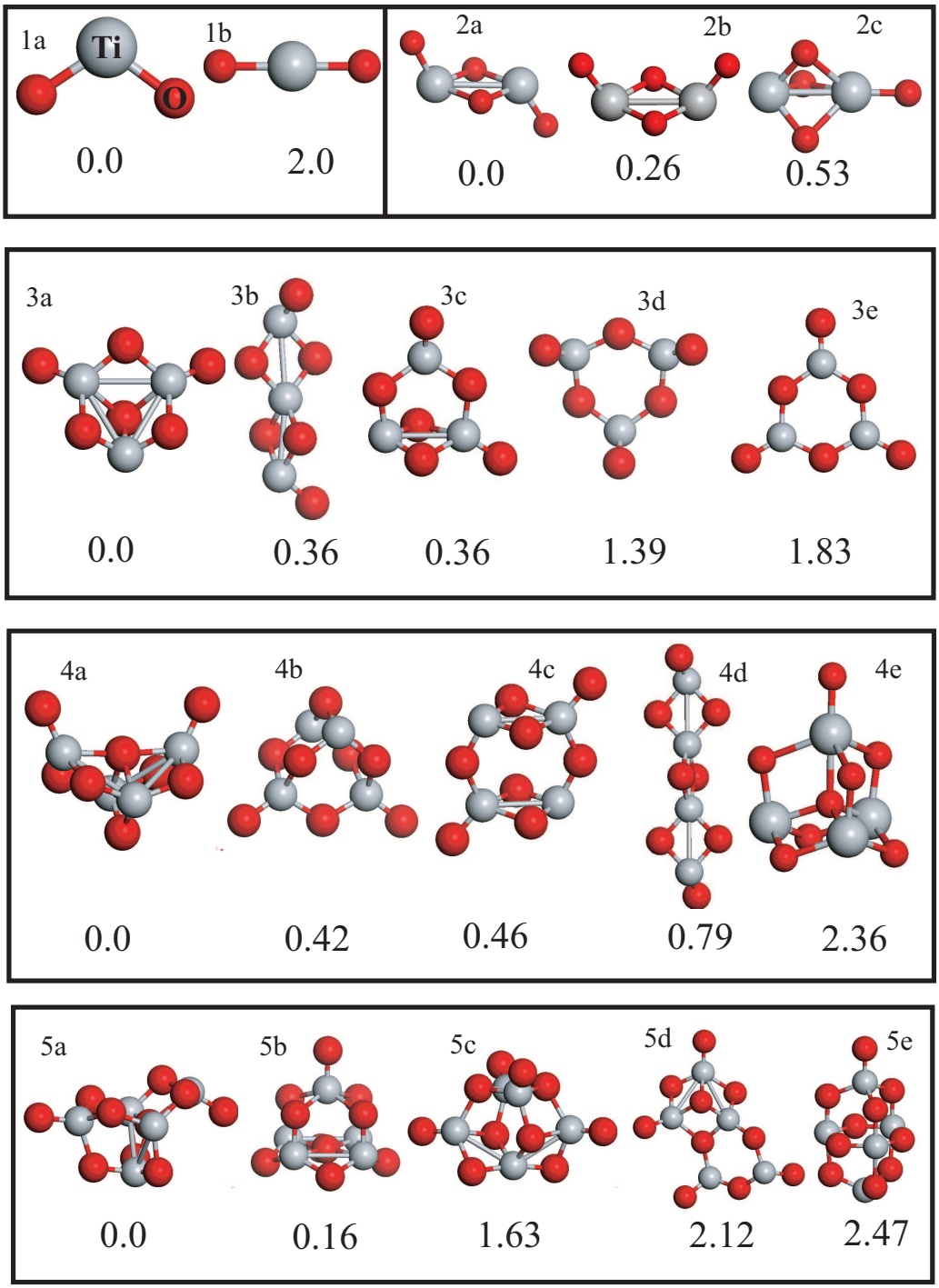

Figure 3.2: Fully optimized structure of the five lowest lying isomers of the neutral $(TiO_2)_n$ clusters for n=1–5. Ti and O atoms are demonstrated by gray and red spheres, respectively. The energies (in eV) relative to the corresponding ground state geometries are also given.

more repulsive interaction among these three O atoms, this structure is 0.56 eV higher in energy than the 2a structure. In n=3 case, global minimum has 3–fold coordinated O atom and two pendant O atoms. 3b and 3c isomers are very close to each other in energy. They could be simultaneously found in a TiO_2 cluster mixture. Actually, in finite temperature experiments, more than one isomer of any $(TiO_2)_n$ may exist if energy difference is small among these isomers. Free energy is the most important quantity in determining of the lowest lying structure at finite temperatures. In contrast to our results, Qu [60] have found that 3c structure is 0.24 eV more energetic than 3b. 2a and 3b structures are related to each other. We can form infinite wire structure by repeatedly adding TiO_2 bent molecule to 2a. In each adding process, total energy per TiO_2 units (E_T/m) increases and saturates after very large m. Here, m represents the number of the added bent TiO_2 molecule. This energy is 23.61, 24.31 and 24.68 eV for 2a, 3b and 4d, respectively and becomes 25.78 eV for the infinite chain which is at equilibrium. We have also considered the planar clusters. These two–dimensional (2D) structures do not obey our cluster construction criteria. 3e planar structure is 1.83 eV higher in energy than 3a. In planar clusters, number of pendant O atoms is equal to n. Energy difference between the lowest lying structure of a certain cluster (E_{na}) and its planar isomer (E_{planar}) decreases with decreasing n. For instance, E_{na}-E_{planar} is equal to 1.83, 2.82, 5.46 and 8.25 eV for n= 3, 4, 5 and 6, respectively. However, the situation is different when we compare the planar clusters with each other. E_T/n increases with increasing n. The rate of increase slows down when we reach n=6. E_T/n is 23.82 (n=3), 23.98 (4), 24.035 (5) and 24.066 eV (6). Three dimensional clusters are more stable relative to two dimensional counterparts. For $(TiO_2)_4$ clusters, 4c structure can be obtained from top–to–top interaction of two 2a structures. We can also form the infinite wire by repeatedly adding more 2a to 4c and resulted infinite structure has lower binding energy E_b compared to the finite 2a or 4c clusters. Global minimum 4a has a 4–fold coordinated O atom. In a covalent compound, coordination of O atom does not exceed three. As a result of this argument, 4a cluster shows mainly ionic character. In the study of Qu *et al.*, 4b structure is the global minimum. They have found that energy difference between 4b and 4c is 0.29 eV. In n=5 clusters, Both 5a and 5b structures have 4–fold coordinated O atom. 5a structure

is 0.16 eV more energetic than 5b. Number of pendant O atom is two and one in 5a and 5b, respectively. We have tested the formation of 2a, 3a and 4a from 1a. If two 1a interact in a suitable configuration, we can obtain 2a. Similarly, 3a or 4a can be formed by adding extra 1a to 2a or 3a. In this way, bigger clusters can be formed by using only 1a and it becomes a building block of the larger systems.

3.2.2 Clusters n=6–10

Figure 3.3 represents the optimized structure of the n=6–10 clusters. 6a structure has a 4–fold coordinated O atom which locates at the center of the cage of 6a. The bond length between this O and each nearest Ti atom is around 2.03 Å. 6b and 6c structures have also 4–fold coordinated O atom. Our lowest lying structure 6a is different from those of Ref. [60, 58, 59]. In n=7 case, 7a is not the global minima of Ref. [60]. 7a geometry is 0.49 eV more stable than 7b. All lowest lying isomers have at least one pendant O atom. There are two 3–fold coordinated O atoms in 7a. We have found a new structure for the ground state of n=8 clusters. 8a has cubic–like structure. Two pendant O atoms bind to opposite Ti atoms in opposite corners. 8b and 8c are the global minima of Ref. [60] and [58], respectively. 8d and 9d structures have been taken from anatase crystal. Their energies are around 2.3 eV higher than 8a and 9a. Therefore, ground state structures of the small TiO_2 clusters cannot be derived from bulk phases. Unlike $n \leq 8$ clusters, ground state structure of n=9 has only one pendant O atom and is 1.74 eV more stable than 9c having two pendant O atoms. 9a and 9b have one and two 3–fold coordinated O atoms and this implies that bonds in these clusters exhibit also covalent character. 10a is the only cluster possessing no pendant O atoms. In structure of 10a, there are four 4–fold coordinated O atoms and all Ti atoms have 4–fold coordination. Interestingly, the second lowest lying structure 10b has also no pendant O atoms. 10a is 0.93 eV more stable than the global minima of Ref. [61]. In general, ground state structures in each n have at least one pendant O atom.

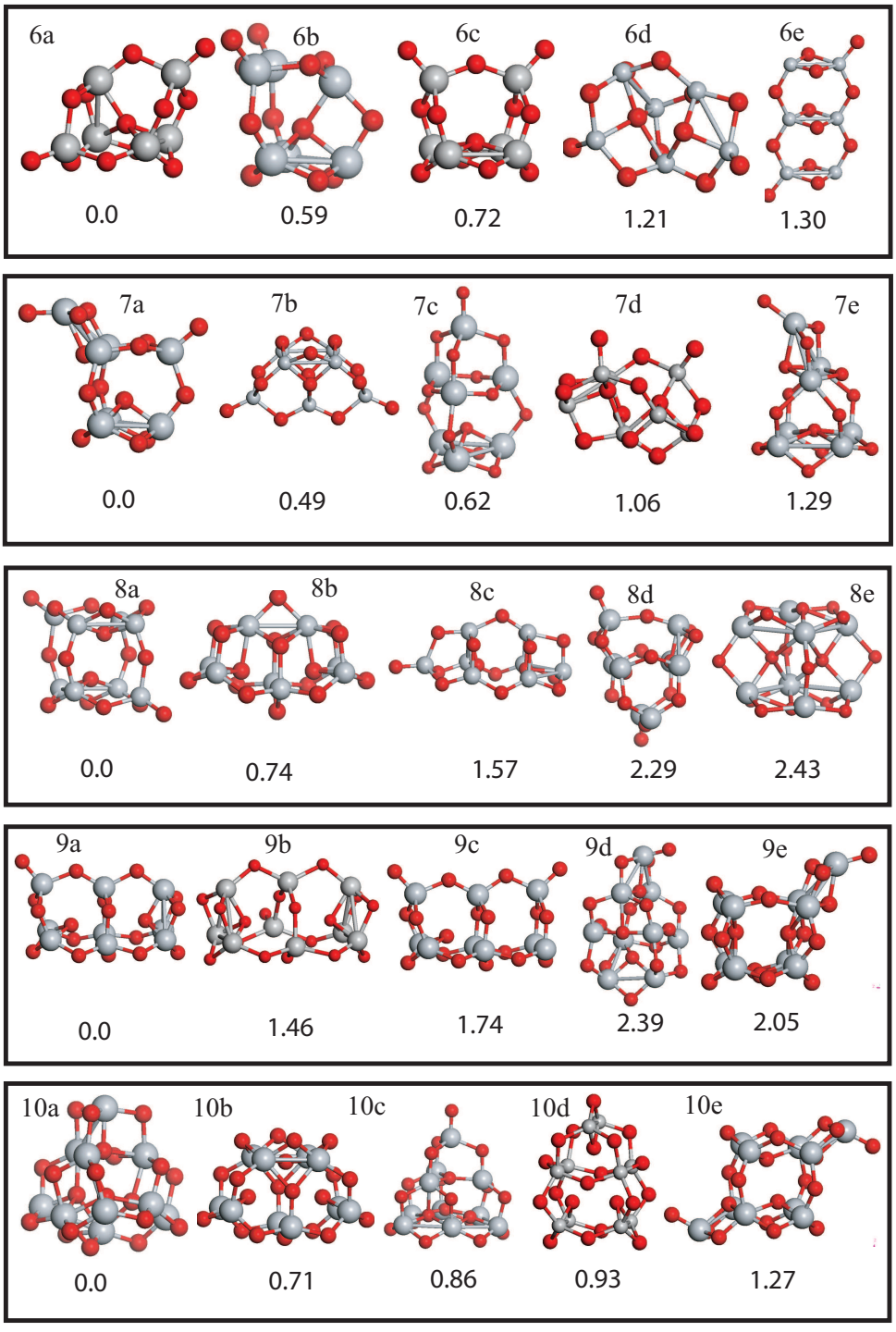

Figure 3.3: Fully optimized structure of the five lowest lying isomers of the neutral $(TiO_2)_n$ clusters for n=6–10. Ti and O atoms are demonstrated by gray and red spheres, respectively. The energies (in eV) relative to the corresponding ground state geometries are also given.

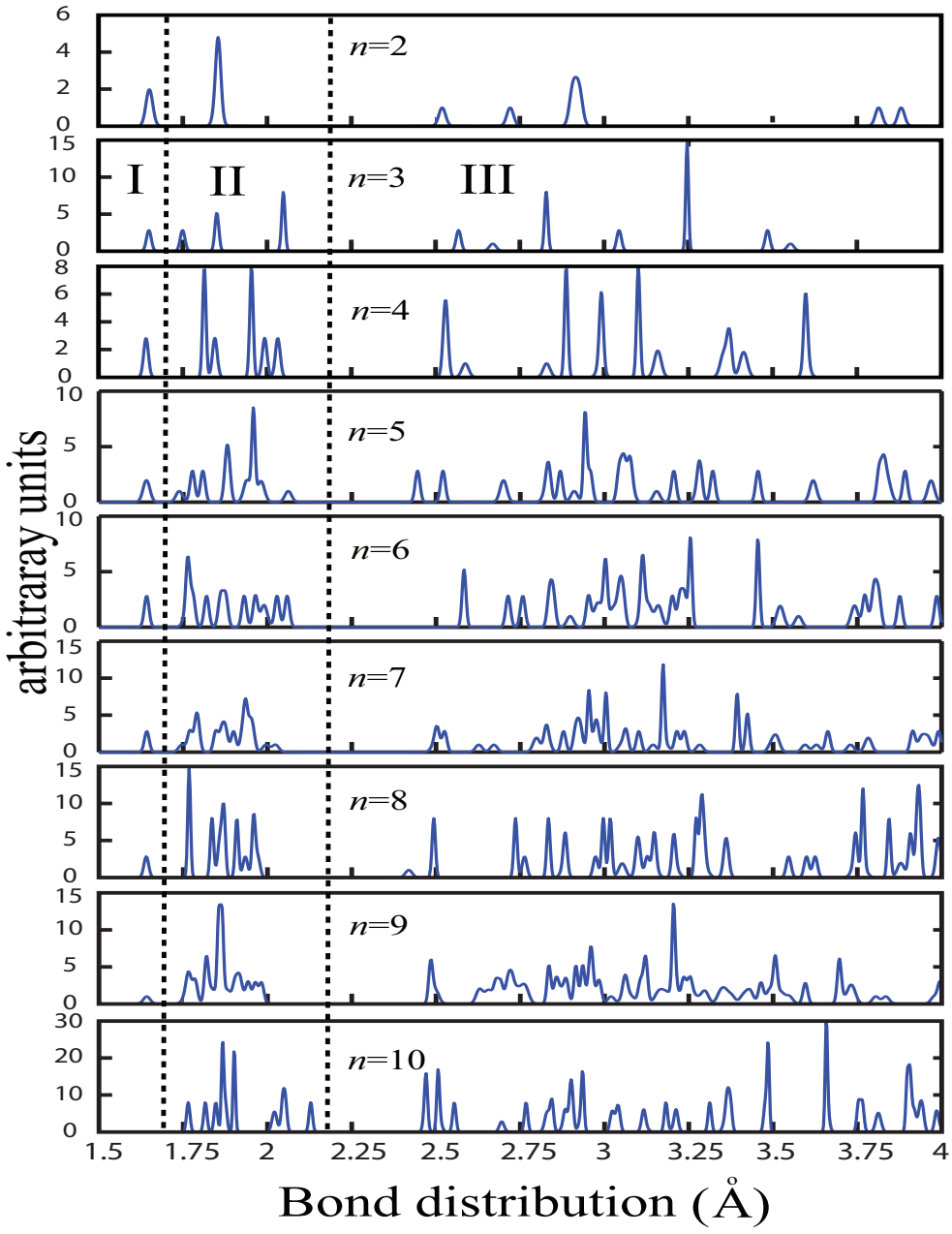

Figure 3.4: Gaussian smeared distribution of Ti–O, O–O and Ti–Ti interatomic distances for ground state geometries for n=2–10 clusters. Two dashed lines divide the graphs into three regions. In region I, bond distance distribution between pendant O and its nearest Ti atom; in region II, distribution of the bonds between highly coordinated (at least two) O atoms and their first nearest neighbor Ti atoms; in region III, second, third, fourth etc. nearest neighbor interatomic distances in Ti–O and O–O atom pairs. This region also includes the first and high order nearest neighbor distances between Ti atoms (Ti–Ti interatomic distance).

Figure 3.4 shows the distribution of Ti–O, O–O and Ti–Ti interatomic distances for n=2–10. We have taken each atom as the center of a 4 Å radius circle and we have measured all interatomic distances between the central atom and other atoms which are inside the circle. This procedure has been performed for all atoms in the cluster. Height of the peaks is proportional to the occurrence of a certain interatomic distance. We have divided each graph into three regions. First region presents the interatomic distance between pendant O atom and its nearest Ti atom. It is seen that this bond distance appears as a very clear and distinct peak for n=1–9 clusters and these peaks occur around 1.64 Å. For the n=10 cluster, there is no peak in the first region. In the second region, there are several peaks corresponding to the interatomic distance between multi-coordinated (at least two) O atoms and their first nearest neighbor Ti atoms. We can also divide this region into three parts. 2–fold coordinated O atoms are located near the first region. In the middle of the second region, both 2– and 3–fold coordinated O atoms exist. In 3a, 4^{th} peak is related with both 2– and 3–fold coordinated O atoms. Finally, 4–fold coordinated O atoms are close to the third region. Because of low symmetry of clusters, boundaries between these three parts are not strict. We have a strong peak around 2.1 Å for 4–fold coordinated O atoms in 10a. 2^{nd} peak in n=2 case exists in all n. In the third region, we have all other interatomic bond distances related with second, third, fourth, etc. nearest neighbors. For the small and relatively symmetric clusters such as 3a and 10a, almost all the peaks are very clear and distinguishable. In addition to Ti–O bonds, Ti–Ti bond lengths range from 2.72 to 2.94 Å and they are represented in the third region of Figure 3.4. Coordination number of Ti atoms influence the Ti–Ti bond length. In 2a structure, Ti–Ti interatomic bond distance is 2.72 Å. In this structure, Ti atoms bind to three O atoms. Ti–Ti bond length increases as the coordination number of these Ti atoms increases.

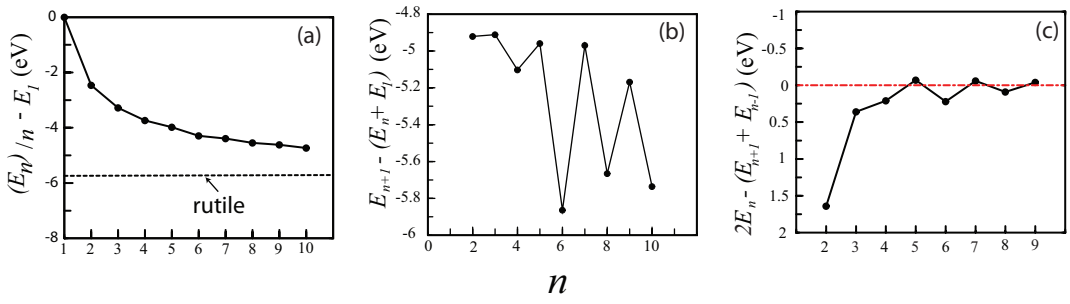

Figure 3.5: Formation energy (a) and nucleation energy (b) for the ground state geometries. Second order difference ($\Delta^2 E$) in E_b versus size of the cluster n is given in (c).

3.2.3 Stability of the clusters

Figure 3.5 presents the energetics and formation of TiO_2 clusters as a function of the number of TiO_2 units or n. We have used the same definitions for formation energy (E_n/n-E_1) and nucleation energy (E_{n+1}-(E_n-E_1)) of Ref. [59]. In Figure 3.5(a), it is noticed that all clusters ($n > 1$) are stable with respect to a single TiO_2 unit. In the same figure, we have also calculated the formation energy of rutile. It is seen that the formation energy approaches that of the bulk phase as the cluster size increases. There is a $1/n$ relation between the size of the clusters and formation energy. We have observed small oscillations after n=5. In Figure 3.1, we have shown the growth mechanism of some small clusters. Bigger clusters can be produced from the smallest cluster (n=1). In Figure 3.5(b), formation of larger clusters from bent TiO_2 molecule or cluster is shown. It is noticed that there are oscillations between odd and even n. It is easy to produce even n clusters from odd ones. Reaction is faster for even n. For producing odd n clusters from even n, reaction slows down. In a mixture of clusters having different size, n=6 would be the most abundant one. These results are in contradiction with those of Ref. [59]. In their study, odd clusters are easy to form and abundance is the highest in n=5 and n=7. Oscillations in Figure 3.5(a) and (b) show the same trend. The second difference in binding energy is shown in Figure 3.5(c) and has been also calculated as $\Delta^2 E = 2E_n$-E_{n+1}-E_{n-1}. Stability of a particular cluster (n) may be compared with its neighbors ($n+1$ and $n-1$). Positive (negative) $\Delta^2 E$ means unstable (stable) cluster with respect to its neighbors. Unlike the

large oscillations seen in Figure 3.5(b), we have observed not only small but also decaying oscillations around zero value with increasing n. As it is expected that $\Delta^2 E$ is negative for even n clusters.

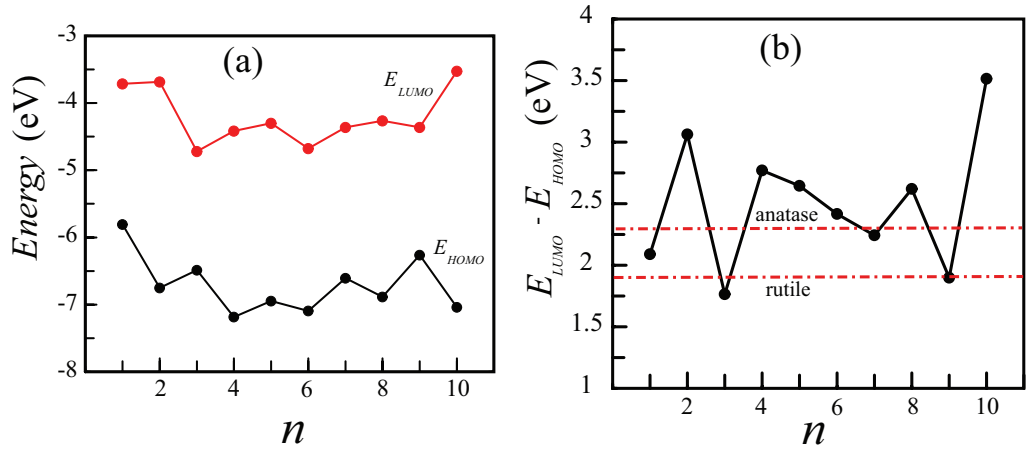

Figure 3.6: (a) Energy of the highest occupied (E_{HOMO}) and the lowest unoccupied (E_{LUMO}) energy levels, (b) energy differences between these levels E_{LUMO}-E_{HOMO}. Energy gaps of rutile and anatase are also shown for comparison.

3.2.4 Electronic properties of the free clusters

To study the electronic properties, we have calculated the HOMO–LUMO gap of the lowest lying structure of all clusters. Figure 3.6 shows the energy of HOMO and LUMO levels and their differences. In nanosize particles, quantum confinement effects begin to be crucial. As a result of these effects, HOMO–LUMO gap must decrease as the cluster size grows. It is noticed that there is no regular trend in the relation between HOMO–LUMO gap and n (or size of the cluster). Therefore, it is impossible to relate these structures with bulk rutile, anatase or other bulk phases of TiO_2. The structure of the clusters has significant effects on the HOMO–LUMO gap. In an experimental work, it has been pointed out that no quantum confinement effect has been observed for TiO_2 nanoparticles down to 1 nm [73]. In the study of Zhai *et al.* [50], band gap of a single negatively charged cluster approaches the bulk band gap limit when n=6 and remains

constant for n=6–10. It is known that DFT fails to calculate the correct energy gap (E_g). Our calculated E_g values are 1.90 (3.03) eV for rutile and 2.30 (3.2) eV for anatase. The numbers depicted in parenthesis are the experimental band gap values. Calculated E_g of n=3 cluster is smaller than both E_g of anatase and rutile. This result is inconsistent with the quantum size argument in which the band gap of small molecules must be larger than that of bulk.

3.2.5 Water adsorption

To understand the formation of TiO_2 nanoparticles produced under wet process or dissociation of H_2O on TiO_2 surfaces, it is important to figure out the interaction between H_2O molecule and 1D, 2D or 3D TiO_2 structures. Moreover, water always exists in experiments in liquid or gas phase. In this study, we have also investigated the interaction of the ground state structure of clusters with a single H_2O molecule for all n.

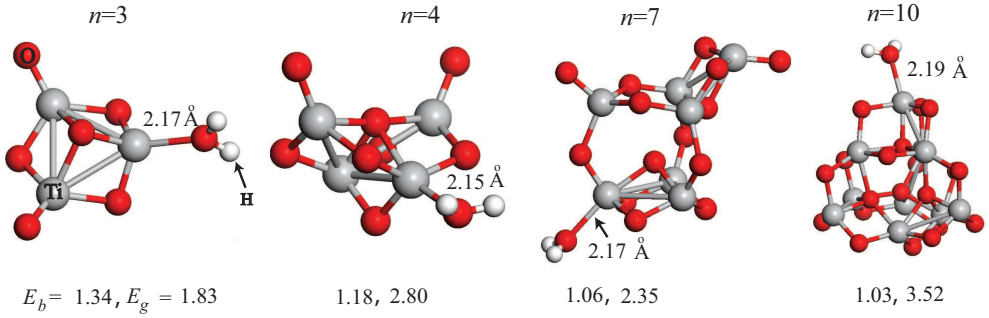

Figure 3.7: Optimized structure of H_2O+$(TiO_2)_n$ system for the most favorable adsorption case of selected clusters. Binding energy E_b of H_2 molecule on cluster (first number) and HOMO-LUMO gap E_g (second number) are given for each cluster in eV.

Figure 3.7 represents the optimized structure of the most energetic adsorption site for some selected clusters. It is noticed that in all cases, H_2O molecule binds to Ti atom of the cluster through its O atom. Interatomic distance between this Ti and O atoms is around 2.17±0.02 Å. In Figure 3.7, E_b and HOMO-LUMO gap

are also given. We have defined the E_b in terms of total energy of $(TiO_2)_n$+H_2O complex, isolated cluster and H_2O in the following form: E_b=E_T[$(TiO_2)_n$+H_2O]-(E_T[$(TiO_2)_n$]+E_T[H_2O]). Figure 3.8 represents variation of E_b with n.

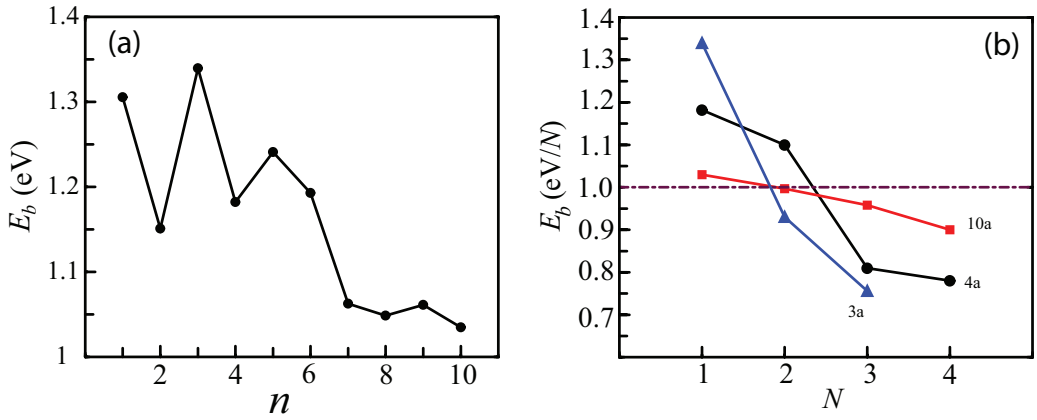

Figure 3.8: (a) Binding energy E_b of a single H_2O molecule on $(TiO_2)_n$ cluster as a function of n. (b) Variation of E_b of H_2O with the number of adsorbed H_2O molecules (N) for the 3a, 4a and 10a structures.

It is noticed that E_b oscillates as a function of n. For the n=1–6 clusters, this oscillation is more rapid than observed in n=7–10 clusters. Therefore, we have two different binding regions. After n=6, there is a sharp drop in E_b. Even–odd oscillations are observed in both regions. E_b takes the values ranging from 1.35 to 1.03 eV. Interaction is more strong for the n=1–6 clusters.

Figure 3.8(b) shows the variation of E_b of H_2O molecules with the number of adsorbed molecules (N). It is found that E_b per H_2O decreases as N increases. Relation between E_b and the number of adsorbed water molecules in 10a case is almost linear. E_b for one molecule is 1.03 eV and it drops to 0.90 eV per molecule for the four H_2O case in this cluster. Interatomic bond distance between O atom of the molecule and its neighboring cluster Ti atom increases slightly and becomes 2.20±0.02 Å for the four molecules case. For the 3a and 4a cases, E_b/N drops more rapidly compared to 10a cluster. It is noticed that there is a crossover between E_b/N of 10a and 3a (and also 4a). After N=1 for 3a and N=2 for 4a ,

water molecules bind to 10a cluster more strongly than the smaller clusters. In 3a and 4a clusters, the bound water molecules are very close to each other compared to those in 10a. Each adsorbed H_2O causes to more weakening of the interaction between these smaller clusters and the next adsorbed molecule than in 10a.

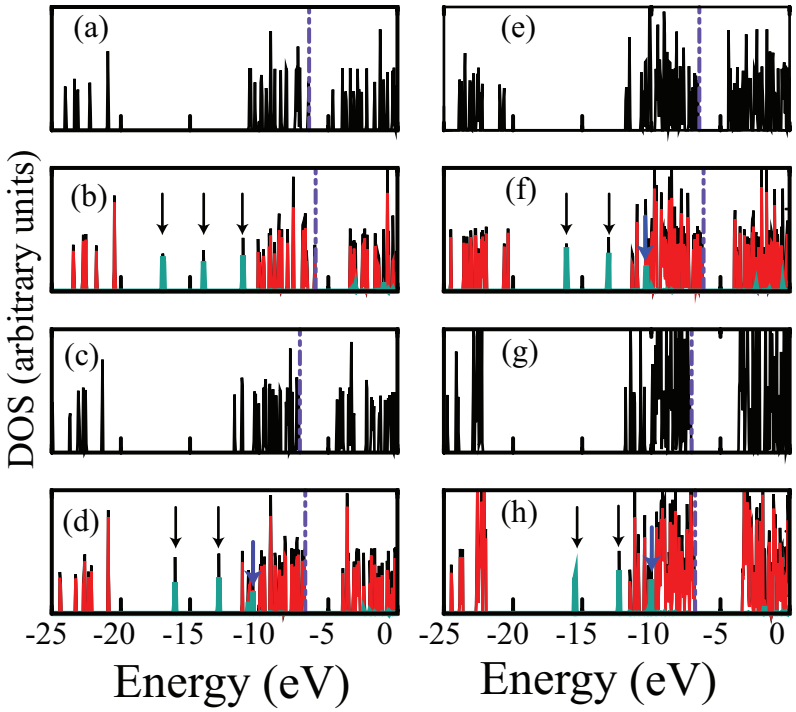

Figure 3.9: Electronic levels of $(TiO_2)_n$ clusters before ((a), (c), (e) and (g)) and after ((b), (d), (f) and (h)) the interaction with H_2O for n=3, 4, 7 and 10, respectively. The arrows show the position of H_2O levels after the interaction between H_2O molecule and the clusters. Fermi level is shown by the violet dot–dashed line. For the cluster+H_2O system after the interaction, black and red colors represent the total and cluster energy levels, respectively.

Figure 3.9 presents the orbital energy levels of the clusters of n=3, 4, 7, and 10 before and after interaction with H_2O. Due to interaction, energy levels of the clusters shift upwards. The amount of shift in each level (ΔE) decreases as cluster size grows and there is a direct correlation between E_b and ΔE. Weak interaction means small ΔE. The number of the possible adsorption sites for a molecule or an atom on clusters or nanoparticles increases as the surface area grows. 10a

structure is the biggest cluster and has four possible Ti sites that bind H_2O more strongly. Moreover, these Ti atoms have almost the same bonding environment. For this reason, we have examined the adsorption of more than one H_2O molecule by 10a, as well as 3a and 4a structures to make a comparison between the clusters of different sizes.

3.2.6 Transition metal adsorption

Ferromagnetic semiconductors are potential materials for spintronic applications. Transition metal (TM) doped TiO_2 has received considerable attention in the last several years to obtain ferromagnetism and efficient injection of spin-polarized carriers for semiconductor spintronic devices [74, 75, 76, 77, 78, 79, 80, 81, 82, 83]. Adsorption of TM atoms like Co, V, and Pt on $(TiO_2)_{10}$ have been investigated for possible functionalization of these clusters. We have considered several different possible adsorption configuration to find the most energetic adsorption site.

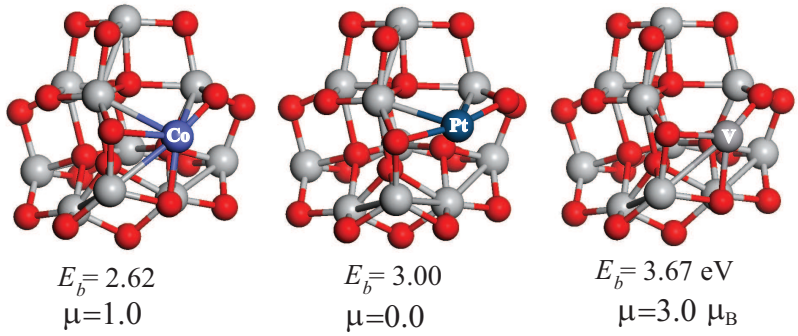

Figure 3.10: Most energetic adsorption site of Co, Pt and V atoms on n=10 cluster. Corresponding binding energy E_b and induced magnetic moment μ are also given.

In Figure 3.10, we have shown the most favorable adsorption site for each TM atoms. E_b of the adsorbate atom has been calculated using the same formula for the adsorption of H_2O molecule. Adsorbates prefer sites where they bind to more cluster atoms. The cluster has magnetic ground state with μ =1.0 and 3.0

μ_B for Co and V adsorption, respectively. Adatoms are also strongly bound to the cluster. E_b is 3.67, 2.63 and 3.0 eV for V, Co, and Pt atoms, respectively. In Figure 3.11, we have shown the electronic density of states of TM + cluster system after the interaction. It is noticed that there is a spin polarization for V and Co cases. Energy levels of TM atoms appear in the gap region of the cluster. Unlike Pt doping, there is a small but noticeable gap narrowing in V and Co cases.

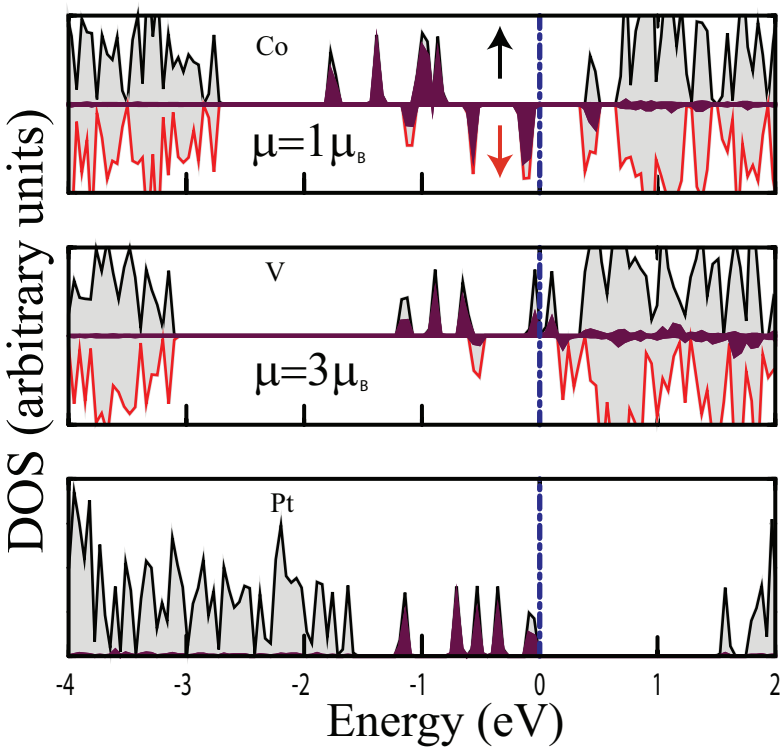

Figure 3.11: Gaussian smeared density of states (DOS) of TM–$(TiO_2)_{10}$ for the most stable adsorption site. Fermi level shown by the dotted–dashed blue line marks the zero of energy. DOS of TM atoms are shown in violet. Gray color denotes the total DOS.

Some energy levels of these adsorbed atoms are close to CB edge of the cluster. *d* states of Ti and dopant atoms mix at the bottom of the CB. However, main effect on electronic properties of TM doped clusters results from gap localized dopant energy levels. It is seen that we have a large red shift in all dopant cases as a

result of the band gap localized states mainly resulting from TM atoms. Optical transitions are from these gap localized impurity levels to CB. The electrons coming from the V and Co atoms are somehow delocalized in conduction band region and contribute to the formation of CB. E_g is 0.48, 0.14 and 1.65 eV for Co, V, and Pt, respectively. In pure cluster, E_g is 3.51 eV. In Co case, HOMO level mainly consists of d_{x^2}, d_{z^2} and d_{yz} orbitals of the Co atom. For the spin down component of LUMO, we have both contribution from d_{xy} orbital of Co and d orbital of Ti atoms. For V case, HOMO and LUMO levels are close to each other. Spin polarization of both levels are the same. All d components of V contribute in different amount to the HOMO orbital. LUMO consists of d_{x^2}, d_{z^2} and d_{yz} orbitals. Pt adsorbed cluster has a paramagnetic ground state. Unlike Co and V cases, d states of Pt atom are close to HOMO level of the cluster. Energy levels coming from Co atoms are more spread in the gap region of the cluster with respect to V or Pt atoms.

Chapter 4

THIN TiO_2 NANOWIRES

4.1 Introduction

Recently, one dimensional TiO_x nanostructures [3] such as nanorods, nanowires, and nanotubes have been investigated extensively because of their size and morphology dependent structural, chemical and electronic properties. They lead a significant number of technological applications including gas and humidity sensors [84], dye-sensitized solar cells [85, 86], photovoltaics, and photocatalysis [87].

TiO_2 nanowires [88, 89, 90, 91, 92] can be synthesized on TiO_2 surfaces or in zeolites. Blanco–Rey *et al.* [88] have obtained nonstoichiometric Ti_2O_3 quasi–1D metallic chains along the [001] direction of (1×2) reconstructed rutile surface. Naturally, semiconductor monatomic titania (...Ti–O–Ti–O...) chains is formed in Engelhard titanosilicate–4 (ETS–4) [89] and 10 (ETS–10) [90]. Individual chains are isolated from each other by an insulating silicate layer. Electrical transport measurement has been made for ETS–4 and a non-ohmic behavior has been observed. Conductivity of these monatomic chains increases with increasing bias voltages. Structural, electronic and vibrational properties of titania chains embedded in ETS–10 have been studied using *ab-initio* methods [93]. Moreover, Enyashin *et al.* [94, 95] have studied the stability and electronic structure of various TiO_2 nanotubes governed from anatase and lepidocricite layer modifications

by using density functional based tight binding method.

Therefore, a thorough analysis of the structural and electronic properties of stoichiometric and non-stoichiometric titania nanowires is necessary before one aims at its possible applications. Our motivation in this work is how thin TiO_x and rutile (110) nanowires are formed and behave in one dimension (1D). This work presents a systematical investigation of structural, electronic and magnetic properties of these nanowires within the density functional theory (DFT).

4.2 Computational methods

Total energy and electronic structure calculations have been performed by first principles plane wave method [21, 39] based on DFT [30] using both ultra-soft [35] and projected augmented-wave (PAW) [36] pseudopotentials with electronic configurations $3p^6 3d^3 4s^1$ for Ti atoms and $2s^2 2p^4$ for O atoms. The exchange–correlation potential has been treated by generalized gradient approximation (GGA) [32]. All structures have been represented in a tetragonal supercell geometry (with lattice parameters $a_{sc} = b_{sc}$ and c_{sc}) using periodic boundary conditions. To prevent interaction between adjacent isolated wires, a large spacing ($a_{sc} = b_{sc}$ ∼16 Å) has been introduced. For single cell wire calculations, c_{sc} corresponds to lattice constant c and for double cell calculations $c_{sc} = 2c$ (c being the lattice parameter of the TiO_x wires along the wire axis). Convergence with respect to the number of plane waves used in expanding Bloch functions and **k**-points in sampling the Brillouin zone have been tested for each wire systems. A plane-wave basis set with kinetic energy cutoff $\hbar^2|\mathbf{k} + \mathbf{G}|^2/2m \leq 450$ eV has been used. In the self-consistent potential and total energy calculations, Brillouin zone of nanowires has been sampled by $(1 \times 1 \times 27)$ and $(1 \times 1 \times 17)$ meshes in the **k**-space within Monkhorst-Pack scheme [38] for single and double unit cells, respectively. In order to treat partial occupancies, Methfessel–Paxton smearing method [96] is used. The width of smearing has chosen as 0.08 eV for geometry relaxation and 0.01 eV for accurate energy band and electronic density of states calculations. All atomic positions and lattice parameters have been optimized

Table 4.1: Computed lattice constants a and c (in Å) and E_g (in eV) for anatase and rutile phases of bulk TiO_2. Ultrasoft pseudopotential results are presented. Very similar results are obtained by using PAW potentials. Experimental values are also shown for comparison. The lattice constants for rutile are from Ref. [97, 98, 99] and for anatase are from Ref. [98, 99] while E_g data are from Ref. [104, 105].

	Anatase			Rutile		
	a	c	E_g	a	c	E_g
Calculation	3.81	9.76	2.3	4.64	2.98	1.9
Experiment	3.79	9.51	3.2	4.59	2.96	3.0

by using conjugate gradient method where total energy and atomic forces are minimized. The convergence for energy has been chosen as 10^{-5} eV between two ionic steps, and the maximum force allowed on each atoms is 0.03 eV/Å.

4.3 Results and discussions

First of all, pseudopotential of Ti and O atoms have been tested. Lattice parameters and energy band gap (E_g) of bulk rutile and anatase phases have been compared with available experimental data in Table 4.1. Lattice parameters a and c of rutile are 4.64 (4.59) and 2.98 (2.96) Å, respectively. The experimental values [97, 98, 99] are quoted in parentheses. For the case of anatase, a and c values are 3.81 (3.79) and 9.76 (9.51) Å which are in fair agreement with experimental values [98, 99]. Due to pseudopotentials, exchange–correlation approximation and methods used in calculations, lattice parameters can be slightly different from both experimental [97, 98, 99] and previous calculated values [100, 101, 102, 103]. Compared to the experimental data, maximum deviation appears with anatase c parameter (%2.6) while the variation of all the other lattice parameters from experimental values are less than %1. E_g values are 1.90 (3.03) eV for rutile and 2.30 (3.2) eV for anatase. These gap values are smaller than the experimental values [104, 105] which is a known deficiency of DFT calculations. In order to calculate correct gap values, it is necessary to go beyond standard DFT calculation

by including self–interaction corrections like GW calculations.

We have also checked the bond length in O and Ti dimer as well as TiO and TiO_2 molecules. O and Ti dimers have magnetic ground state and corresponding O–O and Ti–Ti bond lengths are 1.23 and 2.38 Å, respectively. TiO molecule prefers the magnetic ground state with magnetic moment value of $\mu = 2\mu_B$ where Ti–O bond length is 1.63 Å in good agreement with experimental values [72]. Bent TiO_2 molecule is about 2 eV energetically more stable than linear one and both structures prefer the singlet state. Ti–O bond length and O–Ti–O bond angle are 1.66 Å and 109°, respectively. Experimentally estimated value [41] of O–Ti–O angle is 110±5. Ti–O–O–Ti structure is unstable in linear Ti_2O_2 molecule. Upon relaxation of linear Ti–O–O–Ti molecule, two separated Ti–O molecules resulted by breaking O–O bond. In Ti–O molecule, Ti atom donates two electrons to O atom. According to Hund's rule, remaining unpaired d electrons of Ti cause to magnetization in this molecule. In contrast to TiO molecule, Ti atom gives all the valance electrons to p orbitals of two O atoms in TiO_2 molecule. As a result of this charge transfer, TiO_2 is a closed shell molecule and has paramagnetic ground state.

4.3.1 Ti_mO_m nanowires

Several single and double strain Ti_mO_m wires are investigated, and their optimized structures are presented in Figure 4.1. Wire structures include both simple and more complicated structures together. In order to quantify the relative stabilities of these wires, binding energy E_b per formula unit (f.u.) for Ti_mO_m wires is calculated in terms of energy of individual atoms, $E[Ti]$ and $E[O]$ for Ti and O atoms respectively, and the total energy of wire $E_T[Ti_mO_m]$ as,

$$E_b = (mE[Ti] + mE[O] - E_T[Ti_mO_m])/m \tag{4.1}$$

where m represents the number of Ti and O atoms. Variation of E_b with lattice constant c along the wire axis is shown in Figure 4.2.

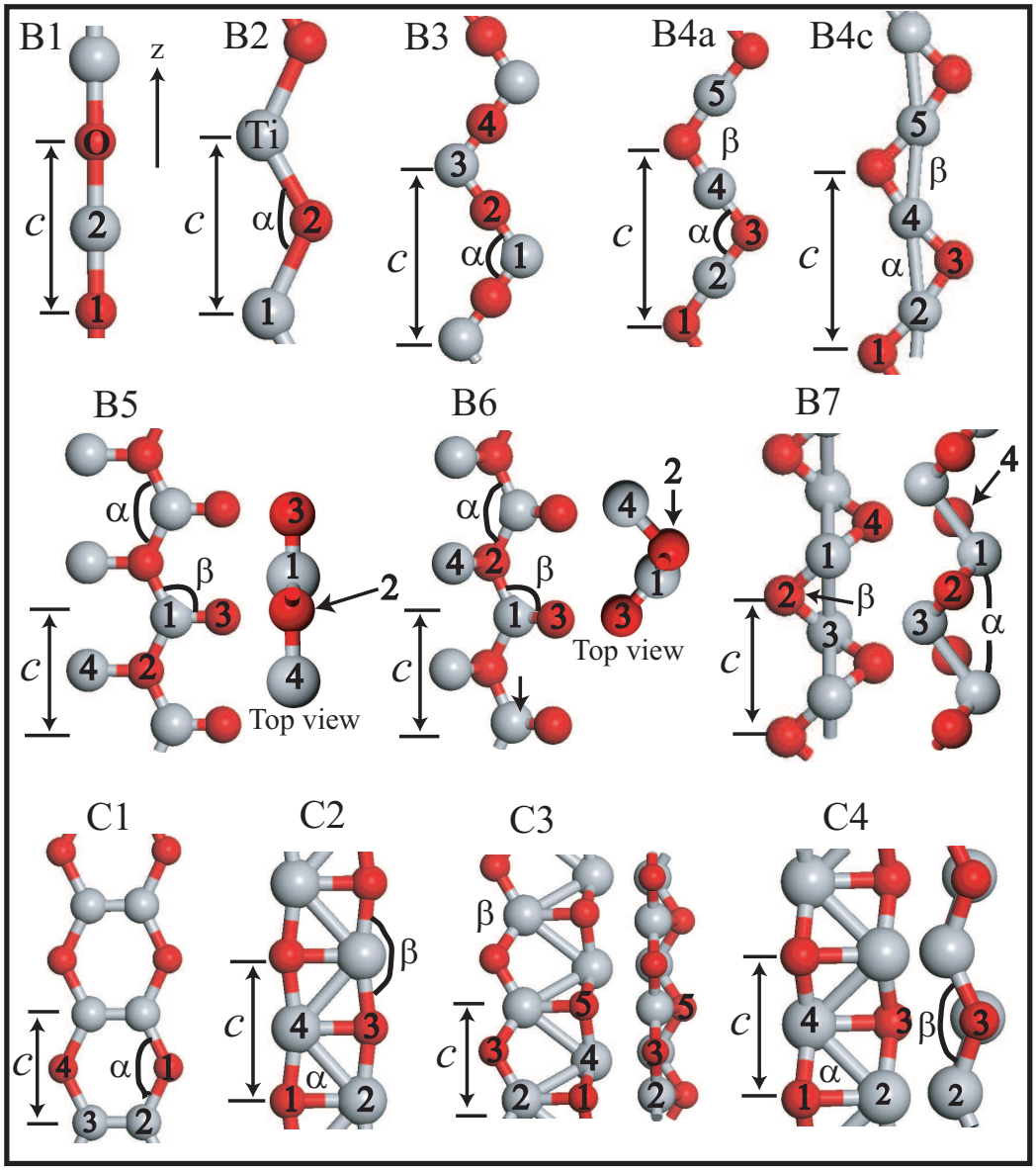

Figure 4.1: Optimized geometric structure of isolated Ti_mO_m nanowires. Assigned labels are indicated in order to identify each of the wire. Light and red balls are used to represent Ti and O atoms, respectively. Lattice constant c, distance between the numbered atoms and indicated angles α and β at equilibrium are compiled in Table 4.2.

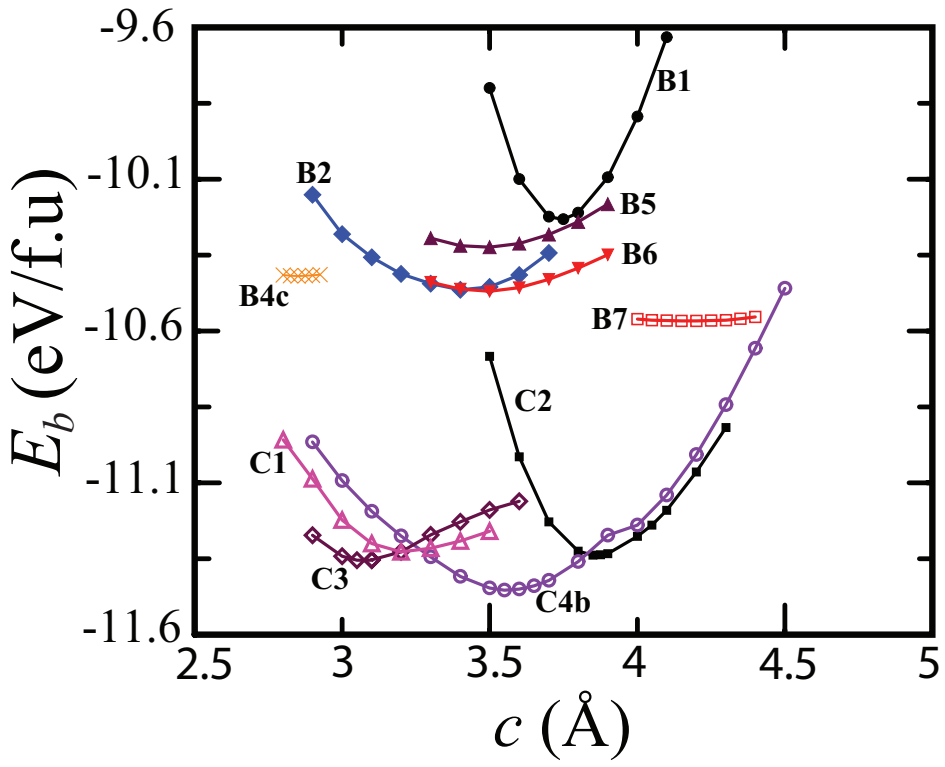

Figure 4.2: Variation of binding energy, E_b (eV/f.u.), with the lattice constant c in different Ti_mO_m wires. Lattice constant of B4c structures is multiplied by 0.5 in order to adjust the horizontal axis.

It is noticed that there are two different region along the energy axis in Figure 4.2. First region is between -10 and -10.5 eV and related to the single strain wires. Double strain nanowires are observed in the second region which is approximately 1 eV lower in energy than the previous one. Along the series of single strain wires, Ti atom is under–coordinated compared to the bulk structures, and coordination number is varied between one and three, depending on the structure. Remember that in bulk TiO_2, Ti and O atoms are 6–fold and 3–fold coordinated, respectively. On the other hand, in double strain systems which are more energetic, coordination number of Ti atoms becomes four. Therefore, we can infer that coordination number influences the strength of binding in these wires. In each

Table 4.2: Optimized lattice constant c_0 (in Å), interatomic bond distances d_{1-2}, d_{1-3}, d_{2-3}, d_{2-4}, d_{4-5} (in Å), angles α and β (in degree), and binding energies E_b (in eV/f.u.) of Ti_mO_m nanowires. Magnetic moment (μ) of the ferromagnetic wires are presented in terms of Bohr magneton μ_B.

wire	c_0	d_{1-2}	d_{1-3}	d_{2-3}	d_{2-4}	d_{4-5}	α	β	E_b	μ
B1	3.7	1.85							10.13	2
B2	3.4	1.83					136.6		10.26	2
B3	6.6	1.84		1.84	3.30		128.0		10.21	4
B4a	5.75	1.85		1.85	2.88	2.88	101.5	101.8	10.21	2.47
B4b	5.75	1.85		1.86	2.9	2.85	102.6	100.7	10.22	2.47
B4c	5.7	1.83		1.88	2.86	2.86	100.8	100.8	10.22	2.47
B5	3.5	1.95	1.64		1.87		127.7	116.3	10.12	2.87
B6	3.5	1.95	1.65		1.91		128	114.1	10.27	2
B7	4.15	1.84	2.62	1.85			104.9	90.4	10.37	
C1	3.2	1.82		2.70			122.8		11.12	
C2	3.9	1.98	2.93	1.94	2.62		83.0	166.1	11.14	
C3	3.1	2.00	3.31	1.84	2.78	2.81	67.4	115.2	11.15	1.05
C4a	3.55	2.00	2.98	1.93	2.59		82.0	133.9	11.16	2.19
C4b	3.55	2.02	2.99	1.91	2.54		80.6	136.1	11.24	
Bulk		2.14							12.91	

region, three dimensional (3D) wires (B6, B7, C3, C4) are more stable than planar (B1, B2, B3, B4, B5, C1 and C2) wire structures. Existence of pendant O or Ti atoms also affect the binding. B5 and B6 structures have both pendant Ti and O atoms. Coordination number of these pendant atoms is one. Formal oxidation states of Ti and O atoms are (+4) and (-2). As a result, these pendant atoms are under–coordinated and these atomic sites might be very reactive against to adsorbate atomic and molecular species. For the double strain wires, our initial starting geometry for structural minimization was planar, however for C3 and C4 wires planar structure is not preserved during the geometry optimization. Lattice parameter along the nanowire axis, some bond angles and interatomic bond distances between the atoms labeled in Figure 4.1, magnetic properties and E_b of Ti_mO_m wires at their ground states are summarized in Table 4.2. Bulk

TiO is also included in this Table for comparison. Crystal structure of bulk TiO is sodium chloride (NaCl) structure and each Ti atoms has six nearest neighbor O atoms (octahedral coordination). Due to high coordination of atoms in bulk TiO compared to nanowires, interatomic bond distance between Ti and O atom is 2.14 Å. Energy difference between the E_b of most energetic nanowire studied here, C4b, and cohesive energy of bulk TiO is 1.67 eV.

More insight about the stability and bonding nature of these nanowires can be provided by examining three isomers of B4 structure. B4a is uniform B4 in which $d_{2-4} = d_{4-5}$. Next isomer is shaped by forming Ti–Ti dimers, so B4 nanowire gains very small energy (about 10 meV) with respect to the B4a structure. This structure is called B4b and $d_{2-4} \neq d_{4-5}$. Third isomer is B4c structure, in which B4 wire gains further energy upon formation of internal Ti zigzag chain. B7 structure can be obtained by compression of B4 chain. It can be easily seen from Figure 4.1 or Table 4.2 that lattice constant of B3 chain is the largest. One of the O (Ti) atom in double cell of B2 is rotated 180° to obtain B3 (B4) structure. In other words, the B3 or B4 wires are formed by combining linear O–Ti–O units which are less energetic than bent O–Ti–O units (see B2 structures). On the other hand, in B4 structure, repulsive O–O interaction is small relative to one of B2 wires. Hence, the lattice constant of B4 (B3) structure is very large comparative to other single strain wires in order to minimize repulsive O–O interaction that would compensate the energy loss due to the linear O–Ti–O units.

Most of the structures have magnetic ground state. However, in both single and double strain wires, non-magnetic wires (B7 and C4b) have the lowest energy. In C4 structure, energy differences between the magnetic and nonmagnetic states is 193.6 meV. Structural parameters of these magnetic and nonmagnetic isomers are not so different. B4 isomers have almost equal magnetic moment which is $\mu = 2.47\mu_B$, while the related wire structure B3 has the largest magnetic moment, $4\mu_B$. Magnetic moment of B1 and B2 are $2\mu_B$. On the contrary, ground state of bulk TiO structure is paramagnetic.

In general, Ti_mO_m wires exhibit metallic behavior as seen in Figure 4.3 while C1, C4b, B3 and B7 structures are semiconductor. Figure 4.3(a–d) shows the

electronic band structure of double strain wires whereas the ones of single strain wires are collected in Figure 4.3(e–h).

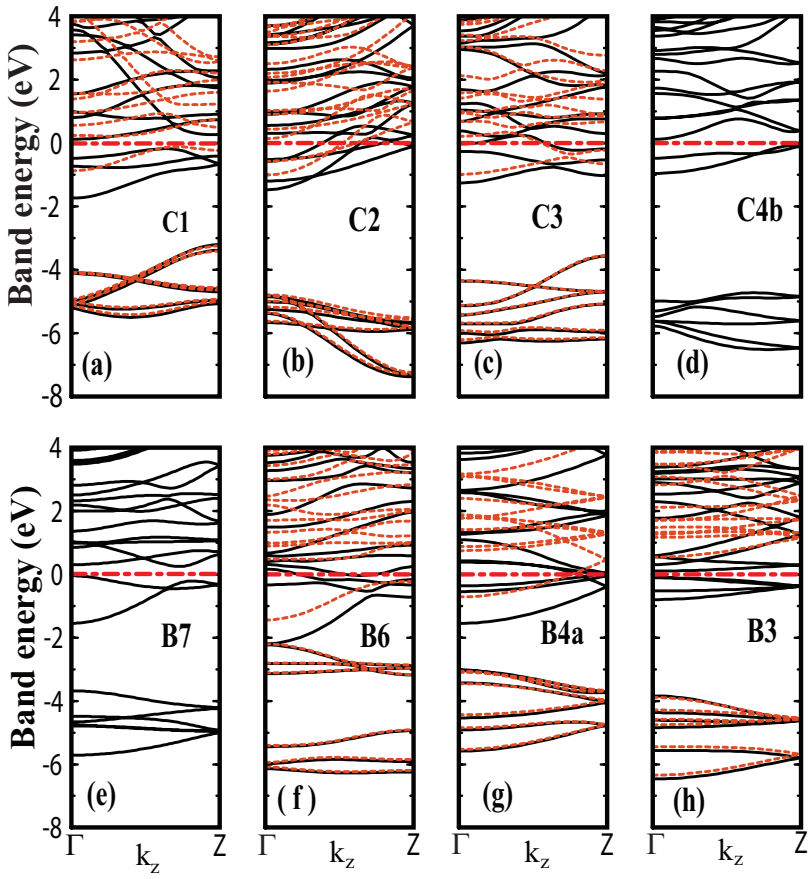

Figure 4.3: The band structure of the selected Ti_mO_m wires. Fermi level of metallic systems shown by dashed lines marks the zero of energy. For magnetic systems, majority (minority) spin components are represented with dark solid (orange dashed) lines.

In the band structure of lowest energy structure, C4b, conduction band and valance band edges are very close to the E_F at Γ and Z points, respectively. E_g is 0.19 eV and has indirect nature for this nanowire. In most of the band structures, there are couple of bands below the Fermi level, E_F, and then a large band gap of a few eV's occurs. For example, in the electronic band structure of C4b wire shown in Figure 4.3(d), there are two bands located just below the E_F

before a band gap of approximately 4 eV, and they are occupied by 4 electrons. If we remove four electrons one by one from C4B wire, E_F goes down in energy in the calculated band structure of charged C4b nanowire, and eventually wire becomes a semiconductor. A similar situation happens for the other Ti_mO_m nanowires. Therefore, it is possible to infer that the stability of Ti_mO_m wires might be enhanced upon adsorption that yield a charge transfer from these wires. Interestingly, B6 exhibits half metallic behavior. While, this nanowire is metallic for the spin up electrons, it is an indirect band gap semiconductor with a E_g of 0.74 eV for spin down electrons.

4.3.2 Ti_mO_n nanowires

A large number of different possible initial wire geometries have been optimized by conjagute gradient minimizations in order to find the ground state structures of Ti_mO_n nanowires. Total energy of these structures is minimized with respect to lattice constant along the wire axis as well. Optimized nanowire geometries are presented in Figure 4.4. Similar to the TiO wires, E_b per formula unit (f.u.) of Ti_mO_n wires have been calculated in terms of the energies of individual atoms ($E[Ti]$ and $E[O]$ for Ti and O atoms , respectively) and the total energy of wire, $E_T[Ti_mO_n]$, as

$$E_b = (mE[Ti] + nE[O] - E_T[Ti_mO_n])/(n-m) \tag{4.2}$$

where m and n (=$2m$, like TiO_2 unit) stand for the number of Ti and O atoms in the unit cell, respectively. E_b versus lattice constant c along wire axis is illustrated in Figure 4.5. Lattice parameter along the nanowire axis, bond angle and interatomic bond distances between the atoms labeled in Figure 4.4, binding energy E_b, and energy band gap E_g of Ti_mO_n wires at their ground states are summarized in Table 4.3. The stability and possibility of formation of TiO_2 nanowires can be investigated by comparing E_b of these nanowires with that of bulk phases of TiO_2. It is known that rutile phase of titania is thermodynamically more stable than anatase phase. E_b per f.u. for rutile phase is 20.51 eV.

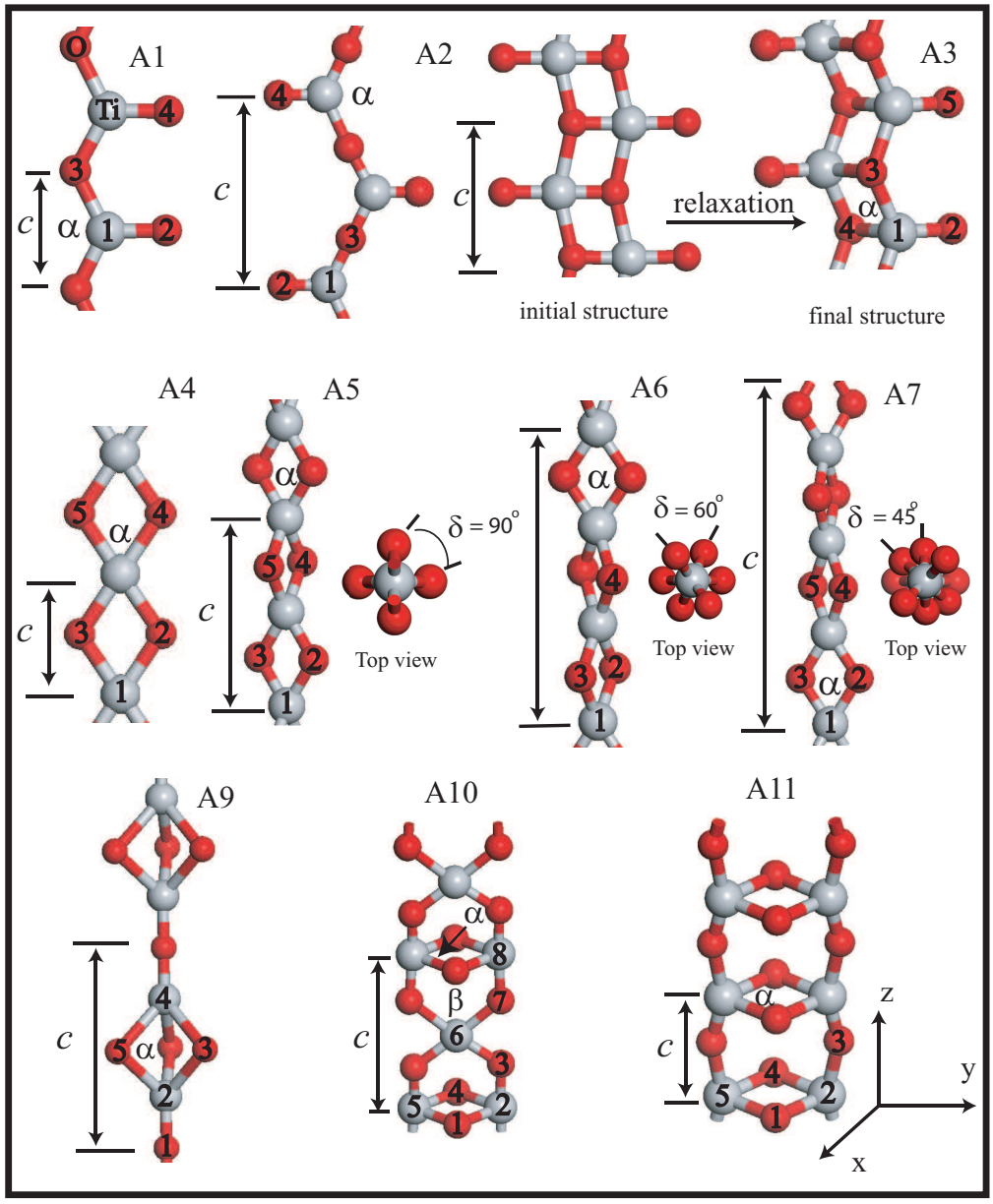

Figure 4.4: Atomic structure of isolated Ti_mO_n wires. Assigned labels are indicated in order to identify each of the wire. Grey and red balls are used to represent the Ti and O atoms, respectively. Lattice constant c, distance between the numbered atoms and indicated angle α at equilibrium are summarized in Table 4.3.

The binding energy with respect to the cohesive energy of bulk rutile phase, E_b^r, might be defined as E_b^{wire}-E_b^{rutile}. Here, E_b^{wire} and E_b^{rutile} are the binding energies of an isolated nanowire and rutile bulk titania. E_b^r is also included in Table 4.3. $E_b^r > 0$ means that bulk rutile is more stable than a particular wire structure. It is observed that E_b^r is negative for all TiO_2 nanowires. But in our calculations, the total energy, not the free energy of these phases has been calculated.

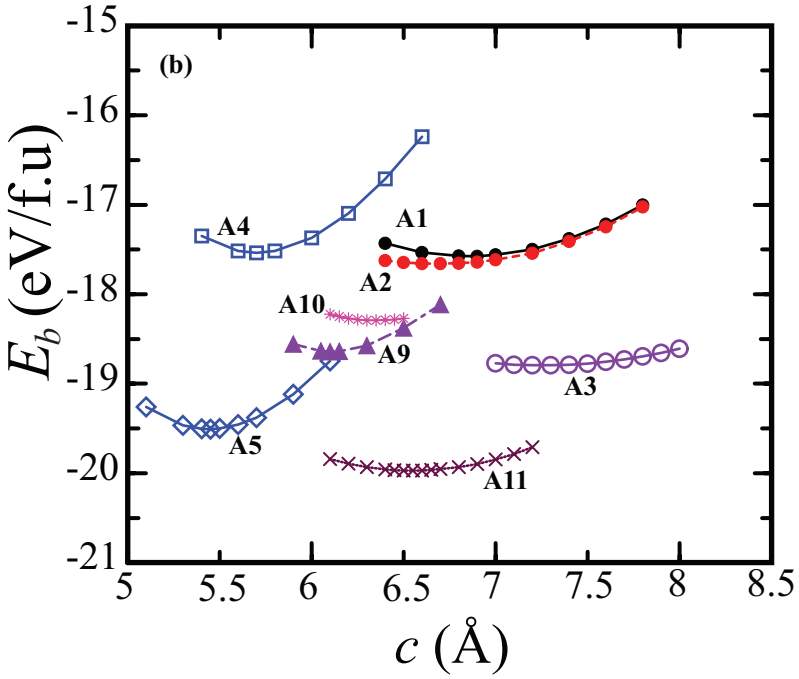

Figure 4.5: Variation of E_b (eV/f.u.) with respect to the lattice constant c along the wire axis in different Ti_mO_n nanowire structures. Lattice constant of A1, A3, A4 and A11 structures are multiplied by 2 for an appropriate horizontal axis.

The A1 and A2 wires have related structures. In a double cell of A1 geometry, one of the low coordinated O atoms is rotated by 180° with respect to the other low coordinated O atom to obtain the A2 structure. Difference between E_b's of these two structures increases (decreases) when lattice constant decreases (increases). For larger lattice constants, interaction between the two low coordinated O atoms

Table 4.3: Optimized lattice constant c_0 (in Å), interatomic bond distancess d_{1-2}, d_{2-3}, d_{1-3}, d_{1-4}, d_{2-4}, d_{2-5} (in Å), α (in degree), binding energy E_b and E_b^r (binding energy with respect to rutile bulk binding energy) (in eV/f.u.) of Ti_mO_n nanowires. The energy band gap (in eV) of the semiconducting wires are also reported. E_b of rutile bulk phase is included for comparison. The definitions of E_b and E_b^r are given in the text.

wire	c_0	d_{1-2}	d_{2-3}	d_{1-3}	d_{1-4}	d_{2-4}	d_{2-5}	α	E_b	E_b^r	E_g
A1	3.45	1.64		1.88		3.45		133.6	17.37	3.14	1.98
A2	6.70	1.65		1.86		6.70		128.1	17.47	3.04	1.96
A3	3.65	1.64		1.98	1.99			84.5	18.60	1.91	2.45
A4	2.85	1.89	2.48			2.85		82.1	17.33	3.17	0.8
A5	5.45	1.85	2.51			3.25		85.4	19.30	1.20	2.98
A6	8.25	1.86	2.51			3.00		84.7	18.89	1.62	
A7	11.1	1.87	2.5			2.9		84.2	18.43	2.06	
A9	6.10	1.85	1.89			2.40		79.7	18.44	2.07	2.52
A10	6.35	1.82	1.83		2.55		2.60	88.8	18.09	2.42	1.33
A11	3.28		1.85		2.48	1.84	2.72	84.6	19.76	0.74	3.68
rutile									20.51	0.00	1.90

decreases in the A1 structure. As a result, E_b's of A1 and A2 begin to get closer to each other. The difference between E_b's of A1 and A2 geometries at equilibrium is 168.6 meV. The distance between adjacent O atoms affects the stability of wires. O atom prefers to make its coordination at least two. A1 and A2 wires have pendant O atoms. Relative stability of these isomers is reduced by these pendant atoms. Ti–O bond length (d_{1-2}) between pendant O and the nearest Ti atom is %10 shorter than other nearest neighbor bond distances as seen in Table 4.3.

A double strand wire is formed by combining two A1 wires, this initial structure of A3 wire is not stable. The structural optimization starting from this planar geometry yield either A3 wire shown in Figure 4.4 or two separate weakly interacting A1 nanowires. When the planar geometry is constrained during the optimization, the structure is transformed into two separated A1 structures. However, the former is energetically more favorable than the latter. The structures of A4 and A5 wires resemble to each other. In the A5 structure, one of the in–plane

O pairs, namely O(2) and O(3), has been rotated by 90° with respect to the other in–plane O pair, O(4) and O(5). When one O pair (e.g. O(2)–O(3)) of the A4 wire has been slightly rotated, the disturbed wire transforms into the A5 wire upon relaxation of the perturbed structure. There is no energy barrier between A4 to A5 structures. The distance between two O atoms, namely 2 and 4, (d_{2-4}) in A4 and A5 structures is 2.85 and 3.25 Å, respectively. Therefore, the repulsive interaction strength between O pairs in A5 is lower than that in A4. Hence, binding in A5 wire enhances, where A5 wire is 3.94 eV more energetic than the A4 structure. Cluster model of the A5 structure have been studied previously [57]. At each end of the cluster, the pendant O atoms bind to the Ti atoms in an antisymmetrical manner. E_b per f.u. increases with increasing number of TiO_2 units. Therefore, infinite A5 wire is the upper limit of E_b in these clusters.

We have also formed the helical structures (A6, A7 and A8) from A4 wire in order to investigate the relative stability of A4 and A5 structures. Each O pair has been rotated with respect to nearest O pairs with a rotation angle δ of 60° in A6, 45° in A7 and 36° in A8 structure as seen in Fig 4.4. The distance d_{2-4} in A6, A7 and A8 wires is longer than that in the A4 structure. The distance d_{2-3} affects the coupling between the in–plane O atoms. When it is compared within the series of A4 to A8 wires, the value of d_{2-3} starts to decrease from A5 and reaches its minimum value at A4 wire. So, it is the longest (shortest) in the A4 (A5) structure. Bond lengths d_{1-2} and d_{2-3} in A6, A7 and A8 wires are between d_{1-2} and d_{2-3} of the A4 and A5 wires. Therefore, helical structures are energetically more stable than A4. E_b reaches its maximum value when δ=90°. E_b of these helical structures are between those of A4 and A5. While A4 wire sets the lower limit of E_b, upper limit of E_b occurs at A5 structure. A8 structure does not preserve the initial helical structure and tends to change its structure to A5. Hence, as a result of structural optimization, we have obtained an irregular helical structure for this case.

Coordination number of Ti atoms also strongly influences the binding of nanowires. Binding increases with increasing coordination of Ti atoms. For example, in A2 and A4 geometries, the coordination number of Ti is three and four, respectively. Coordination number also changes the bond lengths, the bond

lengths increase when the coordination number of atoms increases. When the pendant O atoms in the A1 and A2 structures are removed, one obtains the TiO zigzag chain presented in Figure 4.1. Due to the pendant O atom, d_{1-3} in A1 is %2.7 longer than d_{1-2} in TiO zigzag wire. The bond angle α in A1 is %2.2 smaller than the bond angle in TiO zigzag structure. Consider the B3 wire formed upon removal of the pendant O atoms of the A2 structure. The lattice constants of B3 and A2 structures differ only by 0.1 Å. Energy gain E_{gain} of B3 wire at equilibrium upon adsorption of two O atoms can be calculated with the following formula: $E_{\text{gain}} = (E_T[\text{A2}] + 2E[\text{O}] - E_T[\text{B3}])$. $E_T[\text{A2}]$ and $E_T[\text{B3}]$ are the total energies of A2 and B3 wires at c =6.6 Å. The energy gain upon adsorption of two O atoms at pendant sides (atom 1 and atom 3 shown in Figure 4.1) in B3 wire is 14.51 eV. Ti_mO_n and Ti_mO_m wires can be transformed into each other by adding or removing O atom. However, Ti and O atoms tend to reach the sufficient coordination number to support their formal oxidation states. Therefore, Ti_mO_m wires gain huge energy upon adsorption of O atoms.

In general, TiO_2 nanowires tend to form three dimensional (3D) structures. Planar structures have relatively lower binding energy than 3D structures. Compared to the other wires, the energy of the wire does not change so much upon compression or stretching of A1, A2, A3, and A11 wires as seen in Figure 4.5, and similarly B5, B6, and B7 TiO nanowires as depicted in Figure 4.2 Variation of E_b with respect to the lattice constant c along the wire axis is wider and shallower for these wires. In the A5 case, the distance between O(2) and O(3) (or O(4)–O(5)) atoms decreases, while wire is being pulled along the z-axis. As a result of the increase in the repulsive O–O interaction during stretching, E_b rises rapidly compared to A3 or A11. Magnetic properties have also been investigated for all wire geometries. All studied wires have non magnetic ground state in their equilibrium structures.

Electronic properties of Ti_mO_n wires are explored by band structure calculations, and the relation between electronic properties and stability of these wires is investigated. Electronic band structures of some selected nanowires are presented in Figure 4.6. As infered from Figure 4.6, all studied Ti_mO_n nanowires are semiconductors. Energy band gaps, E_g, range from 0.8 eV to 3.68 eV compared to the

1.90 eV calculated band gap of bulk rutile. There is a direct correlation between E_g and E_b. In general, E_g increases with increasing E_b. We have examined in detail how the band structures are modified between similar structures ((A1, A2, A3) and (A4, A5)). For example, there is a dramatic differences between the band structures of A4 and A5 wires.

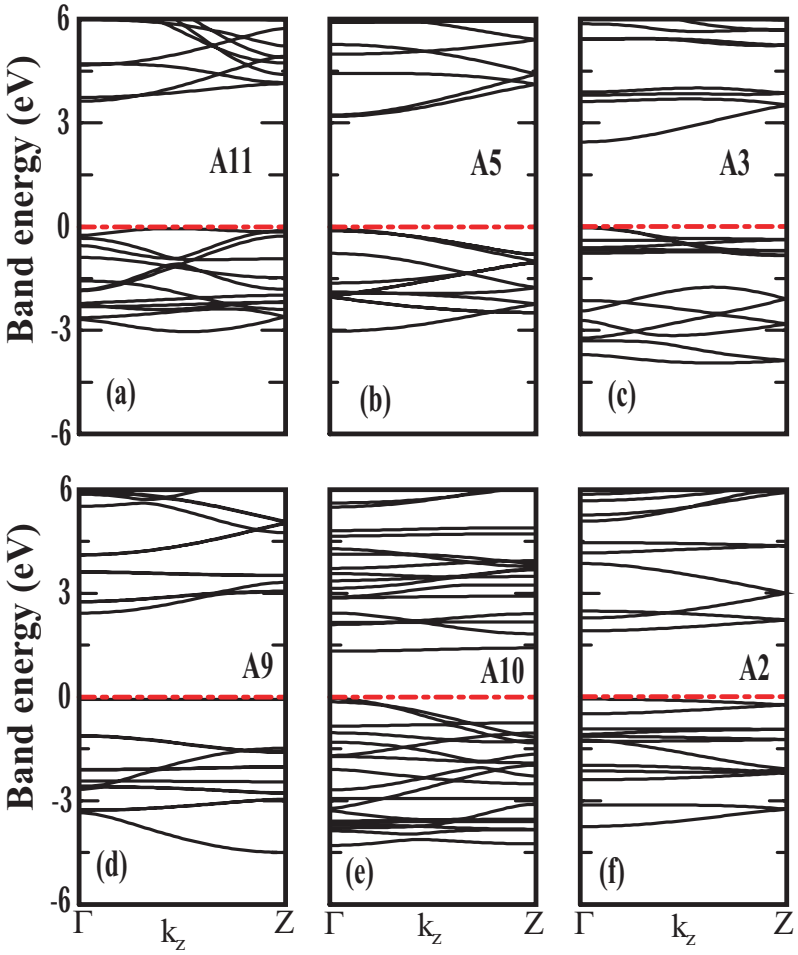

Figure 4.6: The band structure of the selected Ti_mO_n nanowires. Fermi level of these semiconductor wires are shown by dashed lines marks the zero of energy which indicates the top of the valence band.

In the A4 structure, the band gap has indirect nature and the value of E_g is about 0.8 eV. E_g is about 2.98 eV for A5 wire, moreover its character is changed

to a direct band gap. Remember that E_b of A5 is 1.97 eV lower than the one of A4 wire. The band gap behaviour with different rotation angles, δ, of one of the O pair (see Figure 4.4) of A4 or A5 wire is studied in detail and is presented in Figure 4.7. The equilibrium structure of A5 (A4) is taken, and one of the O pair is rotated gradually ending up in the A4 (A5) structure. Electronic band structure calculations are carried out without relaxing the modified structures. Double unit cell is used for the calculations of the A4 structure for direct comparison with the A5 results. This way, as displayed in Figure 4.7, two different E_g versus rotation angle δ curves are resulted depending on the path, i.e. starting from A5 structure and ending with A4 wire or vice versa. E_g's of these rotated structures are between those of A4 and A5 wires. E_g decreases from A5 to A4. Hence, electronic structure is very sensitive to rotation, elongation, and contraction in the A4 and A5 structures. So, it is possible to tune the electronic behaviors of these wires by applying tension.

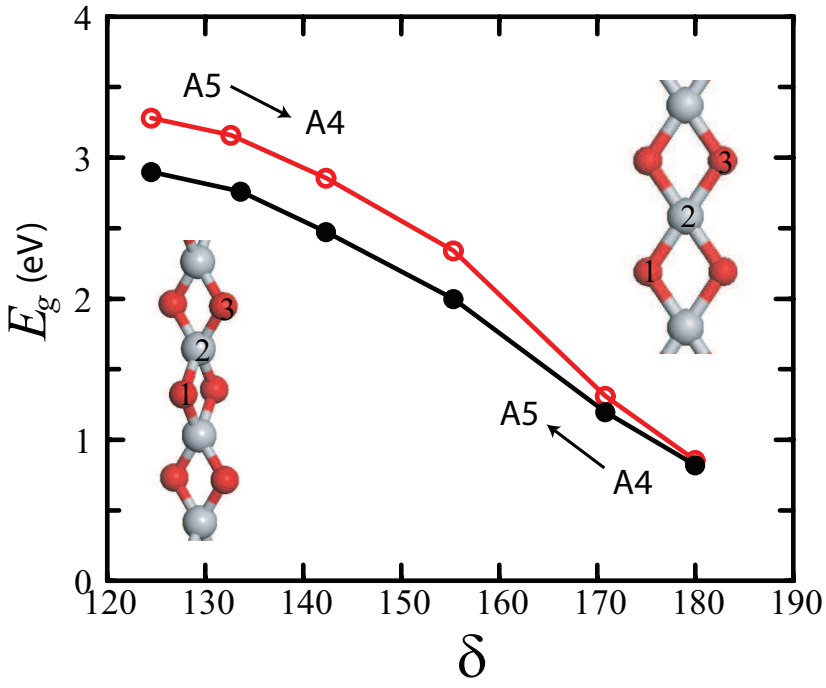

Figure 4.7: Variation of band gap E_g of A4 and A5 wires with the rotation angle δ which is the angle among O1–T2–O3 atoms (see Figure 4.4).

A1 and A2 structures have similar electronic band structures. Nature of the band gap is direct. E_g of A1 and A2 is 1.98 and 1.96 eV, respectively. A3 is more stable than A1 and A2. Hence, it is expected that it has a relatively large E_g, which is calculated as 2.45 eV. A11 structure is the most stable structure. Its E_g is 3.68 eV and the band gap is indirect. In Ti_mO_n wires, Ti and O atoms have 10 ($p^6d^3s^1$) and 6 (s^2p^4) valence electrons, respectively. Ti atoms donate their 4 electrons to two O atoms to fill the unoccupied states of O atom. This behaviour causes the semiconductor nature of Ti_mO_n wires.

Stoichiometric and non-stoichiometric thin Ti–O wires can be formed on TiO_2 surfaces upon reconstruction or annealing. Therefore, it is important to understand structural, magnetic and electronic properties of these nanowires. Unlike stoichiometric TiO_2 nanowires, Ti_2O_3 quasi–1D chains formed on reconstructed rutile [110] surface exhibit metallic behavior [88]. Moreover, we have both metallic and semiconducting Ti_mO_m nanowires. As a result, it is expected that stoichiometry strongly influences the electronic properties of Ti–O nanowires.

4.3.3 Bulk–like rutile (110) nanowires

Finally, we have studied the structural and electronic properties of bulk like TiO_2 nanowires. These nanowires have been cut in rod–like forms from the ideal bulk rutile crystal. Nanowires are oriented along rutile [110] crystallographic direction and each nanowire has different diameter. All of them have rectangular cross section and they have two (110) and (001) lateral surfaces. It is known that (110) surface is the most stable surface among the rutile surfaces. Figure 4.8 shows the optimized structure of some of these nanowires. We have calculated the E_b of these 1D structure as a function of number of TiO_2 units. It is important to figure out how the stability and electronic properties of these nanowires evolve as the cross section changes. The comparison of E_b of A5, A11, and TiO_2 bulk like nanowires is shown in Figure 4.9. It is noticed that bulk wires are more energetic than A5 structure. However, A11 structure is slightly more stable than $Ti_{10}O_{20}$ and $Ti_{21}O_{42}$ nanowires. There is a crossover after the $Ti_{21}O_{42}$ nanowire, and the bulk wires with larger radius than this nanowire become more energetic. Internal

regions of $Ti_{28}O_{56}$ and $Ti_{45}O_{90}$ nanowires exhibit more bulk like behavior. Rutile phase is 0.5 eV more energetic than $Ti_{45}O_{90}$ nanowire. Structural distortion of initial structure of bulk like wires upon geometry optimization decreases as the cross section increases.

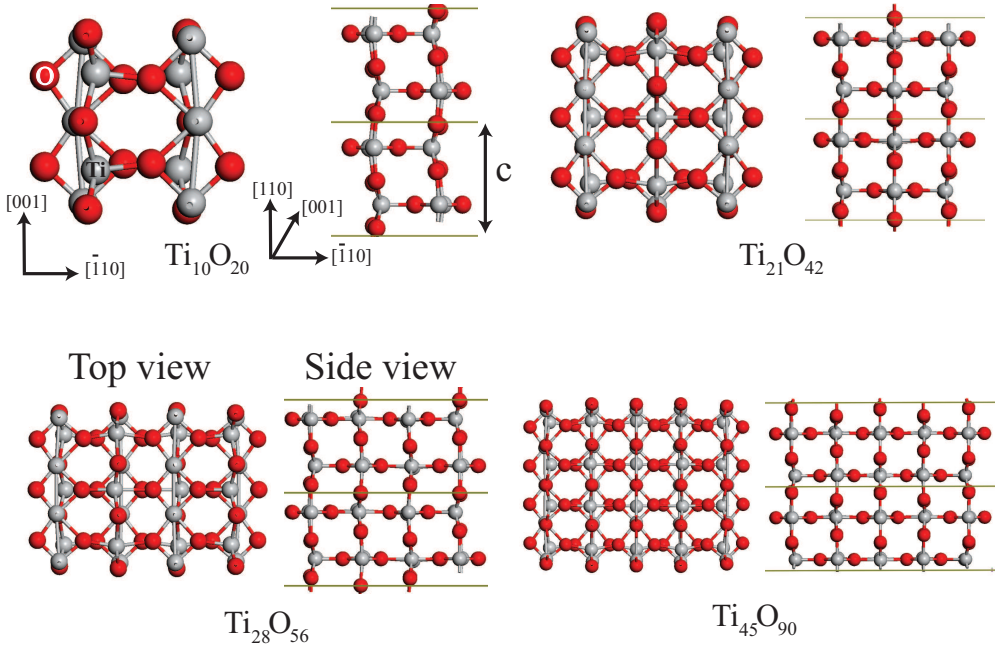

Figure 4.8: Top and side view of the optimized geometric structure of the bulk like TiO_2 nanowires extended along the rutile [110] direction. Grey and red balls are used to represent the Ti and O atoms, respectively.

In Figure 4.10, we have shown the band structure of these rutile (110) nanowires. Bands around the Fermi level E_F has mainly O $2p$ character. The lowest conduction bands are very flat and has d character. Except $Ti_{10}O_{20}$, all nanowires have direct gap. In $Ti_{10}O_{20}$ case, indirect energy gap is slightly smaller than direct one. E_g of these nanowires is displayed in Figure 4.9. E_g shows an oscillation around 1.75 eV which is close to theoretical E_g of bulk rutile.

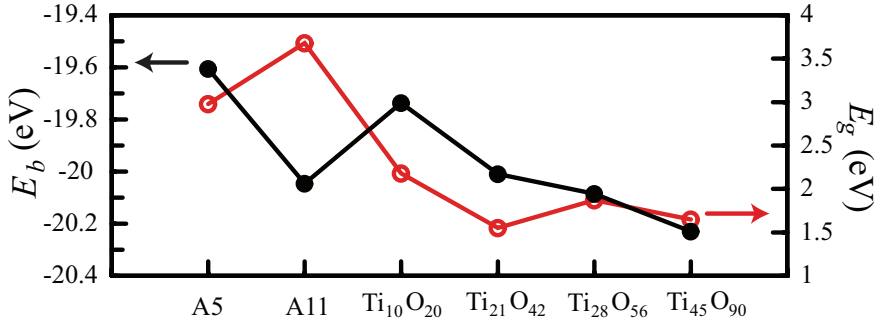

Figure 4.9: Comparison of the atomically thin and bulk like TiO_2 nanowires. E_b and E_g are given in eV.

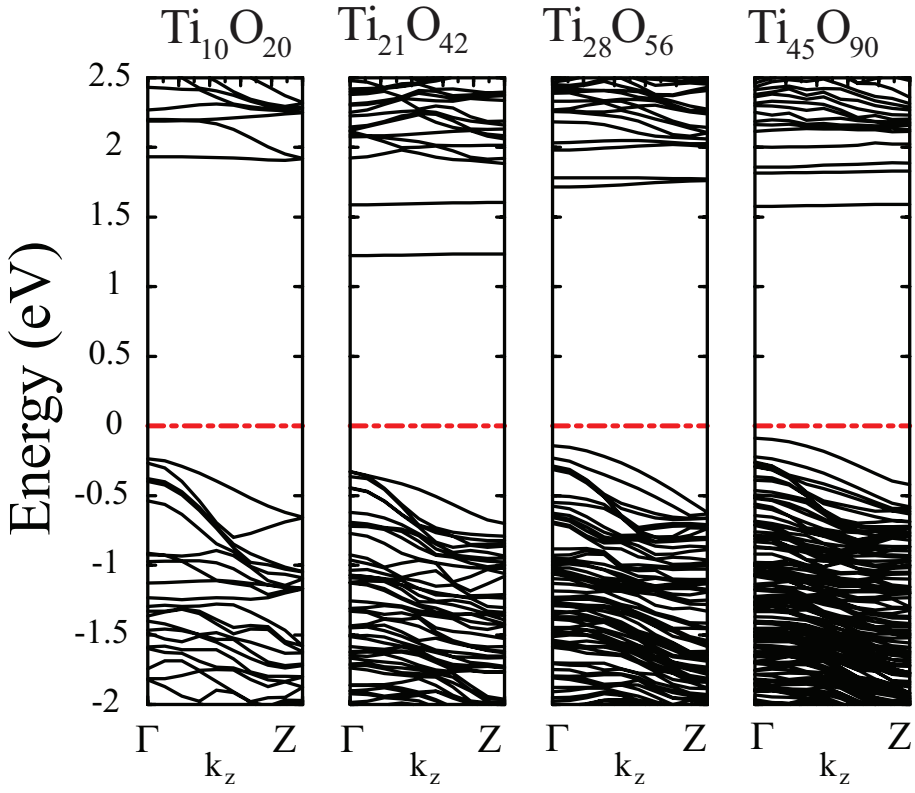

Figure 4.10: The band structure of the various bulk-like rutile (110) nanowires. Fermi level is represented by dotted–dashed lines.

Chapter 5

Adsorption of BrPDI, BrGly, and BrAsp on anatase TiO_2 (001) surface for the dye-sensitized solar cell applications

In this chapter, we have reported the electronic properties of unreconstructed (UR) and reconstructed anatase TiO_2 (001) surfaces with the PDI–based dye molecules adsorbing. We have obtained both adsorbate–induced occupied gap levels and band gap narrowing. These results are essential for photovoltaic and photocatalytic applications. For these applications, adsorbate-surface system must be stable to illumination and following physical and chemical processes. Moreover, electronic structure of whole system including surface and adsorbed dye molecule has ability to absorb a large part of the solar spectrum.

5.1 Method

We have performed first-principles plane wave calculations [21, 39] within density functional theory (DFT) [30] using projected augmented-wave (PAW) potentials [36]. $3p^6 3d^3 4s^1$ for Ti and $2s^2 2p^4$ configuration for O have been used in pseudopotentials. The exchange correlation potential has been approximated by Generalized Gradient Approximation (GGA) by using PW91 [32] formulation. Because of the large size of the dye molecules and to study the different coverage of surfaces, the anatase (001) surface has been modeled by both periodic 2×4 (7.606 and 15.212 Å) and 4×4 (15.212 and 15.212 Å) slabs with four layers of TiO_2 slabs containing at least 192 atoms. The vacuum between the bottom of the slab and the top the absorbed molecule has been taken at least 8 Å. Isolated dye molecules have been relaxed in a large tetragonal supercell. To prevent interaction between adjacent isolated molecules, a large spacing between the dye molecules (8 Å) has been taken. We have used both unreconstructed and reconstructed surfaces. We have imposed some criteria for the choice of these supercell dimensions. First of all, these supercells must be large enough to give possibility to search different adsorption sites and to prevent the interaction between periodic images of dye molecules. Secondly, they must be thick enough to reasonably reproduce most of the TiO_2 bulk properties. In all calculations, only one side of the slab has been allowed to relax and the atoms in the bottom layer have been fixed to their bulk truncated position. In the self-consistent potential and total energy calculations, Γ point and three special ***k**-point* have been used for 4×4 and 2×4 supercells, respectively [38]. A plane-wave basis set with kinetic energy cutoff (E_{cut}) 500 eV has been used. All atomic positions have been optimized by using conjugate gradient method where total energy and atomic forces are minimized. Maximum force allowed on each atom has been chosen as 0.06 eV/Å.

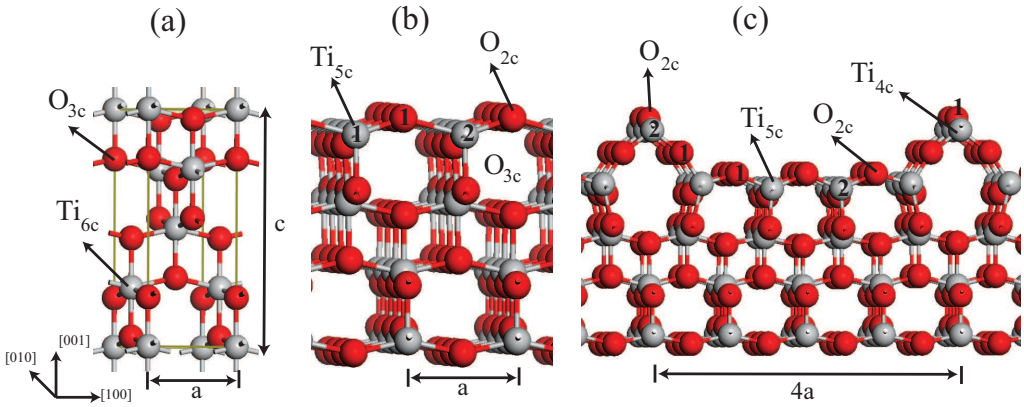

Figure 5.1: Side views of the (a) bulk anatase, (b) relaxed (1 × 1) and (c) (1 × 4) reconstructed anatase surfaces. a (=3.803 Å) is the calculated bulk lattice constant. The coordination of some of the atoms is shown.

5.2 Results and Discussions

5.2.1 Anatase (001) surface

Figure 5.1 (b) and (c) show the structure of unreconstructed (UR) and reconstructed (RC) anatase TiO_2 (001) surfaces, respectively. UR surface has twofold and threefold coordinated O and fivefold coordinated Ti atoms. In RC structure, we have both fourfold and fivefold coordinated Ti atoms. Ti and O atoms are sixfold and threefold coordinated in bulk anatase, respectively. Existence of undercoordinated atoms influence the chemical and physical properties of surfaces. There is a breaking of the symmetry at the UR surface upon relaxation. In the relaxed structure of UR surface, we have inequivalent O–Ti bridge bonds with lengths of 2.21 and 1.76 Å for O1–Ti1 and O1–Ti2, respectively. Ti1–O1–Ti2 bond angle is 146.3°. 1 × 1 anatase (001) surface is not very stable. However it can be stabilized upon hydration or reconstruction of surface obtained with heating to elevated temperatures. For the RC surface case, we have taken the reconstruction model, namely ad-molecule (ADM) model, proposed by Lazzeri *et al* [106]. According to this model, stress of surface is released upon reconstruction. Strong asymmetric O–Ti bridge bonds disappear and resulting Ti1–O1 bridge bonds range from 1.79 to 1.98 Å in length. We have also calculated the surface energy (E_{surf}) of UR and RC surfaces through the following formula:

$E_{\text{surf}} = (E_T[\text{slab}] - E_T[\text{bulk}])/(\text{total exposed area})$. $E_T[\text{slab}]$ and $E_T[\text{bulk}]$ are the total energies of the slab and the bulk anatase containing equal number of TiO_2 units with the slab. The calculated E_{surf} is 0.122 and 0.087 eV/Å^2 for UR and RC structures, respectively. It is noticed that UR surface is energetically unstable compared to RC.

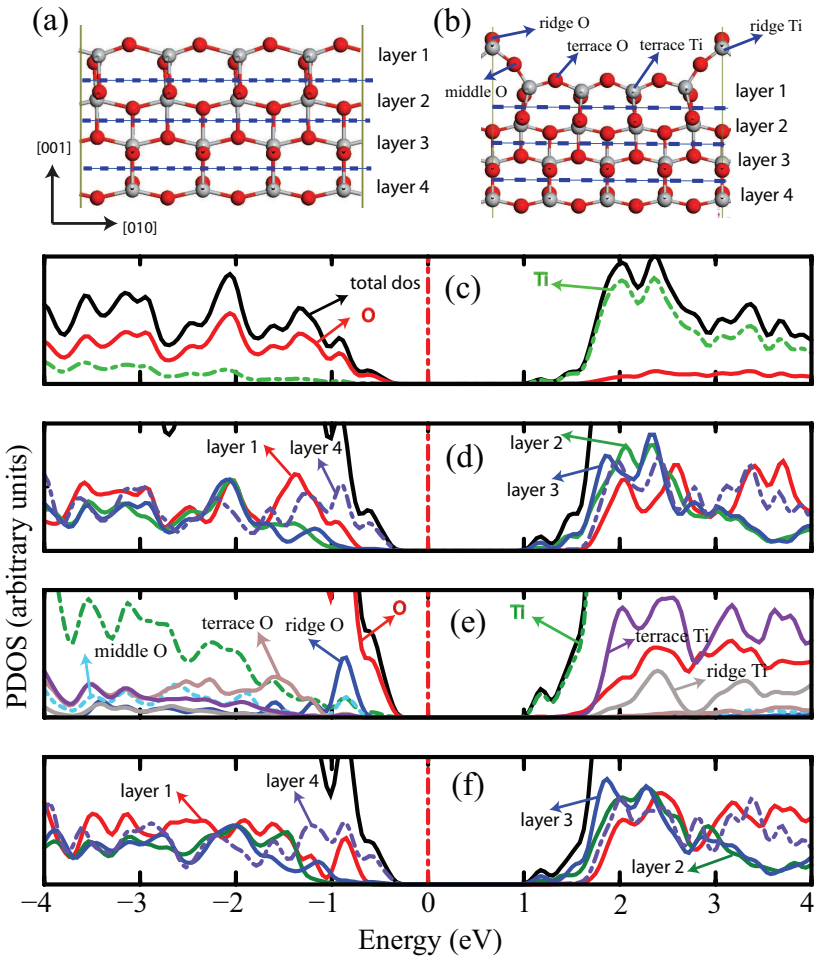

Figure 5.2: Optimized structure of (a) UR and (b) RC surfaces. Each slab has been decomposed into four layers. Description of these layers are presented in the text. Total, Ti and O projected DOS of UR surface in (c) and decomposition of total DOS into the four slab layers of UR urface in (d) are shown. Decomposition of total DOS into some selected O and Ti atoms of RC surface in (e) is depicted. In (f), contribution of four slab layers to the total DOS is shown.

Figure 5.2 shows both total and atom decomposed DOS for UR and RC surfaces. In both surfaces, upper part of the VB ($-2 \leq E(in\ eV) \leq 0$) is mainly composed of $2p$ states of O atoms. $3d$ states of Ti atoms form the lower part of the CB. We have also decomposed total DOS into partial DOS of separated four layers, see Figure 5.2 (a) and (b) for the description of these layers. Layer 1 for both UR and RC surfaces is the externally relaxed plane and layer 4 corresponds to unrelaxed plane which represents the bulk region. Layers 1 and 4 are located at the upper part of the VB while layers 2 and 3 contribute to the lower part of the VB. Because of the existence of the undercoordinated atoms in the outer layers compared to those in the inner layers, layer 1 and layer 4 are less stable than inner layers. As a result, energy levels of the external layers move to higher energies. Layer 4 is not allowed to be relaxed during the optimization. Therefore, shifting of a particular energy level to the higher energies is more pronounced for the energy level coming from layer 4. In RC case, we have different coordinated O and Ti atoms at the surface. Contribution of these atoms to total DOS is shown in Figure 5.2 (e). Ridge Ti and O atoms are fourfold and twofold coordinated, respectively. We have fivefold coordinated Ti and twofold coordinated O atoms at the terrace region of RC surface. It is noticed that upper part of the VB is mostly populated by ridge O atoms. Moreover, ridge Ti atoms are undercoordinated. As a results of these arguments, we can conclude that ridge region is more reactive than the terrace region.

5.2.2 Dyes

We have considered perylenediimide (PDI)–based dye compounds with two Br ions bonded to it and various carboxyl groups attached to it, namely, the glycine (Gly) and aspartine (Asp) groups. Carboxyl groups bond to ends of dye molecule asymmetrically. Optimized structure of BrPDI, BrGly and BrAsp are given in Figure 5.3. Due to attached Br atoms, dyes are not planar in their ground states. There is a twisting of the molecule which might be a result of the repulsive stress between Br and its nearest–neighbor hydrogen. These molecules can be excited under visible light. Therefore, they have potential to be used in production of

dye sensitized solar cells (DSSC) where absorbed photons are used to generate electron–hole pairs.

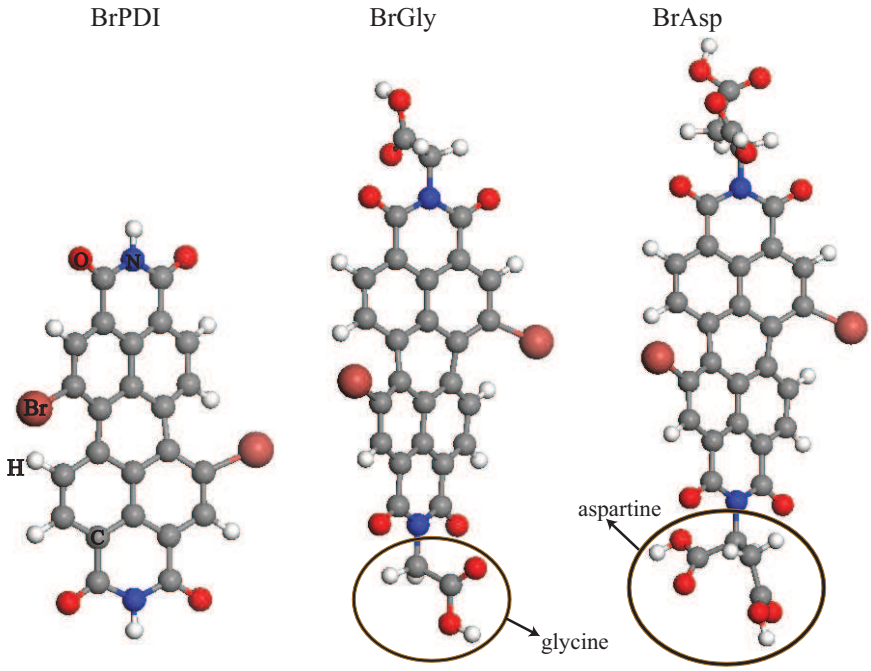

Figure 5.3: Calculated molecular structures of PDI–based dye molecules. Pink, white, gray, red and blue colors represent the Br, H, C, O and N atoms, respectively. Carboxyl groups (glycine and aspartine) are also shown.

The calculated HOMO-LUMO gap of these molecules are 2.39 (1.45), 2.38 (1.45) and 2.36 (1.44) eV for BrPDI, BrGly and BrAsp, respectively using time dependent density functional theory (TDDFT). Standard DFT gap values are give in parenthesis. According to DFT results, dyes exhibit slightly infrared characteristics. It is known that DFT fails to predict correct band gap of the semiconductors and insulators. Luminescence near the green region for these dyes have been obtained in an experiment [107]. Difference between DFT and TDDFT band gap values is about 0.9 eV. DOS of isolated dyes are presented in Figure 5.4. Br, O and C atoms contribute the HOMO level of dyes. The ground state of the PDI dyes extends through the perylene part including the p electrons of the halogen atom. LUMO consists of O, C and small Br contributions. The HOMO-LUMO

gap does not depend on the carboxylic acid groups but on the halogen atom. We have almost the same HOMO-LUMO gap for all PDI dyes. Figure 5.5 represents the partial charge density plots of HOMO and LUMO levels for all dyes.

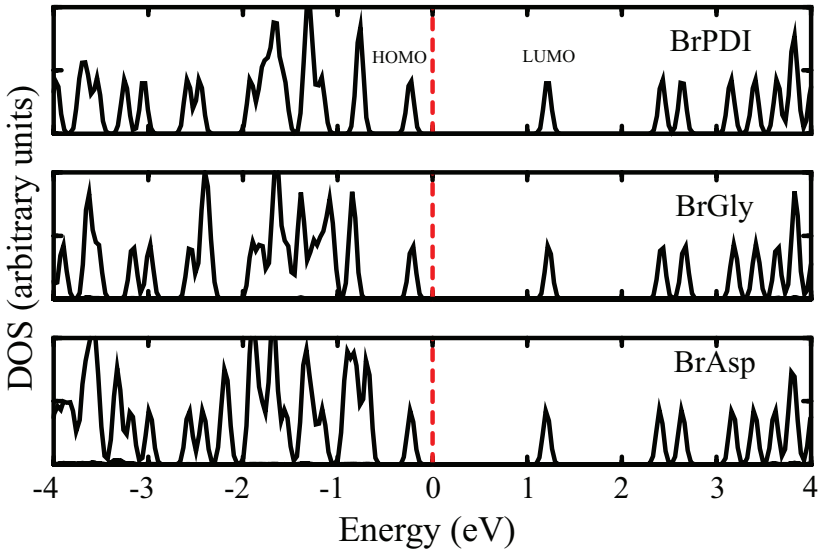

Figure 5.4: Density of states (DOS) of the free dyes. Fermi level is shown by dashed line.

It is noticed that carboxylic acid groups have no charge density distribution, either on the HOMO or on the LUMO levels for all dyes. The electrons seem to be localized around the center when the molecule is in its ground state more than the LUMO. When the molecule is excited to the LUMO, Br gives its HOMO charge to this charge–transfer state which extends toward the ligands. We notice that the main difference in the charge distributions is that, while the HOMO is aligned as if it is attracted by the two Br atoms, the LUMO looks like a flow of charge toward the tips where the carboxyl groups are bound. Detailed discussions about these dye molecules have been published elsewhere [108].

We have considered several adsorption configuration for each dye to find the most favorable binding mode. We have imposed certain criterion in construction of initial surface–dye structures in order to reduce computational costs.

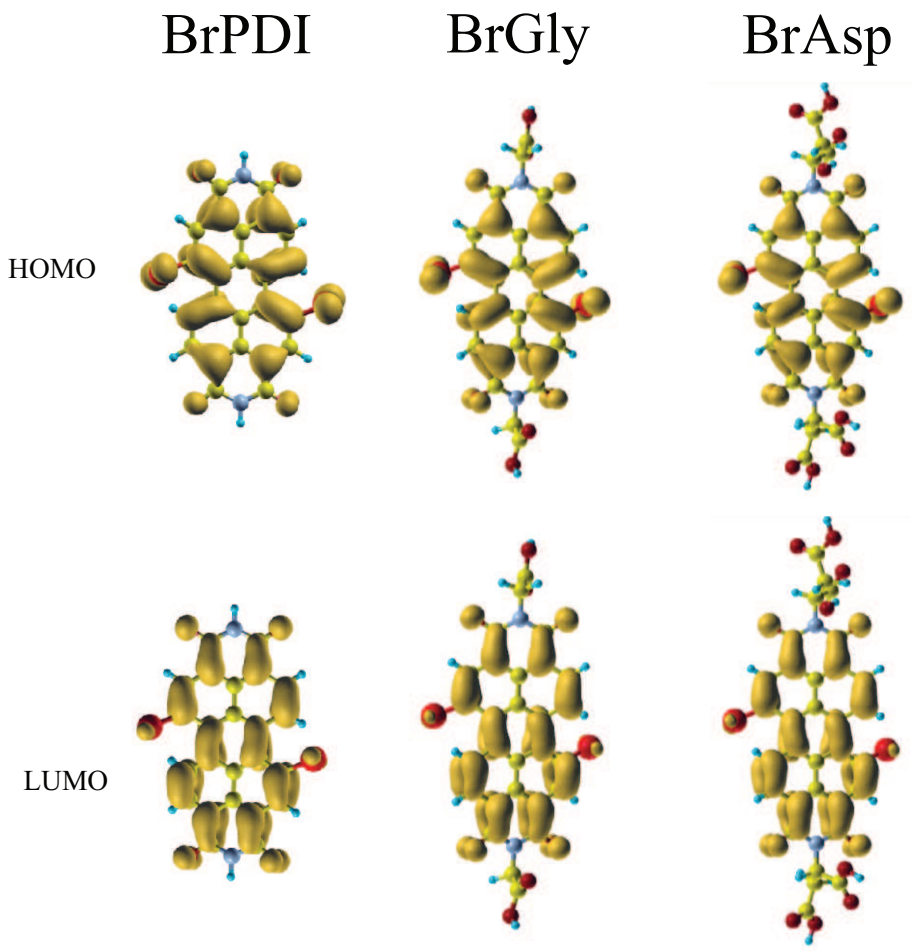

Figure 5.5: Calculated HOMO and LUMO charge density distributions of the (a) BrPDI, (b) BrGly and (c) BrAsp molecules. Upper and lower figures correspond to the partial charge density plots of HOMO and LUMO levels, respectively.

Ti–H, O–O and Br–Ti interactions have been avoided by using simple electrostatic arguments which state that the same charges repel each other. In Figure 5.6, we have presented the most energetic adsorption structures. Binding energy E_b of molecules has been calculated by the following expression, E_b=E_T[surface]+E_T[dye]-E_T[surface+dye] in terms of the total energy of optimized surface+dye system, isolated surface and dye molecule. We can deduce general behaviors about how molecule binds to surface. In all strong binding modes, dye molecules prefer to bind undercoordinated Ti atoms of surface through its O atoms. H atoms of the dye molecule bind to the bridge O atoms of the surface. Strong binding between dyes and surfaces is very crucial for the performance and production of DSSC.

5.2.3 BrPDI case

This dye molecule does not have any carboxyl groups. In initial geometry of UR–dye structure, molecule is almost parallel to surface. After the relaxation has been performed, two O atoms at each end bind to fivefold coordinated Ti atoms in the expense of induced stress on dye molecule and main contribution to E_b comes from these bonds. Due to interaction with H atoms, two bridge O atoms go upward and two surface Ti–O bridge bonds are broken. E_b of this absorption mode is 2.60 eV. When one side of dye does not bind to surface, E_b becomes 1.41 eV. Average distance between molecule O and surface Ti atom is about 2.0 Å. In RC case, molecule prefers to bind ridge atoms of the surface. Unlike Ti atoms on terrace region, Ti atoms on the ridge are fourfold coordinated. Therefore, ridge is more reactive than terrace region. For the water adsorption, it has been shown that molecular and dissociative adsorption occur on the terrace and ridge region, respectively [109]. E_b of the most energetic binding structure is 2.30 eV. Bond between the surface O1 and Ti2 atoms are broken upon adsorption of molecule and H atom of the dye binds to surface O1 atom. Unlike UR–BrPDI case, structure of the surface at the proximity of the dye are mainly disturbed in RC case.

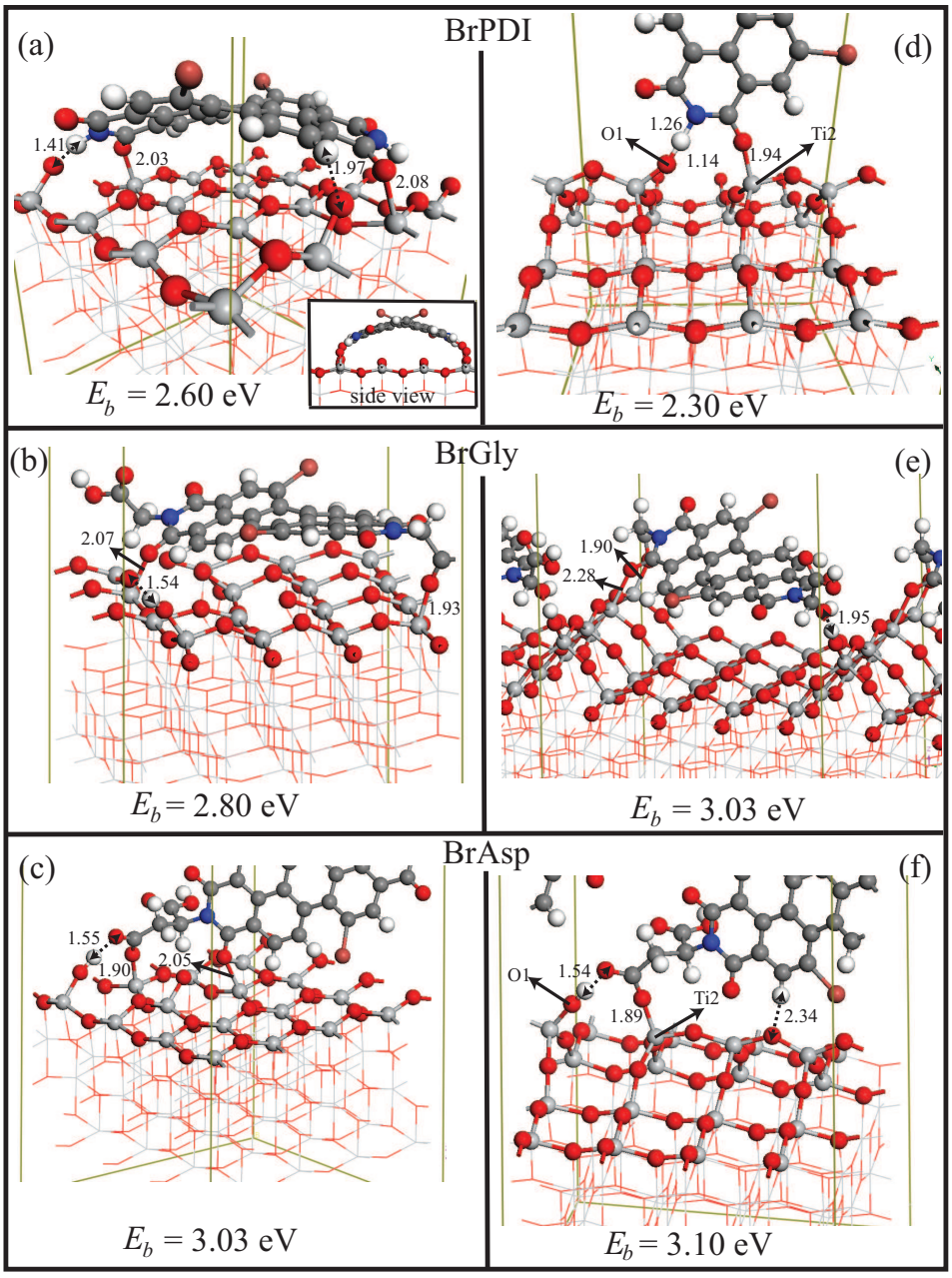

Figure 5.6: Fully optimized geometry of the most energetic adsorption modes of dye molecules on anatase TiO_2 (001). Side perspective structure viewed from [101] direction of UR–BrPDI case is shown in inset. Only the bonded part of the molecules are represented. Detail structure of the dyes are shown in Figure 5.3. Binding energies (E_b) and interatomic distance (in Å) between the selected atoms are also given. Discussions about the numbered atoms are in the text.

5.2.4 BrGly case

BrGly molecule has two glycine groups. The glycine ligand anchors BrGly to the titania as shown in Figure 5.6 (b) and (e). In the UR–BrGly structure, one of the ligand and perylene O atoms bind to surface Ti atoms. The remaining middle part of the dye is almost parallel to the surface. Other ligand does not bind to any surface atom. Average interatomic distance between the bonded surface Ti and dye O atoms is about 2 Å. This dye makes two contacts with the surface giving rise to increased interaction. Moreover, dye is dissociatively adsorbed on the UR surface. H atom of the bonded ligand part is captured by the surface bridge O atom. E_b of this adsorption mode is 2.80 eV which is greater than E_b of BrPDI case on the same surface. In the RC case, E_b of the dye on this surface increases significantly being the strongest chemisorption mode achieved for BrGly surface–dye systems. Resulting binding energy is 3.03 eV. This corresponds to a dissociative adsorption in which ligand O–H bond breaks. This hydrogen binds to the surface ridge O atom becoming separated from the glycine O atom by 1.95 Å. Both ends of the dye interact with the ridge part of the RC surface. Being more energetic than the molecular adsorption, this result suggests that better anchoring leads to relatively higher E_b and stability.

5.2.5 BrAsp case

This dye contains two aspartine molecules as carboxyl groups. In the structure of aspartine, two O atoms are only onefold coordinated. At least, one of these oxygens participates in all strong binding modes. BrAsp exhibits dissociative binding on both surfaces as shown in Figure 5.6 (c) and (f). One of the aspartine O–H bonds breaks and this H atom binds to surface O1 atom as in the case of RC–BrGly structure. The dye molecule sticks to UR surface Ti atoms through its aspartine oxygens giving a binding energy of 3.03 eV. In RC case, onefold coordinated O atom of the ligand part of the dye binds to fourfold coordinated

Ti atom which is in the ridge region on the surface. Existence of this catalytically active region, similar to RC–BrGly case, allows BrAsp to form strong chemical bonds with the RC surface leading to an E_b of 3.10 eV. We also notice that the coordination numbers of ligand O atoms and surface Ti atoms influence the strength of the binding.

We did also study the effects of coverage on E_b for BrPDI adsorption on both (2×4) UR and RC surfaces. Because of the size of these slabs, only some adsorption modes have been investigated. High coverage reduces the E_b significantly. When BrPDI binds to diagonal Ti atoms through its two O atoms, E_b is 1.60 eV on (4×4) cell. However, on (2×4) slab, E_b becomes 0.87 eV. Stability of (001) anatase can be enhanced not only with reconstruction but also via adsorption of water. Thus, we have studied the interaction of BrPDI with these surfaces where water has been adsorbed dissociatively. In RC surface, water adsorption occurs only at ridge region. Direct interaction between BrPDI and the host surface is prevented by the water. In addition to this, reactivity of surface reduces due to the adsorption of water. Therefore, E_b drops compared to the clean surface and binding mainly comes from the interaction between surface hydroxyl groups and the dye molecule.

In DSSC devices, optical properties of the systems are determined by the dye molecules. To produce an efficient and stable solar cell, dye molecules must be strongly bound to the underlying semiconductor material and absorb the large part of the solar light. Our dyes are stable at their ground state and form strong chemisorption bonds with the TiO_2 surface. Except for the UR–BrPDI case, structure of the studied dye molecules are slightly changed upon adsorption only at the proximity of binding region. We have further investigated the electronic properties of fully relaxed surface–dye combined system. In DSSC, dye is excited by photons and as a result electron–hole pairs are generated by this illumination. Generated electrons in excited states of dye must be injected to conduction band of semiconductor and this injection has to be very fast to prevent the reduction of the oxidized dye. Therefore, position of HOMO-LUMO levels of the dyes with respect to valance band (VB) and conduction band (CB) edges of TiO_2 is very crucial. For an efficient solar cell, HOMO level produces occupied levels inside the

gap region and LUMO is well localized across CB of the slab. Figure 5.7 shows the partial density of states (PDOS) of the surface–dye systems for the most energetic adsorption modes. We notice that adsorbed BrGly on both surfaces and BrAsp on the RC surface induce occupied states inside the band gap of TiO_2. Moreover, LUMO levels of these molecules fall inside the CB of the slab.

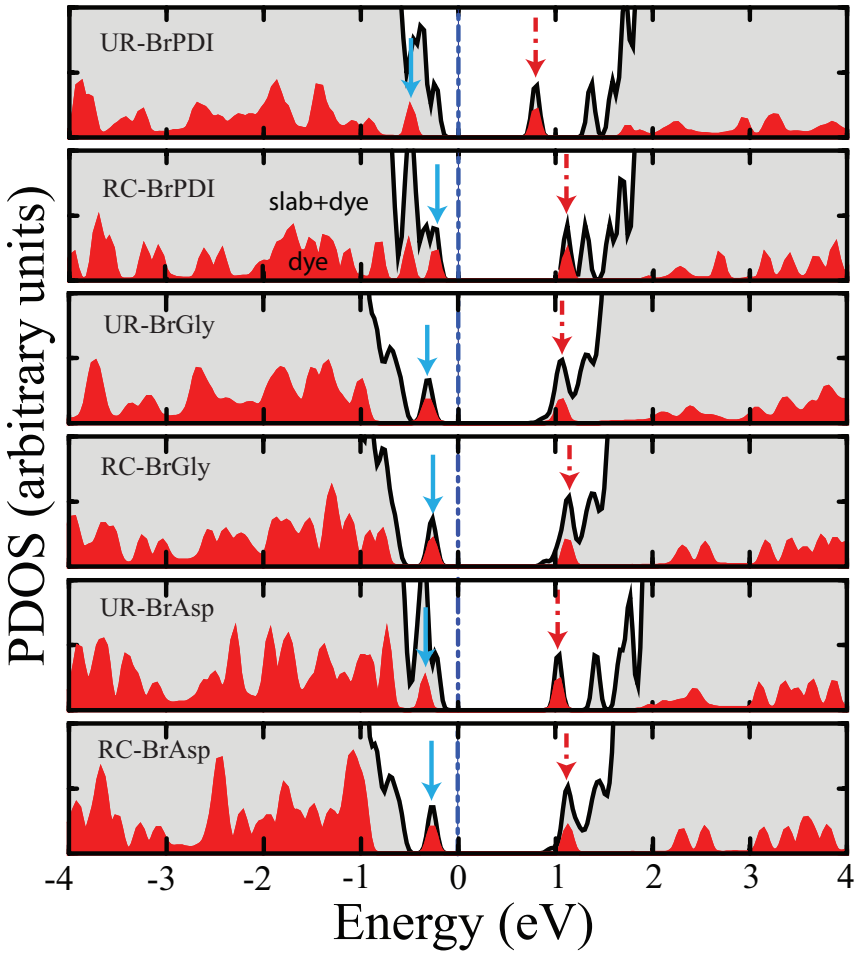

Figure 5.7: Projected density of states (PDOS) for adsorbed dyes. DOS of total system and absorbed dye are represented by gray and red colors, respectively. Fermi level is shown by the violet dotted–dashed line. Cyan and dotted-dashed red arrows mark the position of HOMO and LUMO levels of absorbed dye molecules. We have used gaussian function with a smearing parameter of 0.05 eV and $2 \times 2 \times 1$ k–points mesh in PDOS calculations.

In RC–BrPDI, HOMO and LUMO levels of the dyes appear at the edges of

VB and CB of the metal oxide, respectively. As opposed to the UR–BrPDI case, the adsorption of BrPDI induce significant band gap narrowing. Due to coupling between the electronic states of the dyes and anatase surfaces, there are both broadening and shift to higher energies in the energy levels of the dye molecules. The effects of these strong interactions are more pronounced in the occupied levels of the dyes. Yet, HOMO-LUMO gaps do not change significantly. Therefore, these molecules do not lose their optical properties which are vital for DSSC applications.

Chapter 6

Adsorption of BrPDI, BrGly, and BrAsp on rutile TiO_2 (110) surface for the dye-sensitized solar cell applications

In this chapter, we have investigated the interaction between the PDI–based dyes and defect free rutile (110) surface.

6.1 Results and Discussions

6.1.1 Rutile (110) surface

The rutile (110) surface (see Figure 6.1) exposes two kinds of titanium and oxygen atoms. Along the $[1\bar{1}0]$ direction, fivefold (Ti2) and sixfold (Ti3) titanium atoms alternate. Similarly, twofold bridging oxygen atoms (O1) as well as threefold oxygen atoms (O4) are present. (110) surface is the most stable surface among rutile surfaces. It is often considered as a model metal oxide surface for

both extensive experimental and theoretical studies [1, 3]. According to Wulff Construction, rutile (110) surface forms 56% of the total exposed surface of the rutile crystal.

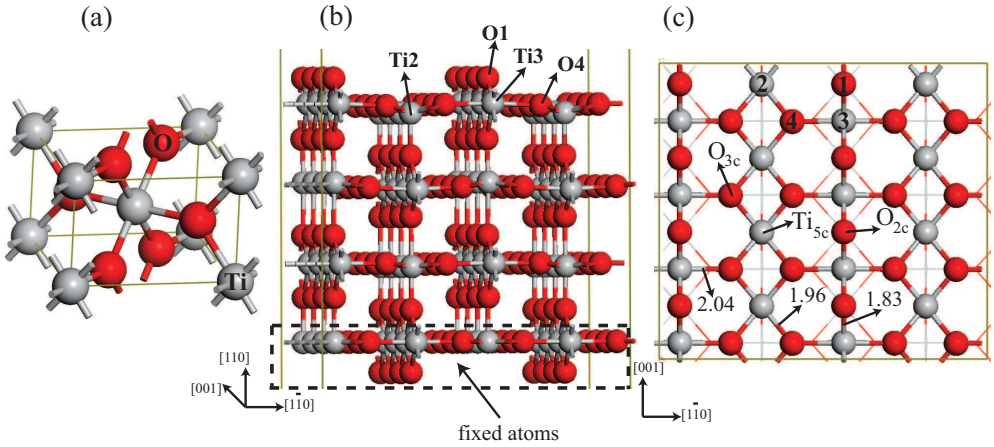

Figure 6.1: (a) Bulk rutile, (b) side and (c) top views of the relaxed 4×2 defect free rutile (110) surface. The coordination of some of the atoms is shown. Discussion about numbered atoms is in the text. Interatomic distance (in Å) between some of the atoms is also depicted.

The position of VB and CB band edges of the surface with respect to HOMO and LUMO levels of the adsorbed dye molecules is the key point for the DSSC applications. The rutile (110) surface has been modelled by both three and four layers slabs in order to examine effects of thickness on binding of dye molecules on titania surface. Three layers slab has been mainly used for test purposes. Depending on the adsorption geometry, 4×2, 4×3 or 6×2 unit cells of three and four layers slabs have been constructed. As in the case of dye–anatase system, certain criteria for the choice of supercell dimensions have been imposed. First of all, these supercells must be large enough to give possibility to search different adsorption geometries and to prevent the interaction of the dye molecules with their periodic images because of periodic boundary conditions. Secondly, they must be thick enough to reasonably reproduce most of the TiO_2 bulk properties. For the rutile (110) surface, an appropriate choice of the number of the fixed atoms or layers is crucial to obtain realistic results [110].

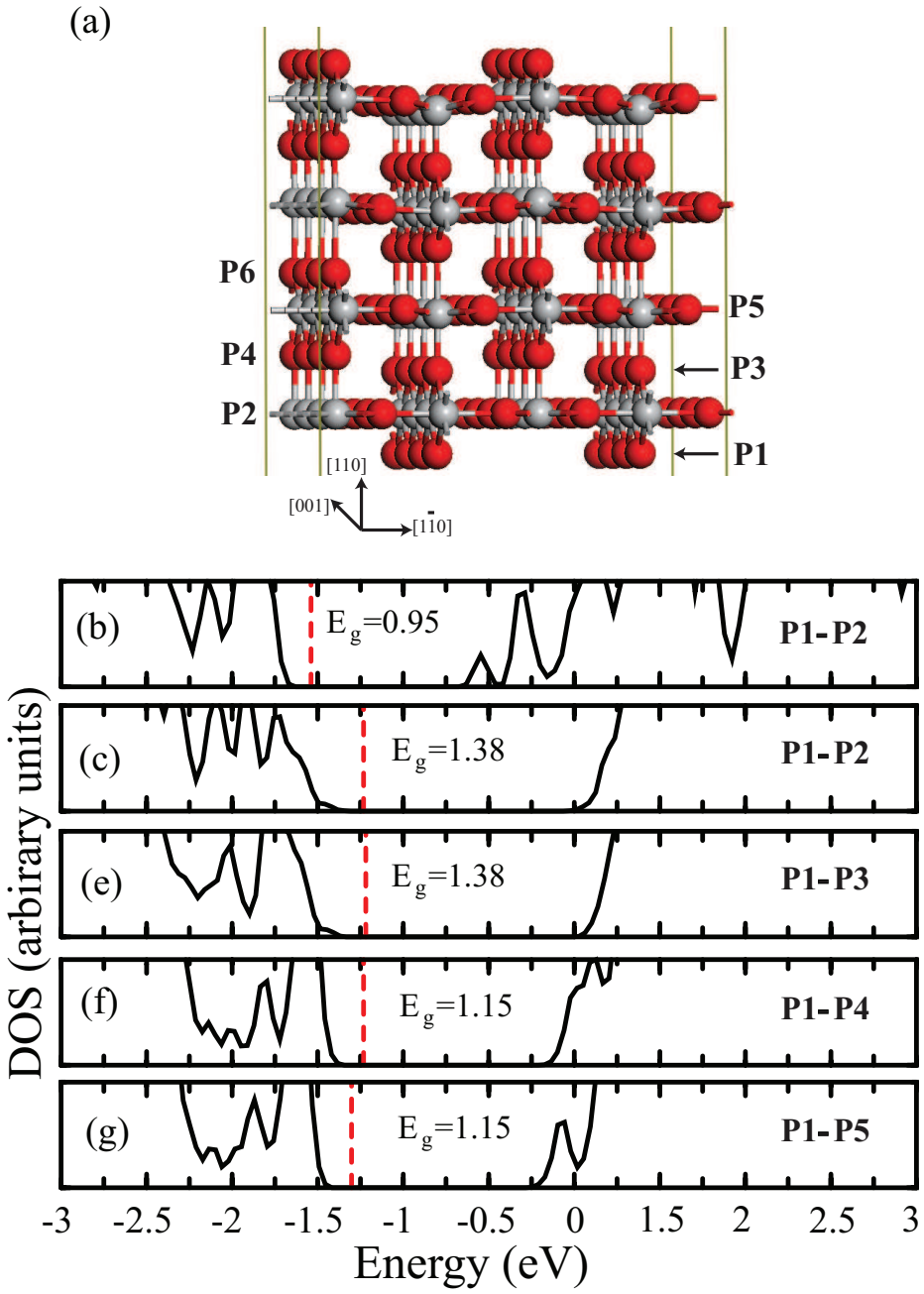

Figure 6.2: (a) Description of the different slab models used in calculations. Atoms residing on the atomic planes, namely P1, P2, P3, P4, P5 and P6, are not allowed to relax during the calculations depending on the slab model. These fixed atoms are kept in their bulk truncated positions. (b) Total density of states of each slab model: (b) three layers slab and (c–g) four layers slab. P1–P5 means that P1, P2, P3, P4 and P5 planes are frozen. Red dashed lines mark the Fermi level.

As a result, different four layers slab models having different number of fixed layers or atoms have been examined in order to figure out whether electronic properties of slab–adsorbed dye combined system change or not. Two bottom layers are decomposed into six atomic planes. Description of these planes is depicted in Figure 6.2 (a). We have tested the interaction between dye and rutile surface as increasing number of the fixed atoms or layers. In all surface modelled by three layers slab–dye calculations, atoms residing in P1–P2 planes of the slab have been fixed to their bulk truncated positions allowing all others to relax. The number of layers composed of the slab and the number of fixed atomic planes influence position of atomic energy levels and relaxation of free atoms. Total density of states of rutile slabs possessing different number of fixed layers for three layers and four layers slabs are shown in Figure 6.2. It is noticed that E_g of three layers slab is smaller than E_g of four layers slabs. Energy gap E_g is 0.95 and 1.38 eV for three and four layers slabs (in both cases P1 and P2 atomic planes do not move), respectively. E_g is 1.15 eV for the four layers slab which has five fixed atomic planes, namely P1–P5. VB and CB edges shift to higher energies with respect to three layers slab when four layers slab has been used. According to our tests, four layers slab is more convenient than three layers slab to get reliable results. It is obvious that properties of a slab converge to real surface properties as the slab thickness grows.

We have again considered perylenediimide (PDI)–based dye compounds. The detail discussions for these molecules have been presented in Chapter 5. Several dye–slab initial structures for all dye molecules have been examined in order to find the most energetic and stable adsorption mode. Two different slab thicknesses have been used in calculations. Methods used in calculations have been described in Chapter 5.

6.1.2 BrPDI case

Surface area in three and four layers slabs are different. Due to large size of the dye, we have constructed 6 × 2 surface (2 and 6 unit cells along the [001] and [1$\bar{1}$0] direction, respectively) in three layers slab. 4 × 2 surface has been used in four layers slab. Unless it is explicitly mentioned, P1 and P2 atomic layers fixed slab calculations will be presented for the BrPDI molecule adsorption. It is obvious that four layers slab has more free atoms than those of the three layers slab. Figure 6.3 shows the adsorption of BrPDI dye on 4 × 2 four layers surface.

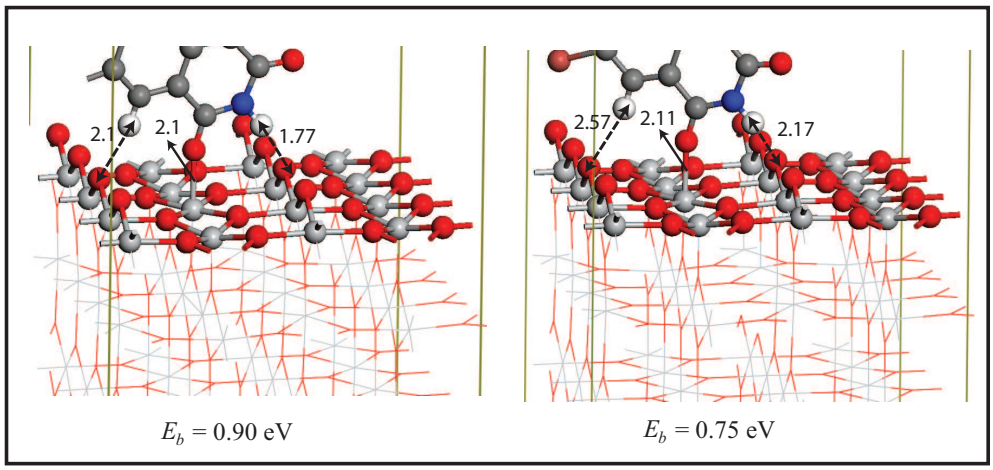

Figure 6.3: Fully optimized geometry of the two most energetic adsorption modes of BrPDI dye molecule on 4×2 four layers rutile TiO_2 (110) surface. In this surface case, P1 and P2 atomic layers has been fixed during the structural optimization. Binding energy (E_b) is given for each adsorption case. Interatomic distance (in Å) between some of the atoms is also depicted.

This surface is large enough to study particular adsorption modes at which perylene part of the dye is perpendicular to the surface. For the most energetic adsorption case, O atom of the dye binds to a surface fivefold coordinated Ti atom with a interatomic distance of 2.1 Å. Moreover, two H atoms of dye interact with two twofold coordinated bridge O atoms. The interatomic distances in these H-O bonds are 2.1 and 1.77 Å, respectively. E_b of this most stable adsorption mode is 0.90 eV. In previous chapter, the calculated E_b's ranges from 1.6 to 2.6 eV for

BrPDI dye molecule. This result suggests that both UR and RC anatase (001) surfaces are more reactive than unreconstructed defect free rutile (110) surface. Furthermore, molecular adsorption of BrPDI dye on four layers 4×2 rutile surface has been observed. For the second most energetic adsorption case, interaction between H atoms of dye and surface bridge O atoms is weakening because of increasing the interatomic distance among these atoms. Dye binds to surface fivefold coordinated Ti atom through its O atom. E_b of this adsorption mode is 0.75 eV. In a chemical bond, E_b is larger than 1 eV. Therefore, a moderate chemical interaction exists between the rutile surface and dye molecule.

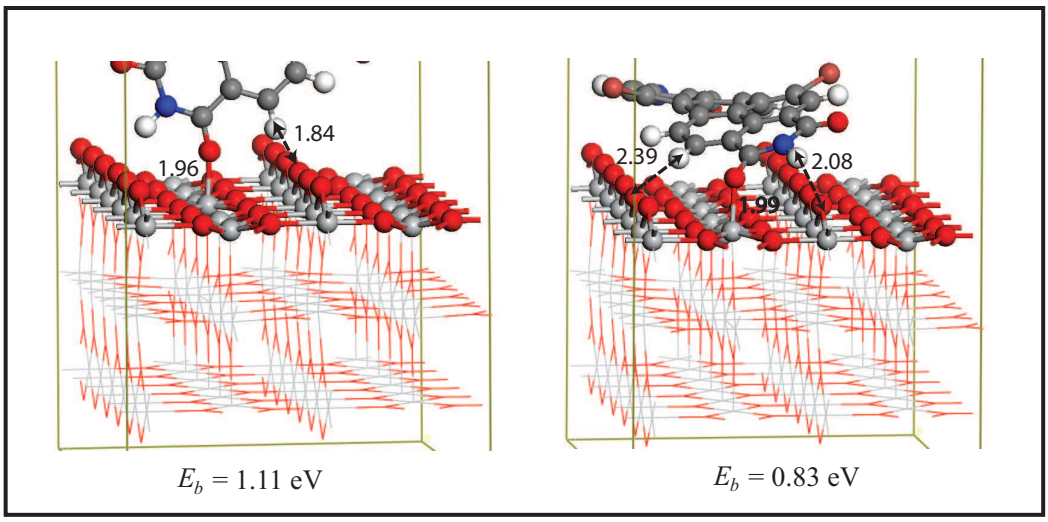

Figure 6.4: Fully optimized geometry of the two most energetic adsorption modes of BrPDI dye molecule on 6×2 three layers rutile TiO_2 (110) surface. P1 and P2 atomic layers has been fixed during the structural optimization. Binding energy (E_b) is given for each adsorption case. Interatomic distance (in Å) between some of the atoms is shown.

When perylene part of the dye is parallel to the surface, 4×2 surface cell is not suitable to study such adsorption structure. Hence, we have constructed 6×2 surface cell. In order to reduce computational costs and examine the effects of the slab thickness on the interaction between the surface and BrPDI dye, 6×2 slab consists of three layers. Again, P1 and P2 layers have been fixed during the calculations. Three main configurations at which dye is parallel to the surface

can be considered. In the first one, longer part of the dye is along the [001] direction of the surface. We have rotated dye by 90° to obtain the second one. In this case, longer part of the dye is oriented along the $[1\bar{1}0]$ direction. The last configuration is the mixing of the first two cases. Dye is oriented along the diagonal of the surface. We have studied three initial structures. One of them is the most energetic adsorption structure of 4×2 four layers slab case. It is possible to construct a large number of initial geometries. However, we can reduce the number of the possibilities by using certain basic physics rules. We know that O atoms of surface are negatively charged. Ti atoms of surface and H atoms of molecule do not prefer to bind to each other. By using these simple electrostatic arguments, we have formed two initial structure in which perylene part of the BrPDI dye molecule is parallel to the surface. Figure 6.4 displays the structure and E_b of the two most energetic adsorption modes. The calculated lowest lying structure in both slab thicknesses is the same. E_b in three layers slab case is 1.11 eV and this binding energy is greater than that of four layers slab case. We have also considered the adsorption of BrPDI on the more than two layers fixed four layers slab. In this case, P1–P5 atomic layers have not been allowed to move. We have only constructed one initial structure which is the most energetic structure of the previously explained slab models for BrPDI adsorption. Figure 6.5 (a) shows the optimized structure of this adsorption mode. The calculated E_b is 1.04 eV.

We have used the BrPDI–surface system as a test system to check several parameters such as slab thickness. Unless it is explicitly mentioned, P1–P5 layers fixed four layers slab calculations will be presented for the rest of this chapter.

6.1.3 BrGly case

BrGly contains two glycine as carboxyl group. The glycine ligand and one of the perylene O atom anchor BrGly to the rutile (110) surface. Figure 6.5 (b) presents the optimized adsorption geometry of BrGly on the surface for the most energetic structure.

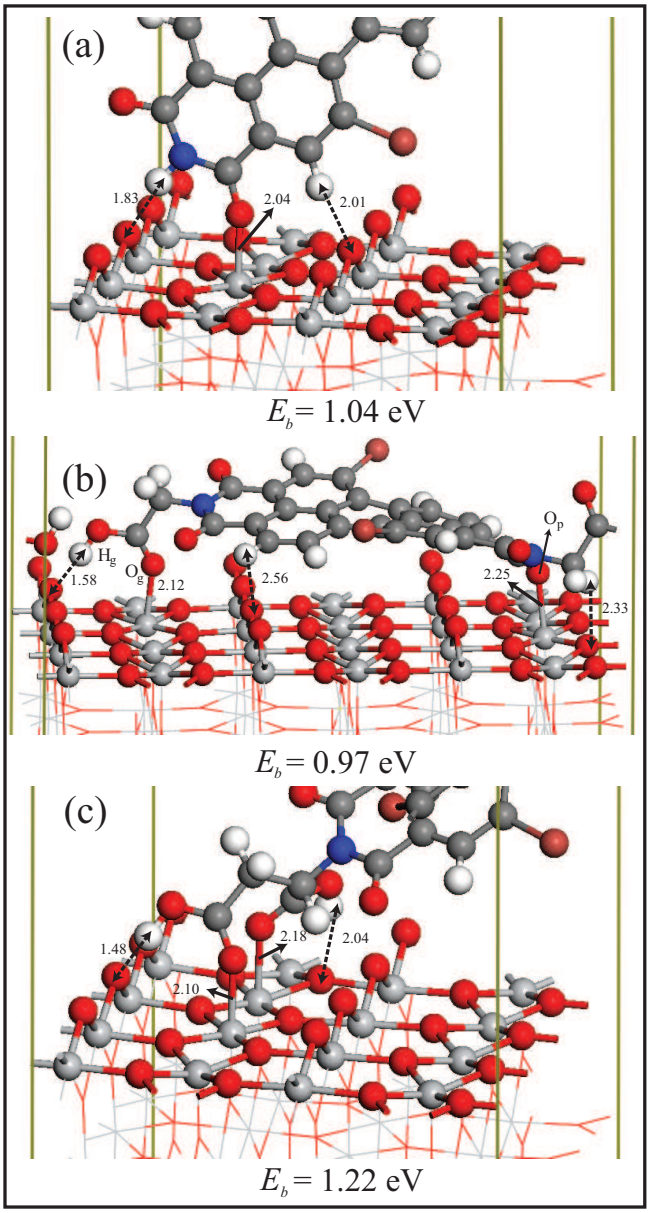

Figure 6.5: Fully optimized geometry of the most energetic adsorption modes of (a) BrPDI, (b) BrGly and (c) BrAsp dye molecules on 4×2 four layers rutile TiO_2 (110) surface which has fixed atomic layers of P1–P5. Binding energy (E_b) is given for each adsorption case. Interatomic distance (in Å) between some of the atoms is also displayed.

Because of the position of the glycine groups with respect to middle part of the dye, perylene part is parallel to the surface in the most stable adsorption structure. Therefore, 4×3 slab has been used to simulate this adsorption mode. Dye makes two contact with titania surface. Anchor group O (O_g) atom interacts more strongly with the surface Ti atoms compared to perylene O (O_p) atom. Interatomic distance between surface Ti and O_g (O_p) atom is 2.12 (2.25) Å. H atoms at the edge of perylene core and glycine H (H_g) atoms interact with the surface bridge O atoms. Distance between the H_g and its nearest bridge surface O is 1.58 Å. Other ligand does not participate to the binding. Dye is molecularly adsorbed by the surface with a E_b of 0.97 eV.

6.1.4 BrAsp case

In this dye, anchor group is aspartine. BrAsp sticks to surface through its one of the carboxylic group. Two O atoms of anchor group bind to fivefold coordinated Ti atoms with a average interatomic distance of 2.14 Å. Moreover, H atoms of aspartine interact with bridge and basal O atoms giving rise to increased interaction between dye and surface. E_b of the most stable adsorption mode is 1.22 eV and this corresponding to a molecular adsorption.

E_b of BrGly is smaller than that of BrPDI and BrAsp dyes. In BrGly case, perylene skeleton is parallel to the surface and this situation enhances repulsive interaction between the surface and dye. In dye–surface systems, binding mainly results from the Ti–O interaction. BrGly and BrAsp dyes are dissociatively adsorbed on the three layers slab. O–H bond in ligand part breaks and H atom of glycine or aspartine group binds to the surface bridge O atom. All dyes bind more strongly to the three layers slab. For the most stable adsorption structure of BrAsp on three layers slab, E_b is 1.76 eV. We have shown that molecular adsorption of dyes is favorable on the at least four layers thick rutile surface.

Figure 6.6 shows the PDOS of the lowest lying adsorption structures of all

dyes. It is noticed that adsorbed dyes induce occupied electronic states inside the TiO_2 band gap. HOMO level of dye is close to VB edge of the slab. Furthermore, LUMO of the dyes is within the CB of the surface. For efficient charge injection from excited dye to CB of the surface, LUMO must be well localized within the CB. For BrPDI–surface case, LUMO of the adsorbed dye is more close to CB edge compared to both BrGly and BrAsp–surface systems. Carboxyl groups do not contribute to both HOMO and LUMO levels of the free dyes.

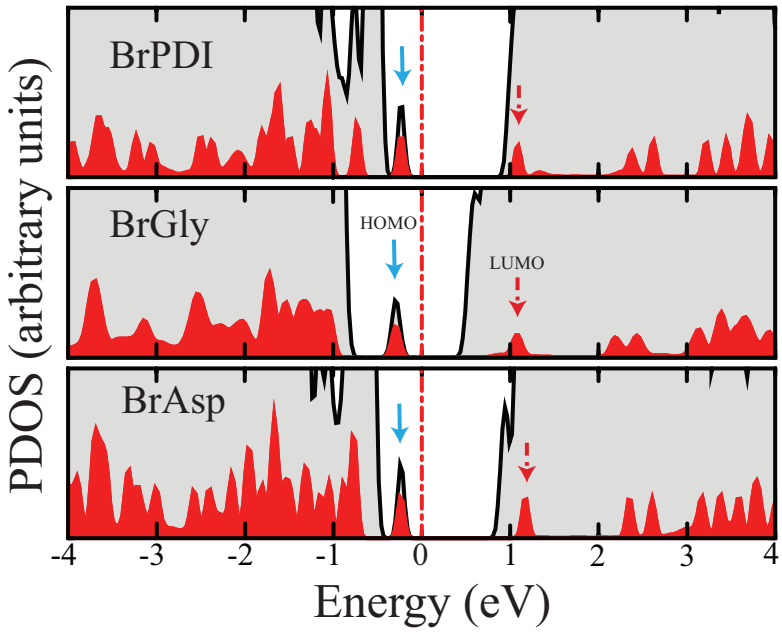

Figure 6.6: Projected density of states (PDOS) of (a) BrPDI, (b) BrGly and (c) BrAsp dye molecules on 4×2 four layers rutile TiO_2 (110) surface which has fixed atomic layers of P1–P5. DOS of total system and adsorbed dye are represented by gray and red colors, respectively. Fermi level is shown by the red dotted-dashed line. Cyan and dotted–dashed red arrows mark the position of HOMO and LUMO levels of adsorbed dye molecules. We have used gaussian function with a smearing parameter of 0.05 eV and $3 \times 2 \times 1$ k–points mesh in PDOS calculations.

Therefore, coupling strength between the perylene core and TiO_2 influences the performance of the DSSC. For the BrPDI and BrGly adsorption, there is a significant coupling between these dyes and underlying surface. As a result, it is

expected that electron injection process from the BrPDI and BrGly excited singlet state to CB of the TiO_2 is faster than those of BrAsp. Slow electron injection rate means low power conversion efficiency in the DSSC devices.

6.1.5 BrPDI dye on partially reduced rutile (110) surface

Oxygen vacancy is one of the main point defect on rutile (110) surface. It influences significantly the physical and chemical properties of metal oxide surfaces [1] and can act preferential adsorption site for atoms or molecules. Formation of oxygen vacancy at the bridge site of the surface gives rise to two excess electrons. Ti^{+3} ions and localized band gap states form upon reduction of the surface. These gap states are mainly Ti $3d$ character [111, 112]. There is an disagreement among the first principles calculations about distribution of these excess charges. Different exchange and correlation (XC) potentials give completely conflicting results. According to standard DFT used LDA and GGA, excess charges populate the bottom of the conduction band, which gives the delocalization of these excess charges over several surface and subsurface layers [113, 114]. However, hybrid functionals such as B3LYP predict localization of defect charge over two specific surface Ti sites [115]. It is known that DFT fails to describe strongly correlated systems. DFT+U approach provides a reasonable description of the electronic and geometric structure of the reduced surface, which is consistent with some experiments. However, in a recent experiment, it has been shown that the defect charge is distributed over several surface and subsurface Ti sites by using the resonant photoelectron diffraction technique [116]. These results are consistent with DFT calculations which have predicted a delocalization of defect charge. DFT theory based on Kohn–Sham orbitals predicts the wrong band gap. However, it generally predicts adsorbate binding energy correctly. In this work, we have also examined interaction between the BrPDI and partially reduced 4×2 rutile (110) surface possessing single O vacancy. We have tried to obtain a qualitative results for binding of dye on the reduced surface. Single O vacancy has been obtained by removing of a bridge O atom from 4×2 surface. Resulting partially reduced surface has ferromagnetic ground state. Induced magnetic moment upon

formation of single O vacancy is 1.77 μ_B.

In contrast to this large magnetic moment, energy difference between the ferromagnetic and non–magnetic solutions is 20 meV. As a result of the O vacancy, structure of surface at the vicinity of vacancy is disturbed. On the reduced surfaces, vacancies are very reactive sites. In construction of initial starting structure for BrPDI–surface system, this argument has been used. During the calculations, spin polarization has been ignored. For the most stable adsorption mode, O atom of BrPDI prefers to locate at the position of the vacancy, see Figure 6.7 (a). Two H atoms of dye interact with the bridge and basal O atoms. E_b of this adsorption mode is 1.22 eV.

6.1.6 BrPDI dye on platinized rutile (110) surface

Photo reduction of CO_2 under UV and visible light have been tested over the dye (brominated PDI derivatives: BrGly and BrAsp) sensitized Pt promoted TiO_2 thin and thick films by Ozcan *et al* [117]. Pure and Pt containing TiO_2 films have been inactive under visible light. These films have activated by adsorbing the organic dye sensitizers. Therefore, we have also studied the interaction of BrPDI with platinized rutile surface as a prototype of dye–Pt–surface system. For this surface, three cases have been considered. For the first one, single Pt atom has been adsorbed by the surface at the vacancy site. Three atoms cluster has been formed at the vicinity of the vacancy site for the second case. Finally, five atoms Pt cluster has been grown. Ground state structures of Pt_n clusters (n=1, 3 and 5) adsorbed on the partially reduced 4×2 rutile (110) surface are shown in Figure 6.7. It is noticed that interatomic distance in Pt–Ti and Pt–Pt bonds increases as the coordination number of Pt atoms increases. Binding energy per Pt atom (E_b) on partially reduced surface has been calculated as follows: $E_b = (E[\text{slab}]+nE[\text{Pt}]\text{-}E[\text{slab}+\text{Pt}_n])/n$. In this formula, E[slab], E[Pt], E[slab+Pt_n] are the total energy of partially reduced slab possessing single O vacancy, free

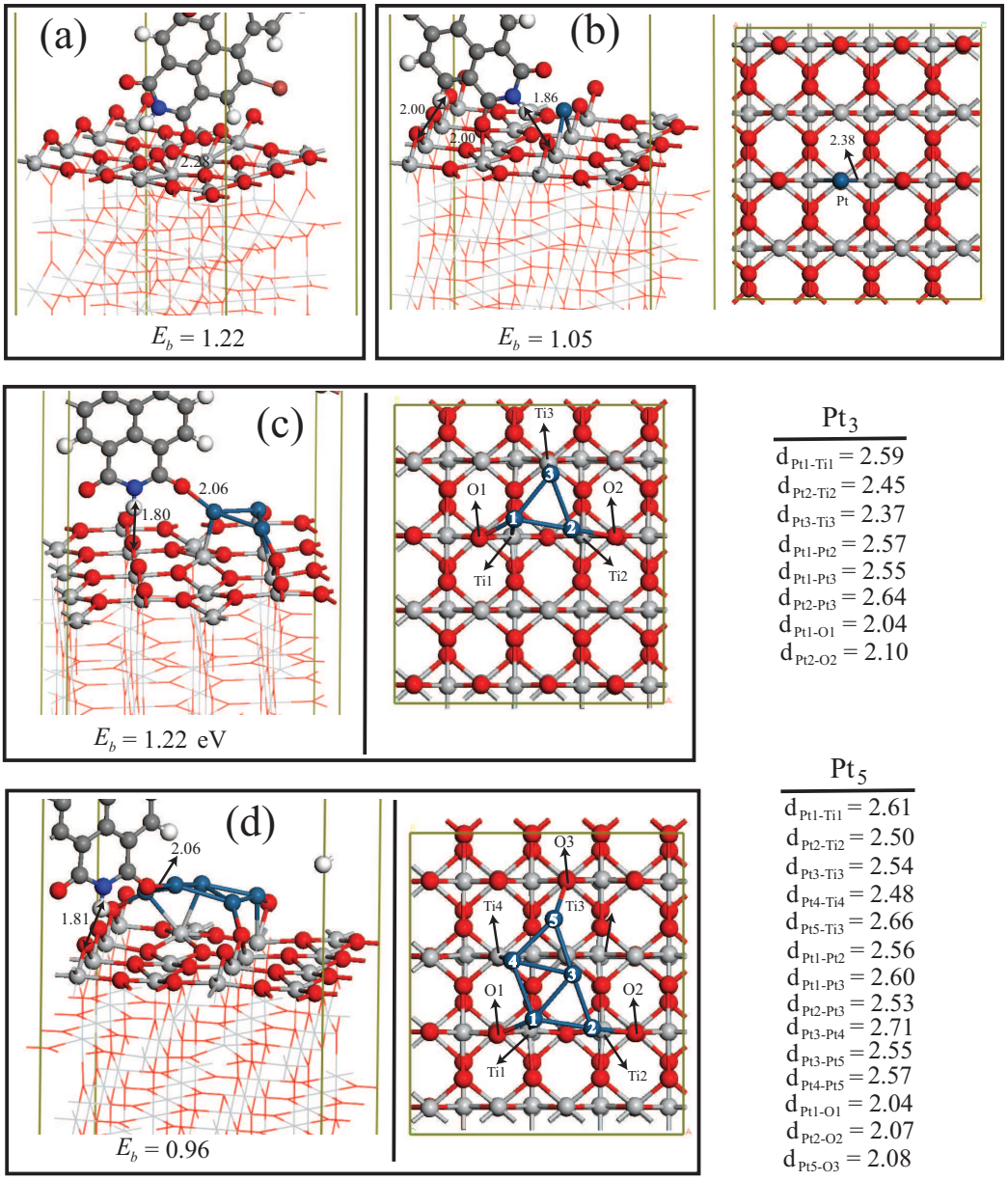

Figure 6.7: Fully optimized geometry of the most stable adsorption modes of BrPDI on (a) partially reduced, (b) Pt–surface, (c) Pt_3–surface and (d) Pt_5–surface. Top view of the ground state structure of the Pt monomer, Pt_3, and Pt_5 clusters adsorbed on partially reduced 4×2 rutile (110) surface is also represented. Binding energy (E_b) is given for each adsorption case in eV. Interatomic distance (in Å) between some of the atoms is shown.

Pt atom and fully relaxed slab+Pt system. Here, n represents the number of Pt atom adsorbed on the surface. E_b of monomer, trimer and Pt_5 cluster is 3.15, 3.66 and 3.83 eV, respectively. The ground state structure of the adsorbed Pt_3 cluster has triangular geometry and two Pt atoms have been adsorbed at vacancy site of the surface. Adsorbed Pt_5 cluster has planar ground state structure on the reduced surface. Pt_3 and Pt_5 clusters have been constructed by repeatedly adding of single Pt atom to smaller cluster and allowing the structure to relax again. We have performed a systematic search to find the lowest energy structure of these small clusters.

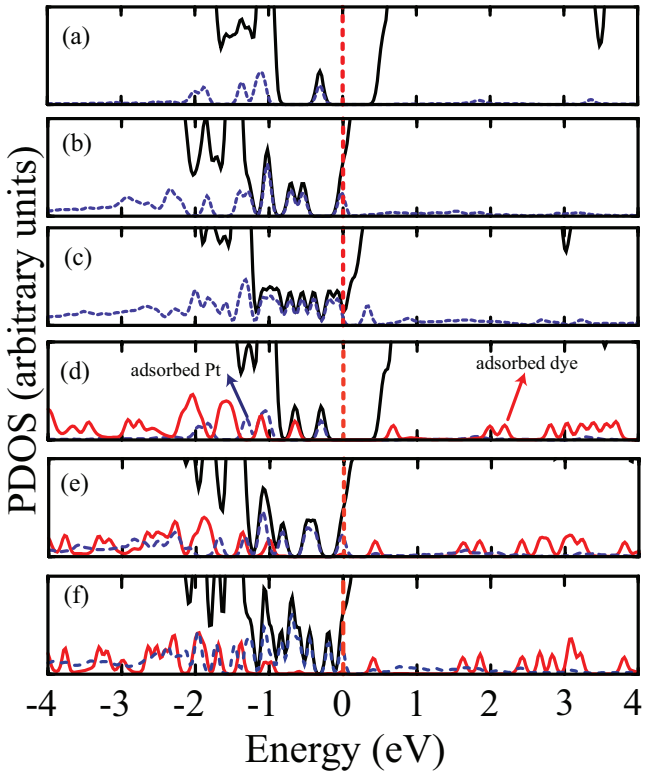

Figure 6.8: Projected density of states (PDOS) of (a) Pt monomer, (b) Pt_3, and (c) Pt_5 clusters adsorbed on the partially reduced 4×2 rutile (110) surface. PDOS of BrPDI adsorbed on (d) Pt–surface, (e) Pt_3–surface, and (f) Pt_5–surface. DOS of total system, adsorbed dye and Pt atoms are represented by black, red and violet colors, respectively. Fermi level is shown by the red dotted–dashed line. We have used gaussian function with a smearing parameter of 0.05 eV and $3 \times 2 \times 1$ k–points mesh in PDOS calculations.

Inclusion of spin polarization effects on calculations has been tested and found them to be negligible. Figure 6.8 shows the partial density of states of Pt_n–surface system before and after the interaction with BrPDI. The analysis of the density of states reveals that Pt_n–surface system becomes metallic for n=3 and 5. Metal–induced states in the band gap of surface for Pt monomer case are observed. Because of these states, adsorption of a single Pt atom is lower the optical threshold of the rutile (110) surface. Figure 6.7 shows the optimized structure of BrPDI adsorbed on platinized rutile (110) surface (Pt_n–surface, where n=1, 3 and 5). For the interaction between dye and Pt_1–surface system, the most energetic adsorption site is the same as adsorption of BrPDI on the defect free rutile surface. Dye molecule does not interact with the previously adsorbed Pt atom. Calculated E_b is 1.05 eV. In contrast to Pt_1–surface system, adsorbed Pt clusters contribute to the binding of dye on the surface in the case of Pt_3 and Pt_5 clusters. In both cluster cases, O atom of the BrPDI binds to a particular Pt atom of the clusters with a average interatomic distance of 2.04 Å. In Pt–oxides, Pt–O bond length is about 2.0 Å. In addition to Pt–O bond, H atom of the dye interact with a 2–fold coordinated bridge O atom for both cluster case with a interatomic distance of 1.80 Å. We have also calculated the binding energy of BrPDI on the Pt_n–surface, which are 1.22 for $n = 3$ and 0.96 eV for $n = 5$ cluster. For all Pt_n (n=1, 3 and 5) cases, dye gives a gap localized occupied state (HOMO level of the adsorbed dye). Moreover, LUMO level is well localized with in the CB of the surface. Unlike optimized BrPDI–Pt_1–surface system, it is hard to inject excited electron of the dye into the CB of the underlying surface in the case of Pt_3 and Pt_5. In these cluster cases, dye interacts with surface through its H atom which has no contribution to the formation of LUMO of the dye. The generated charge eventuality transfers to the Pt_3 or Pt_5 clusters. In dye–Pt_n–surface system, first dye is excited by the visible light. Generated charge may be transfer to Pt clusters by two way: (1) Dye→surface→Pt_n and (2) Dye→Pt_n. In the first case, we have multiple charge transfer mechanism which can be observed in the case of dye–Pt_1–surface. When the charge reaches the Pt cluster, it can be used in catalytic process, which takes place on the cluster. In this way, visible light photocatalysis is obtained by using dyes as a light harvesting molecules. Our dye–Pt cluster–surface is the simplest system because our clusters are so small. However, this

work provides a fundamental understanding for photocatalysis applications of dye–Pt promoted titania surfaces.

Chapter 7

Pt AND BIMETALLIC PtAu CLUSTERS ON RUTILE (110) SURFACE

In this chapter, growth, electronic properties and structure of small Pt_n (n=1-8) and bimetallic Pt_2Au_m (m=1–5) clusters adsorbed on the partially reduced rutile (110) TiO_2 surface have been examined.

7.1 Results and Discussions

7.1.1 Method

We have performed first-principles plane wave calculations [21, 39] within density functional theory (DFT) [30] using projected augmented–wave (PAW) potentials [36]. The exchange–correlation contributions have been treated using generalized gradient approximation (GGA) with PW91 [32] formulation. The vacuum region between the periodic images has been taken at least 8 Å. For Brillouin zone integrations, in the self-consistent potential and total energy calculations, Γ point

has been used. A plane–wave basis set with kinetic energy cutoff of 500 eV has been taken. For the density of states calculations (DOS), a finer k–mesh has been used. For Pt and Au pseudopotentials, s^1p^9 and s^1d^{10} electronic configurations have been used, respectively.

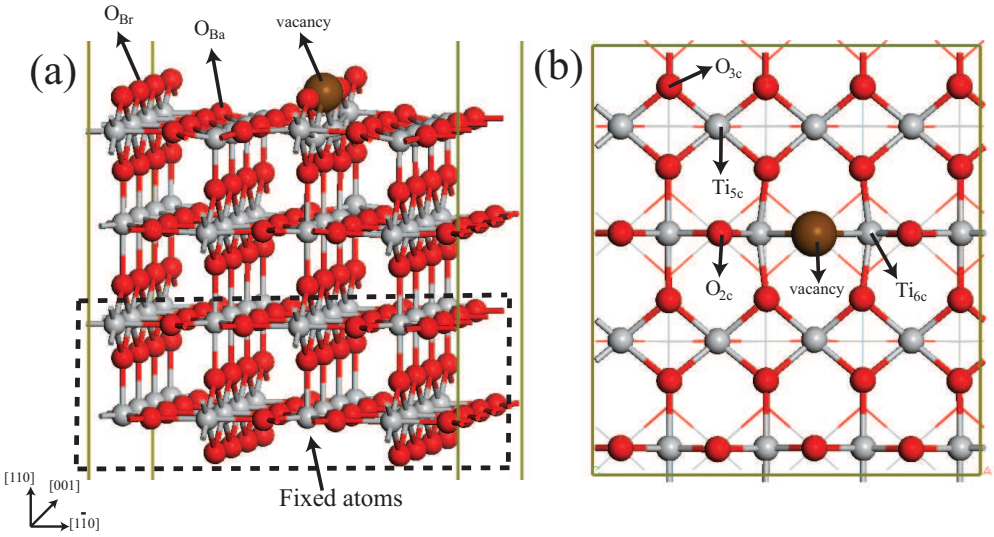

Figure 7.1: Side (a) and top (b) views of the partially reduced 4×2 rutile (110) surface. Position of the O vacancy is displayed by brown color. Gray and red colors represent Ti and O atoms, respectively. The coordination of some of the atoms are indicated as subscripts.

7.1.2 Reduced rutile (110) surface

In this study, 4×2 partially reduced rutile (110) surface is modelled by a four layers thick slab possessing two fixed bottom layers. Figure 7.1 displays side and top view of this partially reduced surface. Reduction of the surface is obtained by removal of a 2–fold coordinated bridge O atom from relaxed structure of the defect free surface and the emergent structure is relaxed again. The energy required to remove one bridging oxygen atom from 4×2 stoichiometric rutile (110) surface to form the partially reduced surface is called the vacancy formation energy E_{vf} and it is calculated using: E_{vf}= E_T[TiO_2(reduced)]+1/2 E_T[O_2]-E_T[TiO_2(stoic)].

Here, $E_T[TiO_2(reduced)]$ and $E_T[TiO_2(stoic)]$ are the total energies of the reduced and stoichiometric surfaces, respectively. In the calculation of E_{vf}, total energy of O_2 molecule in gas phase has been used. The calculated E_{vf} is 3.2 eV. Introducing O vacancy induces significant structural modifications on the ideal rutile surface. The creation of O vacancy causes both inward (along the [110] direction by ∼0.25 Å) and lateral (along the [001] direction by ∼0.2Å) motion of neighboring under-coordinated Ti atoms in order to increase their coordinations. O vacancy density or concentration for this 4×2 surface is 1/8 in our case. Therefore, effect of this defect site on the structure is somewhat local.

7.1.3 Adsorption of Pt_n (n=1–8) clusters on the reduced rutile (110) surface

In the previous two chapters, solar cell application of TiO_2 has been discussed. In addition to this important application, TiO_2 is also used as a widespread catalyst and catalyst support. Pt–TiO_2 and Au–TiO_2 are the most active systems studied by both theoretically and experimentally [118, 119, 120, 121, 122, 123, 124]. Strong–metal–support-interaction (SMSI) [125, 1] is another crucial phenomenon that affects greatly the catalytic activity over the surface. SMSI is a strong interaction observed between the small metal clusters and TiO_2 surface. A fundamental study of the interaction between metal atoms and defect free as well as partially reduced rutile (110) surface will contribute to our understanding about photocatalytic applications of TiO_2 surfaces.

Surface defects such as oxygen vacancies are generally believed to play important roles in the growth of metal clusters. Adsorbed metal adatoms captured at the defect sites act as nucleation sites that attract metal adatoms diffusing on the surface. Furthermore, it is considered that O vacancies influence the catalysis over the metal oxide surfaces. It has been shown that Au_8 cluster absorbed on a partially reduced MgO surface catalyzes CO oxidation at low temperature. However, no reaction has been observed for the same cluster on defect free MgO surface. According to density functional calculations, it has been found that

Au_8 cluster adsorbed on an oxygen vacancy of MgO surface becomes negatively charged and as a result, this charging effect causes the catalytic activity of this cluster [126, 127, 128].

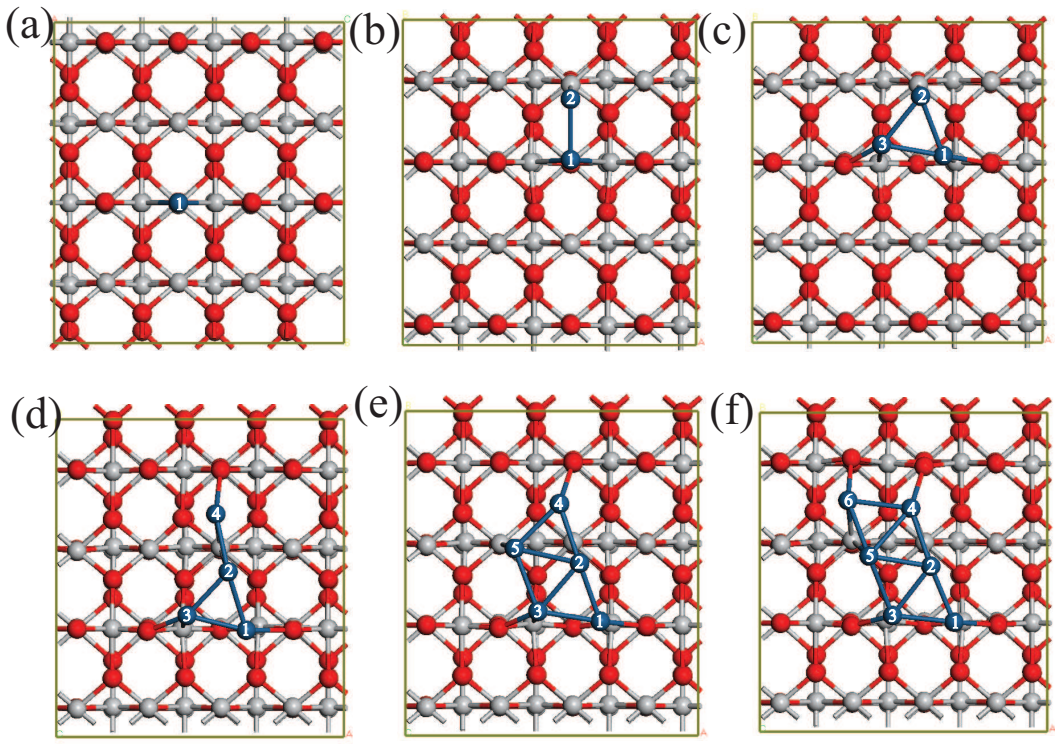

Figure 7.2: Top view of the most energetic adsorption structures for Pt_n (n=1–6) clusters on the the partially reduced 4 × 2 rutile (110) surface. Gray, red and blue colors represent Ti, O and Pt atoms, respectively. Pt atoms are numbered.

7.1.3.1 Pt_1 case

We have first investigated the binding of a Pt atom on a partially reduced surface. A 4 × 2 surface has been used to prevent the interaction between the adjoint clusters. The various possible adsorption sites have been searched not only for Pt monomer but also bigger Pt clusters in order to find the most energetic adsorption sites. The effects of the inclusion of spin polarization on calculations has been tested and found to be negligible. Binding energy per Pt atom (E_b) for Pt_n

clusters has been calculated as follows: $E_b = (E_T[\text{slab}]+nE[\text{Pt}]\text{-}E_T[\text{slab+Pt}_n])/n$. In this formula, E_T[slab], E[Pt], E_T[slab+Pt$_n$] are the total energies of partially reduced 4×2 slab having single O vacancy, free Pt atom and fully relaxed slab+Pt system. Here, n represents the number of Pt atoms adsorbed on the surface. E_b can also be called as the clustering energy. The surface oxygen vacancy site has been found to be the most energetic adsorption site for a single Pt atom with an adsorption energy of 3.15 eV, see Figure 7.2 (a). Pt atom binds directly to two Ti atoms neighboring the vacancy with an average interatomic distance of 2.38 Å. Due to the filling of the oxygen vacancy site by Pt atom, distance between these Ti atoms increases and the structure of the surface relaxes back to the almost defect free surface.

7.1.3.2 Pt_2 case

Pt_2 cluster has been constructed by adding a single Pt (Pt2) atom to Pt_1–surface system and allowing the structure to relax again. This second Pt (Pt2) atom prefers to bind to the previously adsorbed Pt and a 5–fold coordinated Ti atom (Ti_{5c}). Pt1–Pt2 and Pt2–Ti_{5c} bond lengths are 2.51 and 2.34 Å, respectively. E_b is 3.38 eV for this Pt dimer case.

7.1.3.3 Pt_3 case

This cluster is obtained by adding a single Pt (which is Pt3) atom to the ground state structure of the Pt_2–surface system. Not only Pt_3 but also other clusters ($n > 3$) are constructed by using the same procedure. Pt_3 cluster has a triangular ground state structure which lies almost parallel to the surface. Figure 7.2 (c) presents the lowest lying structure of the Pt_3 clusters adsorbed on the surface. Pt1 and Pt3 atoms of the Pt_3 cluster sit at the vacancy site of the reduced surface. The shortest (longest) Pt–Pt bond length is 2.55 (2.64) Å. Pt atoms at the defect site also bind to the neighboring bridge O atoms with a average interatomic distance of 2.04 Å. E_b increases to 3.66 eV when an extra Pt is added to the Pt_2–surface system.

7.1.3.4 Pt_4 case

This cluster has also planar structure. Subsequently adsorbed Pt (Pt4) atom binds to a bridge O (O_{2c}), a Ti_{5c} and Pt2 atom of the Pt_3 cluster. Pt4–O_{2c} and Pt4–Ti_{5c} bond lengths are 2.18 and 2.43 Å. Pt–Pt interatomic distances range from 2.43 to 2.59 Å. Pt2 and Pt4 bind to the same Ti_{5c} atom which is in the valley between the bridging O rows. This Ti_{5c} atom moves upward as a result of the interaction with the cluster. The interatomic distance between Ti_{5c} and its neighboring inner three–coordinated (O_{3c}) O atom increases to 2.54 Å. In this cluster case, E_b is 3.74 eV, which is greater than that of $n < 4$ clusters.

7.1.3.5 Pt_5 case

Figure 7.2 (e) shows the structure of Pt_5 cluster which has a side capped rhombus geometry. Pt5 atom binds to Pt2, Pt3, Pt4 and a Ti_{5c} atom. Pt5–Pt3 and Pt5–Ti_{5c} bond lengths are 2.72 and 2.46, respectively. This Ti_{5c} atom moves 0.17 Å upward from its equilibrium position. In this cluster case, we have calculated E_b to be 3.83 eV.

7.1.3.6 Pt_6 case

The top view of the Pt_6 cluster looks like a bridge extended between two bridge oxygen rows. It has a rhomboid geometry and four corner atoms of the Pt_6 cluster bind to both 5–fold coordinated Ti and 2–fold coordinated bridge O atoms. Pt–Pt (Pt–Ti) interatomic distances range from 2.51 (2.50) to 2.67 (2.68) Å. E_b becomes 3.85 eV upon adsorption of Pt6 atom.

7.1.3.7 Pt_7 case

The lowest lying structure of Pt_7 cluster displayed in Figure 7.3 (a) has a three dimensional structure at which Pt7 atom only binds to cluster atoms (Pt2, Pt4, Pt5

and Pt6) with interatomic distances of 2.90, 2.53, 2.77 and 2.57 Å, respectively.

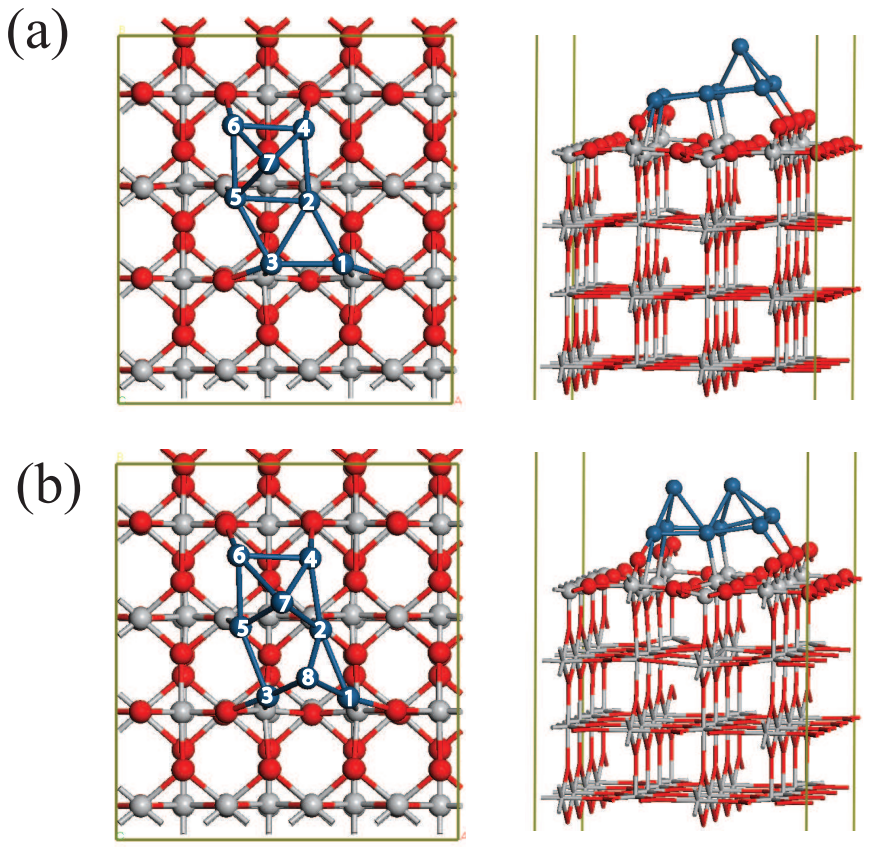

Figure 7.3: Side and top views of the most energetic adsorption structures for Pt_n (n=7–8) clusters on the the partially reduced 4 × 2 rutile (110) surface. Gray, red and blue colors represent Ti, O and Pt atoms, respectively. Pt atoms are numbered.

E_b of this structure is 3.90 eV and its planar isomer is 30 meV less energetic. When Pt7 atom is adsorbed on a similar site which is close to the vacancy, E_b becomes 3.87 eV. The interatomic distance between Pt_6 (Pt_4) and its nearest Ti_{5c} (Ti_{5c}) increases from 2.64 (2.58) to 3.50 (3.44) Å. These Ti atoms slightly move inward. It is noticed that energy difference is very small between the isomers of the Pt_7 clusters. Therefore, various isomers may be found simultaneously at finite temperatures.

7.1.3.8 Pt_8 case

Figure 7.3 (b) shows top and side views of the most energetic structure of Pt_8 cluster. In this cluster, Pt8 is adsorbed on the Pt_7 cluster and there is no direct interaction between the metal oxide and Pt8 atom. Its structure can be considered to be a combination of two distorted square pyramids. Adsorption of Pt8 atom modifies the interatomic distances between Pt1, Pt3 and underlying Ti atoms. For instance, Pt1–Ti bond length increase from 2.56 to 2.80 Å. As expected, E_b of Pt_8 cluster is greater than E_b of Pt_7. Calculated E_b is 3.95 eV. For $n \geq 5$ or planar clusters, adsorption of a Pt atom has relatively local effects on the structural properties of the previously adsorbed cluster. However, effects of Pt7 and Pt8 adatoms are more pronounced and extensive on both interatomic distances and interaction between the cluster and the surface.

7.1.3.9 Energetics

Figure 7.4 displays the variation of the binding energy with the size of the cluster. The binding energy increases with the increasing number of Pt atoms constituting to the cluster due to formation of strong Pt–Pt bonds after $n > 1$. When we add a Pt atom (far away from the vacancy site) to the lowest lying structure of Pt_2–surface system to form Pt_3 cluster, energy difference ΔE between ground state structure of Pt_3–surface and this adsorption mode becomes 0.3 eV. ΔE is 0.27 for Pt_4 and 0.61 eV for Pt_6 cluster. Therefore, each added Pt atom prefers to bind to the previously adsorbed Pt cluster. As a result, the vacancy site behaves as a nucleation center for the growth of Pt clusters on the partially reduced rutile (110) surface. Planar structure is favorable up to $n = 6$. We have also formed 2D clusters for $n = 7$ and $n = 8$. E_b for planar clusters begins to saturate after $n = 5$, see Figure 7.4. A sharp increases in E_b is observed when we go from $n = 6$ to $n = 7$ cluster. Three–dimensional counterparts of the planar clusters $n \leq 6$ have also been examined. For $n = 4$ cluster, energy difference between the ground state structure (which has planar geometry) and its three dimensional isomer having tetrahedron structure is 0.32 eV. All clusters interact with the surface strongly.

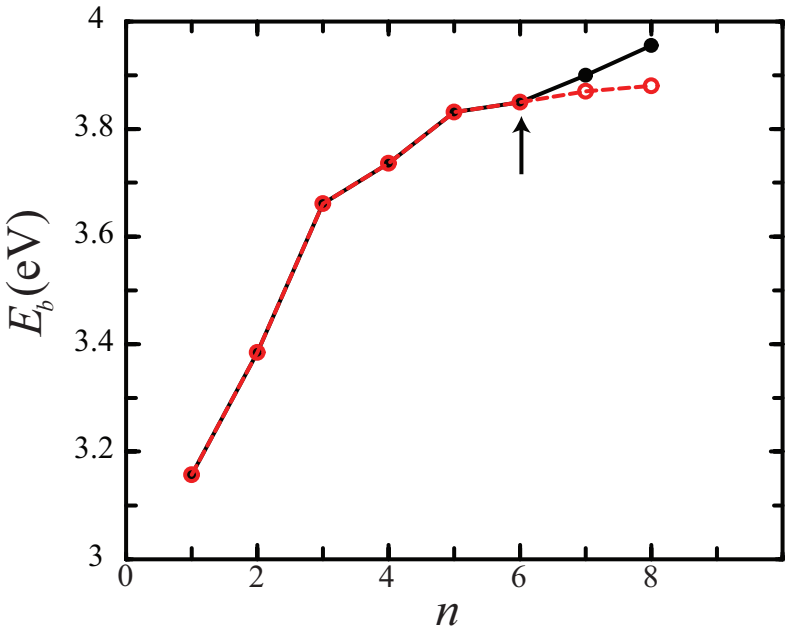

Figure 7.4: Variation of the binding energy E_b with size of the cluster. Solid and dashed lines represent E_b of the lowest lying and two dimensional structures, respectively.

It is known that oxide surface–metal cluster interaction influences greatly the catalytic activity of the supported metal cluster. In this work, total energy of the oxide supported clusters has been calculated. In reality, free energy is the most important physical quantity and cluster–surface system may not be at equilibrium. Therefore, metastable structures might thermodynamically form on the surface. The concentration of vacancies influence reactivity of these defect sites, growth of metal clusters and interfacial properties between the surface and supported metal cluster. In this study, we have examined the reduced surface which has low vacancy concentration.

7.1.3.10 Electronic structure

The partial density of states (PDOS) plots of the adsorbed Pt clusters and the underlying surface are displayed in Figure 7.5. The zero of the energy corresponds

to the Fermi level.

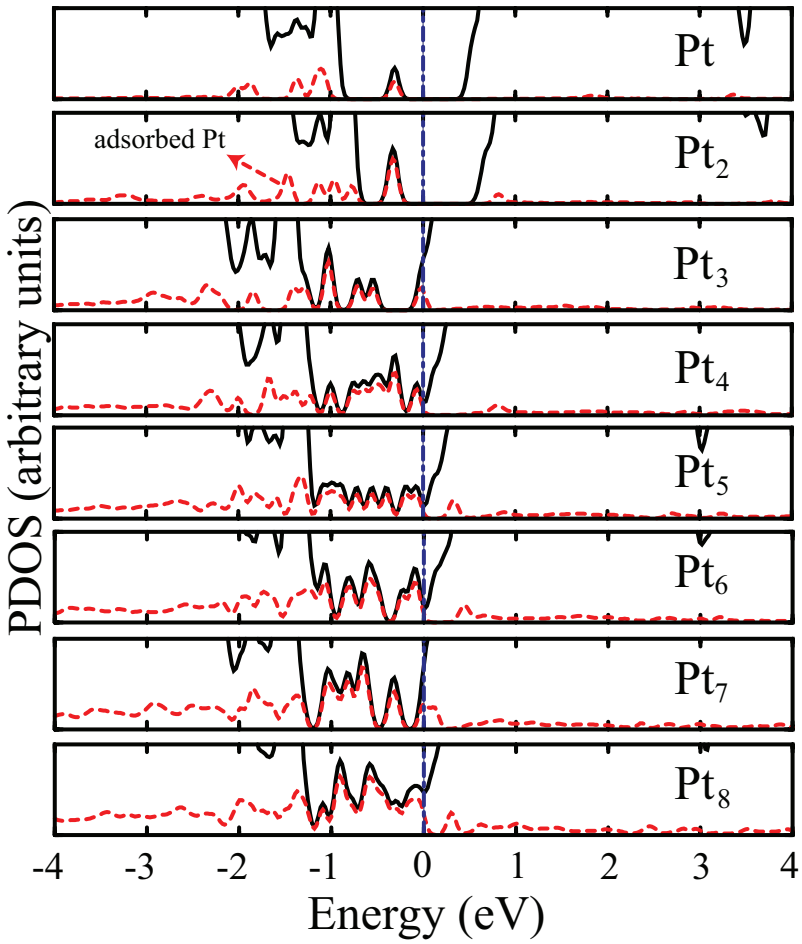

Figure 7.5: Partial density of states (PDOS) of the Pt_n–surface system. Solid line is the total DOS for TiO_2–Pt_n. Fermi level is shown by dotted–dashed line.

It is noticed that metal–induced states in the band gap of the surface exist in all clusters. For $n = 1$ and 2, Pt_n–TiO_2 system exhibits semiconductor behavior. Adsorption of Pt monomer and Pt_2 dimer reduces the band gap from 1.3 of the clean surface to 0.8 eV. As a result of this reduction in the effective band gap, optical threshold of Pt–TiO_2 and Pt_2–TiO_2 systems is lower than that of the clean surface. The gap localized states for Pt–TiO_2 and Pt_2–TiO_2 systems are mainly d and s character of Pt atoms and p character of surface O atoms, see Figure 7.6. For the monomer case, there is very little Pt contribution to the CB of

the surface. Bader charge [129, 130] analysis provides that 0.61 e^- transfers from surface to Pt atom. According to this result, reduced rutile surface acts as an electron donor. Bader charge on each Pt atom of Pt_n clusters has been calculated and results are tabulated in Table 7.1. It has been proposed that the charge state of the oxide supported metal clusters play an important role in catalytic activity of these clusters [131].

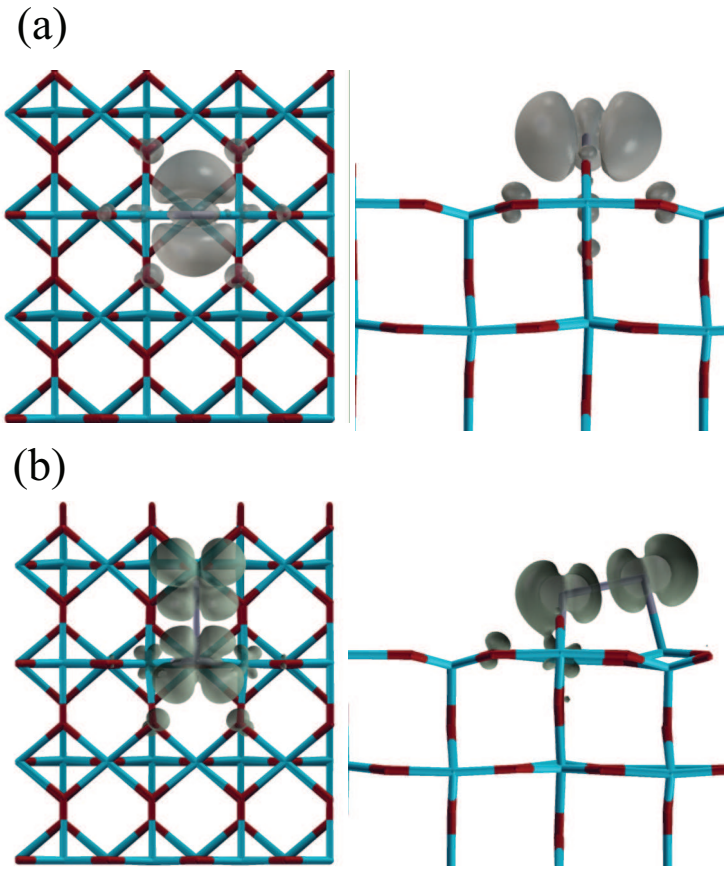

Figure 7.6: Partial charge density plot of HOMO level of (a) Pt_1 and (b) Pt_2–surface systems. Top and side views are shown in right and left figures, respectively.

Pt2 and Pt5 atoms are always negatively charged. Both Pt atoms bind to surface 5–fold coordinated Ti (Ti_{5c}) atoms. Bond strength between these Ti atoms and their neighboring inner 3–coordinated O atoms is weakening upon adsorption of

Table 7.1: Bader charge on each atom of Pt_n clusters. Total charge ΔQ on each cluster is also given in units of e^-.

atom no	Pt	Pt_2	Pt_3	Pt_4	Pt_5	Pt_6	Pt_7	Pt_8
Pt1	-0.61	-0.31	0.03	0.003	0.04	0.01	0.03	0.07
Pt2		-0.23	-0.27	-0.19	-0.16	-0.12	-0.13	-0.12
Pt3			0.05	0.07	0.05	0.01	-0.05	0.16
Pt4				-0.12	0.07	0.08	0.3	0.31
Pt5					-0.23	-0.16	-0.17	-0.23
Pt6						0.04	0.25	0.20
Pt7							-0.13	-0.10
Pt8								-0.16
ΔQ	-0.61	-0.54	-0.19	-0.24	-0.25	-0.14	0.11	0.13

Pt2 and Pt5, which leads to a charge transfer from Ti_{5c} atoms to Pt2 and Pt5. It is noticed that Pt1 atom is positively charged when $n > 2$. When we sum up the Bader charge on each atom, it is seen that the clusters are negatively charged for $n \leq 6$. The absolute value of the total charge takes the highest value in Pt monomer with a charge of 0.61 e^-. It can also be inferred that binding with O atom influences the charge state of a particular Pt atom. In general, only Pt2 and Pt5 atoms, which do not directly bind to any O atoms, are always negatively charged. Each adsorbed Pt atom modifies the charge distribution over the previously adsorbed Pt cluster. This argument can easily seen by investigation of Table 7.1. ΔQ becomes positive upon adsorption of Pt7 and Pt8 atoms. The charge state of the clusters can be switched between opposite charges by changing the structure of the clusters. We have also found that not only the lowest lying structures of $n \leq 6$ clusters but also planar $n = 7$ and $n = 8$ clusters are negatively charged. As a result, it is expected that a continues Pt monolayer over the partially or full reduced rutile surface is negatively charged. We can propose that direct contact among the cluster atoms and titania surface is crucial for charge state of the supported metal cluster and interatomic distance between Ti_{5c} and its neighboring inner O_{3c} atom controls the charge transfer between Pt_n cluster and surface. Pt_n–TiO_2 system turns into metallic system when $n \geq 3$. The gap of the surface is filled by energy states of cluster atoms and the gap

disappears, indicating metallization of the Pt–surface system. The Fermi level is pinned by Pt atoms.

7.1.4 Adsorption of bimetallic Pt_2Au_m (m=1–5) clusters on the reduced rutile (110) surface

It has been shown that Au migration profile on the stoichiometric rutile (110) surface is quite flat relative to Pt atom [122]. Au can easily diffuse on the stoichiometric surface. Both Pt and Au atoms prefer to bind to the O vacancy site of the reduced surface. However, Au is much more likely to escape from this defect site compared to Pt. Because of these results, it can be inferred that catalytic activity of Au clusters or nanoparticles is sensitive to the preparation methods. Au clusters are sintered easily at high temperatures, which leads to not only a loss of surface area but also a loss of catalytic activity. This is an important problem for nanosized Au catalysis. Bimetallic Pt–Au clusters offer important advantages for catalysis applications. First of all, existence of Pt atoms in Pt–Au clusters prevents sintering [132] compared to pure Au clusters. The oxide–supported metal cluster interaction can be tuned by changing the composition of the Pt–Au bimetallic clusters. Furthermore, Pt–Au clusters can be a better catalysts for a particular reaction compared to pure Pt and Au clusters. Pt–Au bimetallic nanoparticles have been used a catalysts for NO reduction [133], CO oxidation [134] and CH_3OH oxidation [135]. Therefore, a detailed analysis of bimetallic Pt–Au cluster supported on the oxide surfaces is necessary.

In this study, we have also examined the structural and electronic properties of bimetallic Pt–Au (Pt_2Au_m, m=1–5) clusters. First of all, a Pt_2 dimer is adsorbed by the 4×2 rutile (110) surface having single oxygen vacancy. Next step is the growth of Au_m (m=1–2) clusters on this platinized surface atom by atom to simulate the experiments correctly. Figure 7.7 displays the lowest lying structures of Pt–Au bimetallic clusters for each m. We have also searched the possible spin polarization on the bimetallic clusters. However, imposing of the magnetism on calculations have not altered both lowest lying structures and relative energies

among the isomers for Pt_2Au, Pt_2Au_2 and Pt_2Au_3.

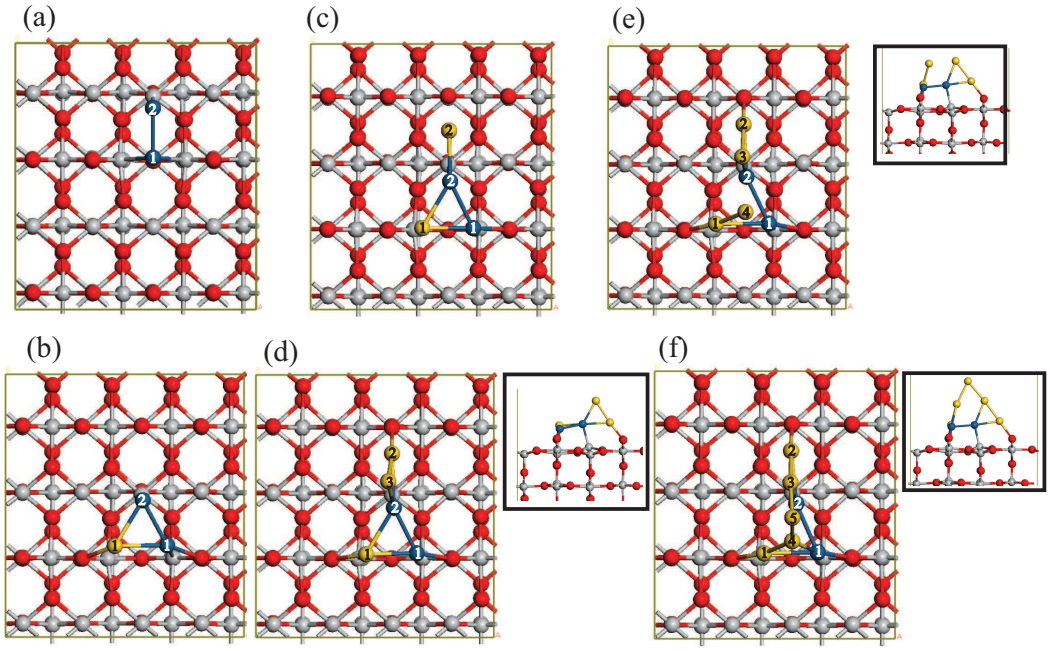

Figure 7.7: Side and top views of the most energetic adsorption structures for Pt_2Au_m (m=1–5) (b) to (f) bimetallic clusters on the the partially reduced 4×2 rutile (110) surface. Gray, red, blue and yellow colors represent Ti, O, Pt and Au atoms, respectively. Pt and Au atoms are numbered.

Hence, the results obtained without inclusion of spin polarization have been presented. The smallest Pt–Au cluster is Pt_2Au_1. In this cluster, Au atom prefers to sit at the vacancy site which has been already occupied by a Pt (Pt1) atom. The adsorbed Au atom pushes this Pt atom toward neighboring bridge O atom and resulted cluster has triangular geometry. Interatomic distances of Au–Ti, Au–Pt1, Au–Pt2 and Au–O_{2c} are 2.88, 2.62, 2.68 and 2.20 Å, respectively. The binding energy per Au atom E_b has been defined as: $E_b = (E_T[\text{slab+Pt}_2]+mE[\text{Au}]-E_T[\text{slab+Pt}_2\text{+Au}_m])/m$. In this formula, $E_T[\text{slab+Pt}_2]$ and $E_T[\text{slab+Pt}_2\text{+Au}_m]$ are the total energies of slab–Pt_2 and slab–Pt_2–Au_m systems. The ground state structure of the Pt_2–TiO_2 and Pt_2Au_m–TiO_2 systems are displayed in Figure 7.7. E_b is 2.55 eV for $m = 1$ case. The binding energy of a Au atom on the partially

Table 7.2: Bader charge on each atom of bimetallic Pt_2Au_m clusters. Total charge ΔQ (in unit of e^-) on each cluster and E_b (in eV) are given. d^l, d^s and d^{ave} are the shortest, longest and average interatomic distances between corresponding atoms in Å.

atom no	Pt_2Au	Pt_2Au_2	Pt_2Au_3	Pt_2Au_4	Pt_2Au_5
Pt1	0.05	0.02	0.01	0.06	0.06
Pt2	-0.23	-0.26	-0.24	-0.22	-0.21
Au1	0.12	0.01	0.03	0.15	0.14
Au2		-0.02	0.24	0.16	0.13
Au3			-0.01	-0.04	0.00
Au4				-0.08	0.00
Au5					-0.08
ΔQ	-0.06	-0.25	0.03	0.02	0.04
E_b	2.56	2.46	2.46	2.45	2.56
$d_{Pt1-Pt2}$	2.57	2.61	2.59	2.60	2.62
d^l_{Au-Au}			2.57	2.68	2.89
d^s_{Au-Au}			2.57	2.65	2.61
d^{ave}_{Au-Au}			2.57	2.67	2.70
d^l_{Au-Pt}	2.68	2.68	2.72	2.71	2.72
d^s_{Au-Pt}	2.62	2.52	2.55	2.65	2.64
d^{ave}_{Au-Pt}	2.65	2.58	2.66	2.67	2.68

reduced rutile (110) surface has been calculated as 1.62 eV. There is an enhancement of the binding of Au atom on the reduced surface due to presence of Pt dimer on that surface. It has been shown that Pt atom binds more strongly to the both clean and reduced rutile (110) surface than Au atom [122]. Pt_2Au_2 cluster has planar geometry which is similar to the lowest lying structure of Pt_4 cluster. Au2 atom interacts with Pt2 atom more strongly than neighboring Ti_{5c} and bridge O_{2c} atoms. Au2–Pt2, Au2–Ti_{5c} and Au2–O_{2c} interatomic distances are 2.52, 2.86 and 2.39 Å, respectively. Three–dimensional structures become more energetic for $m \geq 3$ and Pt–Au bimetallic clusters tend to grow along [110] direction. E_b follows a constant value for m=2,3 and 4. It takes the highest value as 2.56 eV for both Pt_2Au and Pt_2Au_5 clusters. Several optimized structural parameters and binding energies E_b are presented in Table 7.2. In Au dimer and fcc bulk, Au–Au interatomic distances are 2.53 and 2.88 Å, respectively. It is noticed that average Au–Au bond lengths for Pt–Au bimetallic clusters are between those of dimer and bulk, which is a result of having different coordination number of Au atoms in these three structures. Au clusters prefer to grow around the previously adsorbed Pt dimer which behaves as a nucleation center. Due to strong interaction between Au and platinized surface compared to interaction between Au and clean as well as reduced surface, Au clusters are prevented from sintering which causes the reduction of catalytic activities of nanosized Au particles.

We have also calculated the Bader charge on each atom and total charge for all Pt–Au clusters, see Table 7.2. As in the case of Pt_n clusters, Pt2 atom is always negatively charged. Pt1, Au3, Au4 and Au5 atoms exchange small amount of charge with other Au atoms, Pt2 and oxide surface compared to Pt2, Au1 and Au2. Only Pt_2Au and Pt_2Au_2 clusters are negatively charged. Alloying Pt cluster with Au atoms can modify electronic properties of the bare Pt cluster. For instance, Pt1 atom is negatively charged in the pure Pt_2 cluster adsorbed on reduced surface. Adsorption of a gold atom by Pt_2–surface system changes drastically total charge on Pt1 atom. Charge transfer between Au and Pt atoms supplies new degrees of freedom to get better catalyst. By playing with composition, size and structure of Pt–Au bimetallic clusters, we can tune electronic

properties as well as charge transfer between Au and Pt atoms. In general, absolute value of ΔQ is greater for Pt_n cluster than that of Pt_2Au_m bimetallic case.

Chapter 8

CONCLUSION

First of all, we have studied structural and electronic properties of isolated TiO_2 clusters in different sizes and their interaction with H_2O and transition metal atoms like Co, V, and Pt. The structure and size of the clusters have prominent effects on both electronic and chemical properties of these zero–dimensional (0D) structures. In general, clusters prefer to form three–dimensional (3D) structures in their ground states. Stability of isolated clusters increases as the cluster size grows. The coordination of O and Ti atoms is an important criterion to form more stable clusters. Except dangling O atoms, Ti and O atoms are at least 4–fold and 2–fold coordinated in the lowest energy structures. Although $n \geq 8$ clusters possess two 1–fold coordinated O atoms, the number of pendant atoms is one and zero in the ground state of n=9 and n=10 clusters, respectively. HOMO–LUMO orbital energies and their differences have also been calculated to explore the electronic properties of clusters. HOMO–LUMO gap values do not follow a regular pattern. According to the quantum size effect, band gap of a nanoscale material is bigger than its bulk counterpart and this band gap approaches the bulk gap value as the size of the material grows. In our study, we have not observed any quantum size effect in TiO_2 clusters. Interaction of such small systems with molecules or single atoms like H_2O or TM atoms is important for both understanding the experimental results and developing new device applications by using these clusters. Interaction strength of H_2O with clusters depends on

the size of the cluster and there is an oscillatory decrease in the binding energy E_b of the water molecule. In the case of more than one water molecule adsorption, E_b per H_2O molecule decreases with the increasing number of the adsorbed molecule N. The reduction in E_b per H_2O is more pronounced for clusters n=3 or 4 compared to n=10. The interaction of n=10 cluster with TM atoms has been studied. Magnetic moment is induced on n=10 cluster upon adsorption of Co and V atoms. Induced moments are 1 and 3 μ_B for Co and V, respectively. TM elements interact with this cluster forming strong chemisorption bonds.

Nanowires are one dimensional (1D) structures that might exhibit unusual physical and chemical properties. In this part, we have examined the 1D TiO_2 materials or infinite nanowires. Structural, electronic and magnetic properties of atomically thin TiO_x (x=1,2) and bulk–like rutile (110) nanowires have been studied. All stoichiometric thin TiO_2 nanowires are semiconducting and have non–magnetic ground state. It has been found that there is a strong correlation between E_g and E_b of these TiO_2 nanowires. To gain more insight about the relative stability of the atomically thin stoichiometric TiO_2 nanowires, we have also studied the bulk–like rutile (110) nanowires, which are cut in a rod–like structure from bulk rutile and oriented along the [110] crystallographic direction. These bulk–like nanowires become more energetic with respect to thin nanowires after a certain cross–section and all of them exhibit semiconducting behavior. E_g of these thick nanowires oscillates around the theoretical E_g of bulk rutile. Non-stoichiometric thin TiO wires have also been studied. They can exhibit various electronic and magnetic properties. We have both metallic and semiconducting wires. Unlike stoichiometric titania nanowires, some of the TiO wires have magnetic ground state.

In the following three sections, we have concentrated on the TiO_2 anatase (001) and rutile (110) surfaces and their interaction with dye molecules and metal atoms, namely Pt and Au. In the first part, adsorption of BrPDI, BrGly, and BrAsp dye molecules on UR and RC anatase TiO_2 (001) surfaces adapts the electronic structure of combined system and lowers the optical threshold to visible light. Resulting electronic structure depends on the type of the dye molecule as well as the surface structure. BrPDI causes gap narrowing when it is adsorbed by

the RC surface. In UR–BrGly, RC–BrGly and RC–BrAsp surface–dye systems, HOMO level of molecule appears in the band gap region. We have shown that these molecules form strong chemical bonds with both the UR and RC surfaces. Therefore, the surface–dye system is very stable. We have also studied the effects of complete hydration of the surfaces on binding of BrPDI. E_b drops significantly in the existence of water.

In the second part of the surface section, we have studied the interaction between perylene–based dye molecules (BrPDI, BrGly, and BrAsp) and defect free as well as partially reduced and platinized rutile (110) surfaces. Dye molecules bind to the clean rutile surface with weaker interactions compared to anatase–dye system. In all dye cases, E_b is about 1 eV. Regardless of the type of the dye molecules, HOMO and LUMO levels of the adsorbed dye appear within the gap and the conduction band regions of defect free surface, respectively. We have performed the calculations on both three and four layers thick defect free slabs. It is observed that the computed binding energies of the dye molecules are dependent on the thickness of the slab. Dyes bind to three layers slab more strongly. Defects always exist on the surfaces. We have also studied the interaction between BrPDI dye and partially reduced rutile surface. For the reduced surface, dye prefers to bind to the vacancy site.

TiO_2 is also used as a widespread catalyst and catalyst support. Pt–TiO_2 and Au–TiO_2 are the most active systems studied both experimentally and theoretically. In this third part, we have examined the structural and electronic properties of small Pt_n (n=1–8) and bimetallic Pt_2Au_m (m=1–5) clusters, supported on 4×2 rutile (110) surface having single oxygen vacancy. The most favorable adsorption geometries for each n and m have been obtained. In Pt monomer case, Pt atom prefers to bind to the O vacancy site. Clusters tend to grow around this Pt monomer. The vacancy behaves as a nucleation center. Pt_{n-1} (or Pt_2Au_{m-1}) cluster has been obtained by adding a single Pt (Au) atom to the ground state structure of Pt_{n-2} (Pt_2Au_{m-2}) cluster. Binding energy per Pt atom (E_b) of Pt clusters on the rutile surface increases as the cluster size grows. E_b for Pt monomer is 3.38 eV and it becomes 3.96 eV in Pt_8 cluster case. For

n=1–6, Pt clusters have planar ground state structures. After n=7, three dimensional clusters become more energetic. We have calculated the partial density of states (PDOS) for the ground state structure of each Pt_n cluster. Pt–surface system exhibits metallic properties after $n \geq 3$. Energy levels of adsorbed Pt atoms appear mostly within the valance band and band gap regions of the reduced surface. The conduction band edge is populated by energy states of Pt atoms when $n \geq 3$. For n= 1 and 2 cases, occupied Pt states appear within the band gap. As a result of these states, optical response of the Pt–surface system is lower than UV. In the bimetallic PtAu cluster case, Au cluster has been grown on the Pt_2–surface system. Pt dimer has been previously adsorbed at the vacancy site. Au cluster has been nucleated around this Pt dimer. E_b of Au cluster is almost constant and lower than E_b of Pt clusters. Bader analysis has revealed that charge transfer among the Pt atoms of Pt_n clusters and metal oxide surface is stronger compared to the Pt_2Au_m–surface system.

In this thesis, we have presented a complete picture for the structural, electronic and magnetic properties for the 0D, 1D, and 2D TiO_2 based nanostructures. We believe that our results are fundamental and useful for the photovoltaic and photocatalytic applications.

Bibliography

[1] U. Diebold, Surf. Sci. Rep. **48** , 53-229 (2003).

[2] T. L. Thompson and J. T. Yates, Chem. Rev. **106**, 4428 (2006).

[3] X. Chen and S. S. Mao, Chem. Rev. **107**, 2891 (2007).

[4] M. Grätzel, Nature **414**, 338 (2001).

[5] M. Grätzel, J. Photochem. Photobiol. C **4**, 145 (2003).

[6] A. Hagfeldt and M. Grätzel, Chem. Rev. **95**, 49 (1995).

[7] M. Grätzel, J. Photochem. Photobiol., A: Chem. **3**, 164 (2004).

[8] A. Fujishima and K. Honda, Nature 238, 27 (1972).

[9] A. Fujishima, K. Hashimoto and H. Watanabe, TiO_2 Photocatalysis: Fundamentals and Applications; BKC, Inc.: Tokyo, Japan (1997).

[10] R. Wang, K. Hashimoto, A. Fujishima, M. Chikuni, E. Kojima, A. Kitamura, M. Shimohigoshi and T. Watanabe, Nature **388**, 431 (1997).

[11] K. Sunada, Y. Kikuchi, K. Hashimoto and A. Fujishim, Environ. Sci. Technol. **32**, 726 (1998).

[12] N.-L. Wu, S.-Y. Wang, and L. A. Rusakova, Science **285**, 1375 (1999).

[13] R. Asahi, T. Morikawa, T. Ohwaki, K. Aoki and Y. Taga, Science **293**, 269 (2001).

[14] S. U. M. Khan, M. Al-Shahry and W. B. Ingler, Science **297**, 2243 (2002).

[15] C. D. Valentin, G. Pacchioni and A. Selloni, Phys. Rev. B 70, 085116 (2004).

[16] S. Livraghi, M. C. Paganini, E. Giamello, A. Selloni, C. D. Valentin and G. Pacchioni, J. Am. Chem. Soc. **128**, 15666-15671 (2006).

[17] C. D. Valentin, G. Pacchioni, A. Selloni, S. Livraghi and E. Giamello, J. Phys. Chem. B **109**, 11414 (2005).

[18] C. D. Valentin, G. Pacchioni and A. Selloni, Chem. Mater. **17**, 6656-6665 (2005).

[19] J.-Y. Lee, J. Park and J.-H. Choa, Appl. Phys. Lett. **87**, 011904 (2005).

[20] J. Kohanoff and N. Gidopoulos, Density Functional Theory: basics, new trends and applications, Handbook of Molecular Physics and Quantum Chemistry, Volume 2, Part 5, Chapter 26, pp 532-568 (Wiley, Chichester, 2003).

[21] M. C. Payne, M. P. Teter, D. C. Allen, T. A. Arias and J. D. Joannopoulos, Rev. Mod. Phys. **64**, 1045 (1992).

[22] R. Martin, Electronic Structure: Basic Theory and Practical Methods, Cambridge University Press (2004).

[23] M. Born and J. R. Oppenheimer, Ann. der Phys. **84**, 457 (1927).

[24] D. R. Hartree, Proc. Cambridge. Philos. Soc. **24**, 89 (1928).

[25] J. C. Slater, Phys. Rev. **35**, 210 (1930).

[26] V. Fock, Z. Phys. **61**, 126 (1930).

[27] L. H. Thomas, Proc. Cambridge. Philos. Soc. **23**, 542 (1927).

[28] E. Fermi, Z. Phys. **48**, 73 (1928).

[29] P. Hohenberg and W. Kohn, Phys. Rev. **136**, B864 (1964).

[30] W. Kohn and L. J. Sham, Phys. Rev. **140**, A1133 (1965).

[31] D. M. Ceperley and B. J. Alder, Phys. Rev. Lett. **45**, 566 (1980).

[32] J. P. Perdew and Y. Wang, Phys. Rev. B **45**, 13244 (1991).

[33] A. D. Becke, Phys. Rev A **38**, 3098-3100 (1988).

[34] J. P. Perdew, K. Burke, and M. Ernzerhof, Phys. Rev. Lett, **77**, 3865-3868 (1996).

[35] D. Vanderbilt, Phys. Rev. B **41**, R7892 (1990).

[36] P. E. Blöchl, Phys. Rev. B **50**, 17953-17979 (1994).

[37] C. Kittel Introduction to Solid State Physics (Wiley and Sons, New York, 1996).

[38] H. J. Monkhorst and J. D. Pack, Phys. Rev. B **13**, 5188, (1976).

[39] Numerical computations have been carried out by using VASP software: G. Kresse, J. Hafner, Phys Rev. B **47**, R558 (1993); G. Kresse, J. Furthmuller, Phys Rev. B **54**, 11169 (1996).

[40] M. Anpo, T. Shima, S. Kodama and Y. Kubokawa, J. Phys. Chem. **91**, 179 (1987).

[41] N. S. McIntyre, K. R. Thompson, W. Weltner, Jr., J. Phys. Chem. **75**, 3243 (1971).

[42] G. Balducci, G. Gigli and M. J. Guido, Chem. Phys. **83** ,1909 (1985).

[43] G. Balducci, G. Gigli and M. J. Guido, Chem. Phys. **83**, 1913 (1985).

[44] W. Yu and R. B. J. Freas, Am. Chem. Soc. **112**, 7126 (1990).

[45] B. C. Guo, K. P. Kerns and A. W. Castleman, Int. J. Mass Spectrom. Ion Processes **117**, 129 (1992).

[46] G. V. Chertihin and L. J. Andrews, Phys. Chem. **99**, 6356 (1995).

[47] H. B. Wu and L. S. J. Wang, J. Chem. Phys. **107**, 8221-8228 (1997).

[48] M. Foltin, G. J. Stueber and E. R. J. Bernstein, Chem. Phys. **111**, 9577 (1999).

[49] Y. Matsuda, and E. R. J. Bernstein, Phys. Chem. A **109**, 314 (2005).

[50] H. J. Zhai and L. S. Wang, J. Am. Chem. Soc. **129**, 3022-3026 (2007).

[51] A. Hagfeldt, R. Bergström, H. O. G. Siegbahn and S. Lunell, J. Phys. Chem. **97**, 12725-12730 (1993).

[52] R. Bergström, S. Lunell and L. A. Eriksson, Int. J. Quantum Chem. 59, 427-443 (1996).

[53] M. B. Walsh, R. A. King and H. F. Schaefer, J. Chem. Phys. **110**, 5224-5230 (1999).

[54] T. Albaret, F. Finocchi and C. Noguera, Faraday Discuss. **114**, 285-304 (1999).

[55] T. Albaret, F. Finocchi and C. Noguera, Appl. Surf. Sci. **145**, 672-676 (1999).

[56] T. Albaret, F. Finocchi and C. Noguera, J. Chem. Phys. **113**, 2238-2249 (2000).

[57] K. S. Jeong, C. Chang, E. Sedlmayr and D. Sülze, J. Phys. B.:At. Mol. Opt. Phys. **33**, 3417-3430 (2000).

[58] S. Hamad, C. R. A. Catlow, S. M. Woodley, S. Lago and J. S. Mejias, J. Phys. Chem. B **109**, 15741-15748 (2005).

[59] S. M. Woodley, S. Hamad, J. S. Mejias and C. R. A Catlow, J. Mater. Chem. **16**, 1927-1933 (2006).

[60] Z.-W. Qu and G.-J. Kroes, J. Phys. Chem. B **110**, 8998-9007 (2006).

[61] Z.-W. Qu and G.-J. Kroes, J. Phys. Chem. C **111**, 16808-16817 (2007).

[62] P. Persson, J. C. Gebhardt and S. Lunell, J. Phys. Chem. B **107**, 3336-3339 (2003).

[63] M. J. Lundqvist, M. Nilsing, P. Perssson, and S. Lunell, Int. J. Quantum Chem. **106**, 3214 (2006).

[64] A. S. Barnard, S. Erdin, Y. Lin, P. Zapol and J. W. Halley, Phys. Rev. B **73**, 205405 (2006).

[65] V. N. Kopared, and P. T. Cummings, J. Phys. Chem. B **109**,24280 (2005).

[66] P. K. Naicker, P. T. Cummings, H. Zhang, and J. F. Banfield, J. Phys. Chem. B **109**,15243 (2005).

[67] V. V. Hoang, Phys. Stat. Sol. **244**, 1280 (2007).

[68] P. C. Redfern, P. Zapol, L. A. Curtiss, T. Rajh and M. C. Thurnauer, J. Phys. Chem. B **107**, 11419-11427 (2003).

[69] A. S. Barnard, P. Zapol and L. A. Curtiss, J. Chem. Theo. Comm. **1**, 107-116 (2005).

[70] S. Erdin, Y. Lin, J. W. Halley, P. Zapol, P. Redfern and L. Curtiss, J. Electroanal. Chem. **607**, 147-157 (2007).

[71] V. N. Koparde and P. Cummings, J. Phys. Chem. C **111**,6920 (2007).

[72] K. P. Huber, G. Herzberg, In Molecular Spectra and Molecular Structure IV. Constants; Van Nostrand Reihold: New York (1979).

[73] N. Serpone, D. Lawless and R. Khairutdinov, J. Phys. Chem. **99**, 16646 (1995).

[74] Y. Matsumoto, M. Murakami, T. Shono, T. Hasegawa, T. Fukumura, M. Kawasaki, P. Ahmet, T. Chikyow, Shin-ya Koshihara and H. Koinuma, Science **291**, 854856 (2001).

[75] M. S. Park, S. K. Kwon and B. I. Min, Phys. Rev. B **65**, 161201 (2002).

[76] J.-Y. Kim, J.-H. Park, B.-G. Park, H.-J. Noh, S.-J. Oh, J. S. Yang, D.-H. Kim, S. D. Bu, T.-W. Noh, H.-J. Lin, H.-H. Hsieh and C. T. Chen, Phys. Rev. Lett. **90**, 017401 (2003).

[77] Z. Yang, G. Liu and R. Wu, Phys. Rev. B **67**, 060402 (2003).

[78] W. T. Geng and K. S. Kim, Phys. Rev. B **68**, 125203 (2003).

[79] N. H. Hong, J. Sakai and A. Hassini, Appl. Phys. Lett. **84**, 2602 (2004).

[80] L.-H. Ye and A. J. Freeman, Phys. Rev. B **73**, 081304 (2006).

[81] X. Du, Q. Li, H. Su and J. Yang, Phys. Rev. B **74**, 233201 (2006).

[82] Ll. Balcells, C. Frontera, F. Sandiumenge, A. Roig, B. Martnez, J. Kouam, and C. Monty, Appl. Phys. Lett. **89**, 122501 (2006).

[83] X. W. Wang, X. P. Gao, G. R. Li, L. Gao, T. Y. Yan and H. Y. Zhu, Appl. Phys. Lett. **91**, 143102 (2007).

[84] G. Wang, Q. Wang, W. Lu, and J. Li, J. Phys. Chem. B. **110**, 22029-22034 (2006).

[85] B. Tan and Y. Wu, J. Phys. Chem. B **110**, 15932-15938 (2006).

[86] J. Jiu, S. Isoda, F. Wang, and M. Adachi, J. Phys. Chem. B **110**, 2087-2092 (2006).

[87] S. P. Albu, A. Ghicov, J. M. Macak, R. Hahn, and P Schmuki, Nano lett. **7**, 1286 (2007).

[88] M. Blanco-Rey, J. Abad, C. Rogero, J. Mendez, M. F. Lopez, J. A. Martin-Gago and P. L. de Andres, Phys. Rev. Lett **96**, 055502 (2006).

[89] B. Yilmaz, J. Warzywoda and A. Sacco Jr., Nanotechonology **17**, 4092 (2006).

[90] B. Yilmaz and A. Sacco Jr. and J. Deng, Appl. Phys. Lett. **90**, 152101 (2007).

[91] S. S. Amin, A. W. Nicholls and T. T. Xu, Nanotechonology **18**, 445609 (2007).

[92] B. Poudel, W. Z. Wang, C. Dames, J. Y. Huang, S. Kunwar, D. Z. Wang, D Banerjee, G. Chen, and Z. F. Ren, Nanotechonology **12**, 1935 (2005).

[93] A. Damin, F. X. L. i Xamena, C. Lamberti, B. Civalleri, C. M. Z. Wilson, and A. Zecchina, J. Phys. Chem. B **108**, 1328 (2004).

[94] A. N. Enyashin, V. V. Ivanovskaya, Y. N. Makurin, V. G. Bamburov, and A. L. Ivanovskii, Dokl. Phys. Chem. **391**, 187 (2003).

[95] A. N. Enyashin and G. Seifert, Phys. Stat. Sol. (b) **242**, 1361 (2005).

[96] M. Methfessel, A. T. Paxton, Phys. Rev. B **40**, 3616 (1989).

[97] S. C. Abrahams and J. L. Bernstien, J. Chem. Phys. **55**, 3206 (1971).

[98] J. K. Burdett, T. Hughbanks, G. J. Miller, J. W. Richardson, Jr., and J. V. Smith, J. Am. Chem. Soc. **109**, 3639 (1987).

[99] C. J. Howard, Z. M. Sabine, and F. Dickson, Acta Crystallogr. Sect. B: Struct. Sci. **47**, 462 (1991).

[100] S. J. Thompson and S. P. Lewis, Phys. Rev. B **73**, 073403 (2006).

[101] A. Kiejna, T. Pabisiak, and S. W. Gao, J. Phys: Condensed Matter **18**, 4207 (2006)

[102] S. P. Bates, G. Kresse and M. J. Gillan, Surf. Sci. **385**, 386 (1997).

[103] T. Bredow, L. Giordano, F. Cinquini, and G. Pacchioni, Phys. Rev. B **70**, 035419 (2004).

[104] H. Tang, F. Levy, H. Berger, and P. E. Schmid, Phys. Rev. B **52**, 7771 (1995).

[105] A. V. Emeline, G. V. Kataeva, V. K. Ryabchuk, and N. Serpone, J. Phys. Chem. B **103**, 9190 (1999).

[106] M. Lazzeri and A. Selloni, Phys. Rev. Lett **87**, 266105 (2001).

[107] F. Yukruk , A. L. Dogan, H. Canpinar, D. Guc and E. U. Akkaya, Org. Lett. **7**, 2885 (2005).

[108] E. Mete, D. Uner, M. Cakmak, O. Gülseren, and Ş. Ellialtıoğlu, J. Phys. Chem. C **111**, 7539 (2007).

[109] X.-Q. Gong and A. Selloni, J. Phys. Chem. B **109**, 19560 (2005); X.-Q. Gong and A. Selloni, J. Phys. Chem. B **110**, 2804 (2006).

[110] K. J. Hameeuw, G. Cantele, D. Ninno, F. Trani, and G. Iadonisi, J. Chem. Phys. **124**, 024707 (2006).

[111] Z. Zhang, S. -P. Jeng, and V. E. Henrich, Phys. Rev. B **43**, 12004 (1991).

[112] P. Le Fèvre, J. Danger, H. Magnan, D. Chandesris, J. Jupille, S. Bourgeois, M.-A. Arrio, R. Gotter, A. Verdini, and A. Morgante, Phys. Rev. B **69**, 155421 (2004).

[113] A. T. Paxton and L. Thiên-Nga, Phys. Rev. B **57**, 1579 (1998).

[114] D. Pillay and G. S. Hwang, Phys. Rev. B **72**, 205422 (2005).

[115] C. Di Valentin, G. Pacchioni, and A. Selloni, Phys. Rev. Lett. **97**, 166803 (2006).

[116] P. Kruger *et al.*, Phys. Rev. Lett. **100**, 055501 (2008).

[117] O. Ozcan *et al.*, Appl. Catal. B: Environ. **71**, 291297 (2007).

[118] Y. Han, C. J. Liu, Q. F. Ge, J. Phys. Chem. B **110**, 7463 (2006).

[119] A. Vittadini and A. Selloni, J. Chem. Phys. **117**, 353 (2002).

[120] A. Vijay, G. Mills, H. Metiu, J. Chem. Phys. **118**, 6536 (2003).

[121] S. Chrétiena and H. Metiub, J. Chem. Phys. **127**, 244708 (2007).

[122] H. Iddir, S. Ögüt, N. D. Browning, and M. M. Disko, Phys. Rev. B **72**, 081407 (2005).

[123] H. Iddir, V. Skavysh, S. Ögüt, N. D. Browning, and M. M. Disko, Phys. Rev. B **73**, 041403 (2006).

[124] X.-Q. Gong, A. Selloni, O. Dulub, P. Jacobson, U. Diebold, J. Am. Chem. Soc. **130**, 370 (2008).

[125] S. J. Tauster, S. C. Fung and R. L. Garten, J. Am. Chem. Soc. **100**, 170 (1978).

[126] A. Sanchez, S. Abbet, U. Heiz, W.-D. Schneider, H. Häkkinen, R. N. Barnett, and U. Landman, J. Phys. Chem. A **103**, 9573 (1999).

[127] H. Häkkinen, S. Abbet, A. Sanchez, U. Heiz, and U. Landman, Angew. Chem., Int. Ed. Engl. **42**, 1297 (2003).

[128] B. Yoon, H. Häkkinen, U. Landman, A. S. Wörz, J.-M. Antonietti, S. Abbet, K. Judai, and U. Heiz, Science **307**, 403 (2005).

[129] G. Henkelman, A. Arnaldsson, and H. Jansson, Comput. Mater. Sci. **36** 254-360 (2006).

[130] E. Sanville, S. D. Kenny, R. Smith, and G. Henkelman, J. Comp. Chem. **28** 899-908 (2007).

[131] J. G. Wang, and B. Hammer, Top. Catal **44**, 49 (2007).

[132] J. B. Park, S. F. Conner, and D. A. Chen, J. Phys. Chem. C **112**, 5490 (2008).

[133] C. Mihut, C. Descorme, D. Duprez and M. D. Amiridis, J. Catal. **212**, 125 (2002).

[134] S. Chilukuri *et al.*, Stud. Surf. Sci. Catal **146**, 573 (2003).

[135] J. Luo *et al.*, Catal. Today **99**, 291 (2005).